# Performance of Metallic Fast Reactor Fuel( Dissertation_全文 )

AUTHOR(S):

Ogata, Takanari

# Performance of Metallic Fast Reactor Fuel

By

Takanari Ogata

March 2000

# Contents

# Chapter 1.

# Introduction

## 1.1. Background

Metallic fuels containing uranium and plutonium are ideal for fast reactors, because they have higher densities of fissile and fertile materials than any other types of fuels, which leads to a higher breeding ratio of the fast reactor core. Therefore, early experimental fast reactors – EBR-I, EBR-II, Enrico-Fermi Reactor, and DFR – utilized uranium alloys as driver fuels [1]. Before the full potential of metallic fuels could be established, worldwide interest turned toward oxide fuels for fast reactors [2]. At Argonne National Laboratory (ANL), continuous effort had been made to increase burnup of the metallic fuel. As a result of irradiation tests for metallic fuels of various specifications, the U-Pu-10wt.%Zr alloy fuel with ~75 % smear density was selected for the Integral Fast Reactor (IFR) program [2,3] initiated at ANL in 1983. In the IFR program, ~8000 pins of the U-10wt.%Zr binary alloy fuels and ~600 pins of the U-Pu-10wt.%Zr ternary fuels were irradiated [4] until the program was forced to terminate by a political issue in 1994. About 1800 pins of these fuels exceeded 10 at.% burnup [4]. The highest burnup achieved was more than 18 at.% for the U-19wt.%Pu-10wt.%Zr fuel pin [5,6], whereby the high-burnup capability of the metallic fuel was demonstrated. The schematic view of the metallic fuel pin is illustrated in Fig. 1-1. Typical specifications of the metallic fuel pins [7,8] tested in the IFR program are presented in Table 1-1. Cast cylindrical fuel alloy is called a "fuel slug." Smear density for the metallic fuel is usually ~75%, which is lower than that for the ceramic fuels, in order to accommodate gas swelling and to moderate FCMI (Fuel-Cladding Mechanical Interaction). Here, "smear density (%)" is defined as a fuel slug cross-sectional area divided by an internal cross section of the cladding. Since sodium does not react with the U-Pu-Zr alloys, the gap between the fuel slug and cladding can be filled with sodium (bond Na) to enhance thermal conduction from the fuel slug to the coolant.

Success in metallic fuel development by ANL will bring about breakthroughs in development of the fast reactor and its fuel cycle technology, as follows [2].

First, the reactor core of the metallic fuel has a high breeding ratio due to higher fuel (fissile and fertile) densities and harder neutron energy spectrum. This reduces core reactivity change due to burnup, then leads to a longer period of reactor operation cycle.

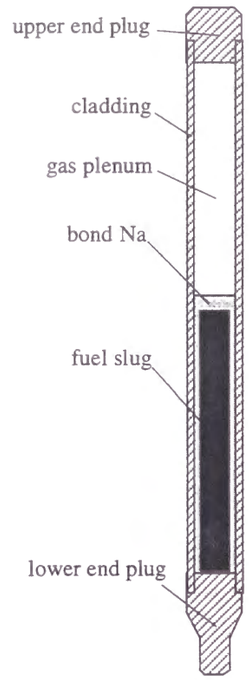


Fig. 1-1 Schematic view of the metallic fuel pin.

Table 1-1 Typical specification of the metallic fuel pins tested in EBR-II and FFTF

| | EBR-II [7] | FFTF [8] |
|---|---|---|
| Fuel slug composition (wt%) | U-19Pu-10Zr | U-19Pu-10Zr |
| Slug length (mm) | 343 | 914 * |
| Slug diameter (mm) | 4.32 | 4.98 |
| Cladding material | HT9 | D9 |
| Cladding diameter (mm) | 5.84 | 6.86 |
| Cladding thickness (mm) | 0.381 | 0.56 |
| Smear denisty (%) | 72 | 75 |
| Plenum/slug volume ratio | 1.01 | 1 |
| Peak linear power rate (W/cm) | ~400 | 492 |
| Peak cladding temperature (°C) | ~590 | 604 |

* U-10wt%Zr blanket slugs of 165 mm length were attached immediately above and below the ternary fuel slug.



Second, higher thermal conductivity of the fuel alloy and use of the bond-Na produce favorable thermal coupling between the slug and coolant. This promotes inherent safety characteristics of the fast reactor core; for example, in the loss-of-flow events, the temperature of the metallic fuel increases along with the coolant temperature rise, and consequently a negative reactivity feedback by the Doppler effect is provided to the reactor core. This inherent safety feature of the metallic fuel core was demonstrated in 1983 in the Experimental Breeder Reactor - II (EBR-II).

Another breakthrough is due to the application of a novel technology, called "pyroprocess," to the recycling of the spent metallic fuel. In the pyroprocess, U and Pu are separated from fission products by electrorefining. The recovered U and Pu are melted and cast into silica tubes (molds) to fabricate new fuel slugs. The pyroprocess is simpler than the recycle system for the oxide fuel – the PUREX process and fuel pellet production –, so the fuel cycle cost for the metallic fuel will be reduced. Although a part of fission products, especially lanthanides, remains in the recycled metallic fuel in the pyroprocess, it does not significantly affect performance of the fast reactor core. Instead, the retained fission products keep the fuel highly radioactive and provide resistance against proliferation of the nuclear materials. Almost all of the minor actinides (MA), such as Np, Am, and Cm, also remain in the recycled metallic fuel, so the radioactive toxicity that lasts for a longer period in the high-level waste will be reduced.

In order to realize this attractive energy production system consisting of the metallic fuel fast reactor and the pyroprocess, the metallic fuel must be shown to be applicable to commercial use. The purpose of this thesis is to show this applicability by evaluating the performance of the metallic fuel from the standpoint of fuel pin design.

In the following sections, after key features of irradiation behavior of the metallic fuel pin are reviewed, methodology for the performance evaluation is presented.

### 1.2. Irradiation behavior of metallic fuel

The first irradiation test for the U-Pu-Zr alloy fuel was conducted in the 1960s using the thermal reactor CP-5 [9]. Then 16 pins of the U-Pu-Zr fuels were irradiated in EBR-II [10], where the maximum burnup was about 4.5 at.%. A new series of irradiation tests for the metallic fuels was started in the IFR program in February of 1985, and the U-Zr binary and U-Pu-Zr ternary fuels were tested until cancellation of the program in September of 1994. Almost all of the above irradiation experiences were obtained in EBR-II, where the fuel slug length was limited to ~34 cm. Several ternary fuel pins were

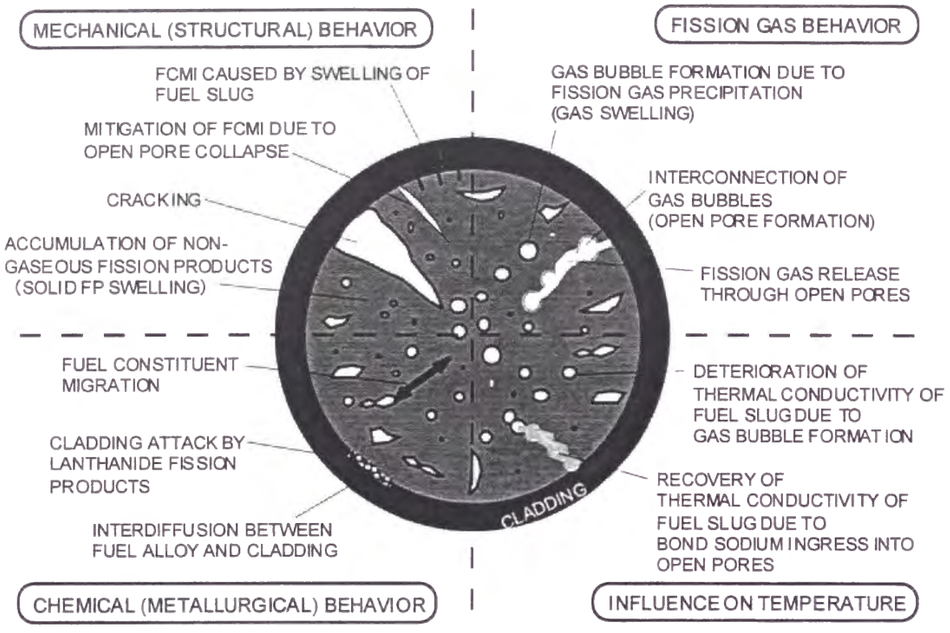


Fig. 1-2 Irradiation behavior of the metallic fuel.

also irradiated in FFTF [8], where about 90 cm of the slug were tested to investigate slug length effects on the irradiation behavior. Furthermore, some transient tests were conducted in the TREAT reactor [11] and the hot cell [12] in order to simulate the transient-over-power and loss-of-flow events, respectively. From those extensive irradiation tests, the characteristic behavior of the metallic fuel pins was clarified as follows. Figure 1-2 illustrates this irradiation behavior schematically.

### 1.2.1. Gas swelling and fission gas release

Fission gas atoms produced during the early stage of irradiation (<~1 at.% burnup) form gas bubbles in the fuel alloy and are not released outside of the fuel slug [2,13]. This leads to a higher rate of fuel gas swelling, ~40 dV/V% per at.%-burnup, at this stage. Further irradiation increases the number density of gas bubbles and causes interconnections among gas bubbles [2,13], provided that the fuel smear density is designed to be sufficiently low, for example, ~75 %. The interconnected bubbles develop to form the open pore which has a connection to the outside of the slug [2,13]. The open pore acts



as a path for fission gas release and decreases further gas swelling. The open pore may collapse when it is compressed. Due to this mechanism, FCMI remains at a low level. In the case of ~75% smear density fuel, fission gas release starts at ~1 at.% burnup, increasing with burnup, and then the ratio of released to generated gas amount (fractional gas release) levels off at a value of ~60 – ~80 % at a higher burnup than ~10 at.% [2,3,5,14]. Released fission gas accumulates inside the fuel pin and increases gas plenum pressure, which is one of the causes of the cladding stress increase [5].

### 1.2.2. Fuel-cladding mechanical interaction (FCMI)

In the case of ~75% smear density fuel, FCMI stress remains at a low level, as stated in the foregoing subsection. At a higher burnup (> ~10 at.%), however, FCMI stress increases and affects cladding diametral strain [7,14]. It is thought that this significant level of FCMI is caused by the accumulation of solid-state fission products.

### 1.2.3. Deformation of the fuel slug

For the ~75% smear density fuel, almost all of the gap between the fuel slug and the cladding closes by approximately 2 at.% burnup due to gas swelling and radial crack formation [13]. Although the radial deformation of the slug reaches ~16 % for the ~75 % smear density fuel at the time of the gap closure, axial deformation of the slug is only 2~8 % [13]. This anisotropic deformation has been explained by radial crack, anisotropic irradiation growth of αU crystals and related cavitational swelling, and the slug radial stress caused by radial distribution of the swelling [13]. After the gap closure, both radial and axial deformation of the slug are restrained by the cladding [13].

### 1.2.4. Fuel-cladding chemical interaction (FCCI)

The rare earth fission products generated in the fuel alloy matrix migrate out to the peripheral region of the slug, agglomerate at the slug-cladding gap, then cause chemical or metallurgical reactions with the cladding [6,7,10]. The reaction layer in the cladding is brittle [14], so that this layer should be treated as a cladding wastage. The maximum reaction layer thickness of ~100 μm has been observed so far [15], which is comparable in level to the FCCI layer thickness for the oxide fast reactor fuel [16]. One of the mechanisms of the rare earth migration is thought to be vapor transport through the open pore [6].

### 1.2.5. Liquefaction of the peripheral region of the fuel slug

In a series of ex-reactor tests where segments of irradiated fuel pins have been heated, liquefaction of the fuel alloy matrix adjacent to the cladding has been observed at ~660 °C [17]. This liquid phase has been formed as a result of the interdiffusion between the U-Pu-Zr fuel alloys and cladding materials [17]. The liquid phase formation promotes cladding wastage [17] and degrades cladding integrity. Therefore, the potential for liquid phase formation in the fuel pin should be excluded during normal reactor operation. The conditions for liquefaction, for example, the cladding temperature and the fuel alloy composition, have not been clarified.

### 1.2.6. Change in thermal conductivity of the fuel slug

Fission gas bubbles reduce the thermal conductivity of the fuel slug [18]. When the open pore is sufficiently developed, however, the bond Na infiltrates the porous slug through a part of the open pore, and thermal conductivity recovers accordingly. While a part of the bond Na in the open pore may be expelled by fission gas, it is known that 25 ~ 40 % of the total pore (= closed gas bubble plus open pore) is infiltrated by bond Na on an average [2,18].

### 1.2.7. Fuel constituent migration

The fuel alloy constituents, especially U and Zr, migrate radially during irradiation [19,20]. Remarkable migration of Pu has not been observed [19]. At the radial cross section where the center-line temperature is expected to exceed ~700 °C, three radial zones have been observed [20]: the central zone where Zr is enriched and U depleted, the outermost zone that retains the as-fabricated composition, and the intermediate zone in between where Zr is depleted and U enriched. In the case of the U-Zr binary fuel, these zones are consistent with the U-Zr phase diagram [20]; the innermost and outermost zones correspond to the BCC solid-solution region and αU-containing phase, respectively. The mechanism of the fuel constituent migration will be thermo-diffusion [20,21,22]. The solidus, liquidus, thermal conductivity, and other physical properties of the fuel alloy are varied with the local fuel composition. The fission rate, i.e., power generation rate, will be also affected by the redistributed constituents. Before the margin to the slug center-line melting is estimated, therefore, the effect of the fuel constituent migration on the slug



temperature should be examined.

## 1.3. Points of performance evaluation of metallic fuel pins

Results of irradiation tests indicate that a normal mode of cladding breach for the metallic fuel pins is creep rupture due to cladding stress increase mainly by fission gas accumulation in the gas plenum, FCMI, and FCCI [14]. Cladding strain should be limited to an appropriate range over the fuel lifetime in order to retain the integrity of coolant flow channel and minimize the bundle-duct interaction, as in the case of the oxide fuel. Therefore, analysis of the cladding stress and strain is required in order to estimate the lifetime of the metallic fuel pin.

Because the center-line melting in the oxide fuel pin causes significant FCMI and leads to cladding breach, the oxide fuel is designed so that the pellet temperature never exceeds its melting temperature. In the case of the metallic fuel, the center-line melting causes axial elongation (extrusion) [11] of the slug and changes reactor core geometry, while it has not been related directly to FCMI increase. The center-line melting should be avoided also in the metallic fuel from the standpoint of stability of the core geometry.

Another design limit for the metallic fuel pin is to avoid liquefaction of the peripheral region of the fuel slug, as mentioned in Subsection 1.2.5. The potential for liquefaction in the fuel pin should be excluded during normal reactor operation.

From the above considerations on the life-controlling factors and the design limits, the author recognizes that performance of the metallic fuel pin can be evaluated primarily from the following points:

(1) cladding stress and strain,

(2) slug center-line melting,

(3) liquefaction of the slug peripheral region.

As reviewed in Section1.2, (1) to (3) above are closely related to the irradiation behavior, fuel pin specifications, and irradiation conditions. The relationship (Fig. 1-3) among them should be appropriately considered, when performance of the metallic fuel pin is evaluated. Therefore, the computer code ALFUS [23,24] has been developed for comprehensive analysis of the metallic fuel irradiation behavior, such as gas swelling, FCMI, and slug temperature change. Cladding strain of the fuel pins tested in EBR-II has been analyzed to validate the ALFUS code. The mechanism of increase in the cladding stress and strain is derived from the analytical results. The development and validation of ALFUS are described in Chapter 2. The ALFUS code is then applied to the analysis of a prototypic

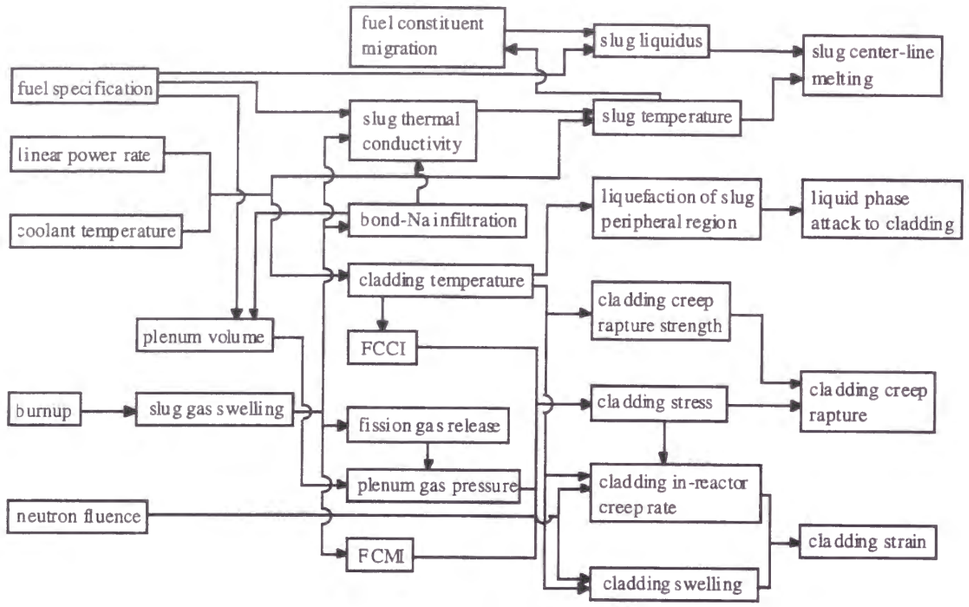


Fig. 1-3 Relationship among the irradiation behavior, fuel pin specification, and irradiation condition.

metallic fuel pin [25]. Chapter 3 presents the results of the analysis, in particular, of (1) cladding stress and strain and (2) slug center-line melting. As for (3) liquefaction of the slug peripheral region, limited experimental data are available. Therefore, the ex-reactor experiment [26] has been conducted using the diffusion couples consisting of U-Pu-Zr alloys and Fe. The first fundamental data on the conditions for liquefaction are obtained from the experiment, as described in Chapter 4. The performance evaluation of the metallic fuel is summarized in Chapter 5.

## References


[1] L.C. Walters, B.R. Seidel and J.H. Kittel, Nucl. Technol. 65 (1984) 179.

[2] G.L. Hofman and L.C. Walters, "Metallic Fast Reactor Fuels" in: B.R.T. Frost, ed., Materials Science and Technology: A Comprehensive Treatment, Part 1, Vol. 10A (VCH, New York, 1994).

[3] R.G. Pahl, D.L. Porter, D.C. Crawford and L.C. Walters, J. Nucl. Meter. 188 (1992) 3.

[4] R.D. Leggett and L.C. Walters, J. Nucl. Mater. 204 (1993) 23.





[5] R.G. Pahl, R.S. Wisner, M.C. Billone and G.L. Hofman, Proc. Int. Fast Reactor Safety Meeting, Snowbird, 1990, vol. IV (American Nuclear Society, 1990).

[6] H. Tsai, A.B. Cohen, M.C. Billone and L.A. Neimark, Proc. The 3rd JSME/ASME Joint Int. Conf. on Nucl. Eng., Kyoto, vol. 2 (1995) 849.

[7] R.G. Pahl, C.E. Lahm, H. Tsai, and M C. Billone, Proc. Int. Conf. Fast Reactor and Related Fuel Cycles, Kyoto, Japan, P1.19, Atomic Energy Society of Japan (1991).

[8] H. Tsai and L.A. Neimark, Proc. Int. Conf. on Design and Safety of Advanced Nuclear Power Plants, Kyoto, (Atomic Energy Society of Japan 1992) 28.2-1

[9] W.N. Beck, R.J. Fousek and J.H. Kittel, Argonne National Laboratory Report ANL-7388 (1968).

[10] W.F. Murphy, W.N. Beck, F.L. Brown, B.J. Koprowski and L.A. Neimark, Argonne National Laboratory Report ANL-7602 (1969).

[11] T.H. Bauer, A.E. Wright, W.R. Robinson, J.W. Holland and E.A. Rhodes, Nucl. Technol. 92 (1990) 325.

[12] Y.Y. Liu, H. Tsai, M.C. Billone, J.W. Holland and J.M. Kramer, J. Nucl. Mater. 204 (1993) 194.

[13] G.L. Hofman, R.G. Pahl, C.E. Lahm, and D.L. Porter, Metallurgical Trans. 21A (1990) 517.

[14] R.G. Pahl, D.L. Porter, C.E. Lahm, and G.L. Hofman, Metallurgical Trans. 21A (1990) 1863.

[15] R.G. Pahl, C.E. Lahm and S.L. Hayes, J. Nucl. Mater. 204 (1993) 141.

[16] S. Nakayama, et al., Proc. AESJ Annual Meeting, L4, Kyoto, Japan, March 1993.

[17] A.B. Cohen, H. Tsai and L.A. Neimark, J. Nucl. Mater. 204 (1993) 244.

[18] T.H. Bauer and J.W. Holland, Nucl. Technol. 110 (1995) 407.

[19] D.L. Porter, C.E. Lahm and R.G. Pahl, Metallurgical Trans. 21A (1990) 1871.

[20] G.L. Hofman, S.L. Hays and M.C. Petri, J. Nucl. Mater. 227 (1996) 277.

[21] T. Ogawa, T. Iwai and M. Kurata, J. the Less-Common Metals 175 (1991) 59.

[22] M. Ishida, T. Ogata and M. Kinoshita, Nucl. Technol. 104 (1993) 37.

[23] T. Ogata, M. Kinoshita, H. Saito and T. Yokoo, J. Nucl. Meter. 230 (1996) 129.

[24] T. Ogata and T. Yokoo, Nucl. Technol. 128 (1999) 113.

[25] T. Ogata and T. Yokoo, submitted for publication in Proc. 8th Int. Conf. Nucl. Eng. (ICONE-8).

[26] T. Ogata, K. Nakamura, M. Kurata and M.A. Mignanelli, submitted for publication in J. Nucl. Sci. Technol. (in press).

# Chapter 2.

# Development and validation of an irradiation behavior analysis code

## 2.1. Background and outline of the ALFUS code

As stated in Chapter 1, cladding stress and strain are key points to evaluate the performance of the metallic fuel pins. The stress and strain are influenced by the various in-reactor phenomena such as fuel slug swelling, FCMI (Fuel-Cladding Mechanical Interaction), and fission gas release from the slug. These phenomena are also linked closely with each other. For example, FCMI, one of the sources of cladding stress, occurs when the slug swelling rate exceeds the cladding deformation rate after the swollen slug comes in contact with the cladding. One of the slug swelling components is volume of the bubbles produced by the precipitation of gaseous fission products (FP gas) retained in the slug. The FP gas retention is dependent on the amount of the open pores, because the open pore acts as a path for the FP gas release. The FCMI force is dependent on the fuel slug stiffness, which consists of the elasticity and viscosity (creep) of the fuel alloy matrix, and also of the compressibility of the fission gas bubbles, and volume decrease of the open pores. When the mechanical behavior of the metallic fuel is analyzed, therefore, it is necessary to consider the linkage among the in-reactor phenomena.

A computer code is only a possible tool to analyze the cladding stress and strain with consideration of the complicated relations among these phenomena. For analysis of the steady-state irradiation behavior of the metallic fuel pins, the pioneer code, LIFE-METAL [1], has been developed by ANL. The FP gas swelling and release models in LIFE-METAL are, however, based on the empirical correlations, which cannot simulate some of the phenomena important to the metallic fuel such as the interconnection of the closed bubbles, the open pore formation, and gas release through the open pores. Although LIFE-METAL seems to have the "hot-press" model to calculate volume decrease of the porous fuel slug, this code will not estimate FCMI properly because it does not include the concept of the open pore formation and the large radial crack. In Ref.[2], where the high smear density (85%) fuel pin was analyzed, the LIFE-METAL calculation over-estimated the experimental data for the cladding diametral strain. This is probably due to an inappropriate estimate of the



stiffness of the porous slug to reproduce FCMI and slug axial elongation simultaneously, as suggested in Ref.[2]. The SESAME code [3] developed in Japan is based on the empirical models of LIFE-METAL. The capability of SESAME, therefore, is limited for the same reason as stated above.

In order to comprehensively understand the irradiation behavior, analyze cladding stress and strain properly, and establish the design procedure of the metallic fuel pin, ALFUS (ALloyed Fuel Unified Simulator) [4,5] has been newly developed. The ALFUS code includes the following analytical models:

(1) a stress-strain analysis model, including gas bubble compressibility and open pore volume decrease,
(2) a mechanistic model to describe coalescence and growth of the gas bubbles, formation of the open pores and FP gas release,
(3) an empirical model to incorporate the effect of large radial crack formed in the U-Pu-Zr ternary fuel slug,
(4) a model to calculate the volume increase of the fuel alloy matrix due to accumulation of non-gaseous fission products (solid FP swelling),
(5) an empirical correlation to estimate the cladding wastage by rare-earth fission products,
(6) a temperature analysis model with effective thermal conductivity of the porous slug infiltrated by the bond sodium.

These models are linked in ALFUS so that the relations among in-reactor phenomena in the metallic fuel pin can be simulated properly. Input data for ALFUS are fuel pin specification and irradiation condition, such as linear power rate and its axial distribution, coolant flow rate per pin, and coolant inlet temperature. A set of model parameters, the physical and mechanical properties of the fuel alloy and cladding is also required. The ALFUS code outputs temperature distribution and stress-strain state in the slug and cladding, FP gas release, margin to cladding creep rapture (cumulative damage function: CDF), etc.

Change in the melting temperature (solidus and liquidus) of the fuel slug due to the fuel constituent migration is important when the design limit of the fuel pin is evaluated, so ALFUS includes the thermo-diffusion model [6] to simulate the fuel constituent migration. In the present study, this model is not used since the stress-strain calculation in the current version of ALFUS is relatively insensitive to change in the local compositions of the fuel slug. In Chapter 3, hypothetical distributions of the fuel alloy compositions are used to examine the effect of the fuel constituent migration on slug temperature.

The following sections describe the analytical models in some detail, including the model parameters and the fuel alloy properties, then present the results of ALFUS validation. Finally, the stress-strain behavior of the metallic fuel pin is summarized.

## 2.2. Models in the ALFUS code

### 2.2.1. Calculation flow in ALFUS

Calculation flow in ALFUS is schematically shown in Fig. 2.2.-1. First, temperature distribution in the fuel pin at time step $t = t_{n+1}$ is calculated from a linear power rate and a coolant flow rate at the present $t = t_{n+1}$, and from the slug-cladding gap and porosity in the slug at the previous time step $t = t_n$. Second, gas swelling and

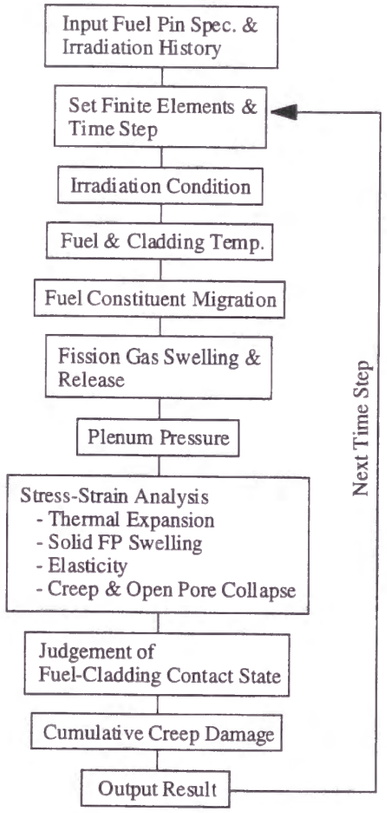


Fig. 2.2.-1 Calculation flow in ALFUS.



gas release are calculated based on the local temperature at $t = t_{n+1}$ and the stress state at $t = t_n$. After strain increments due to gas swelling, solid FP swelling, and thermal expansion during the time step interval $\Delta t = t_{n+1} - t_n$ are obtained, a new stress-strain state of the slug and the cladding are calculated by the Newton-Raphson scheme. Volume changes of the gas bubble and the open pore due to the stress state change are taken into account in the iterative calculation. The contact condition between the fuel slug and cladding is determined from the displacements of the slug outer surface and the cladding inner surface with consideration of the radial crack strain. The usual time step interval $\Delta t = 20$ (hr) is thought to be sufficiently small compared with the time-scale of the in-reactor phenomena during steady-state irradiation. This preset time interval is divided into smaller intervals automatically in accordance with the rate of the slug-cladding gap closure and the creep rate of the hottest part of the slug. Such a time step control is essential when the stress-strain analysis is conducted for a high creep rate material like the U-Pu-Zr alloy.

### 2.2.2. Stress-strain analysis model

#### *2.2.2.1. Basic equations*

Axial symmetric, r-z 2-dimensional finite element method is applied, which is successfully used in the LWR fuel performance code FEMAXI-III [7]. The virtual work principle with respect to a finite element (see Fig. 2.2.-2) yields

$$\int [B_n]^T \{\sigma^i_{n+1}\} dV + \int [B_n]^T \{d\sigma^{i+1}_{n+1}\} dV = \{F_{n+1}\} \quad , \tag{1}$$

where $\{F\}$ is the external force vector, $[B]$ is the node displacement-strain matrix, $\{\sigma\} = \{\sigma_r, \sigma_\theta, \sigma_z, \tau_{rz}\}^T$ is the stress vector. Superscript and subscript in Eq. (1) represent the iteration counter in the Newton-Raphson iterative calculation and the time step, respectively, and "$d$" denotes the corrective increment at *i+1 -th* iteration at the present time $t_{n+1}$. In the parabolic isoparametric element used in this model (see Fig. 2.2.-2), the node displacement $\{u'\} = \{u'_r, u'_z\}^T$ within the element is interpolated as

$$\begin{aligned} u'_r &= N_1 u_{1r} + N_2 u_{2r} + N_3 u_{3r} + N_4 u_{4r} \ , \quad \text{and} \\ u'_z &= N_1 u_{1z} + N_2 u_{2z} + N_3 u_{3z} + N_4 u_{4z} \ , \end{aligned} \tag{2}$$

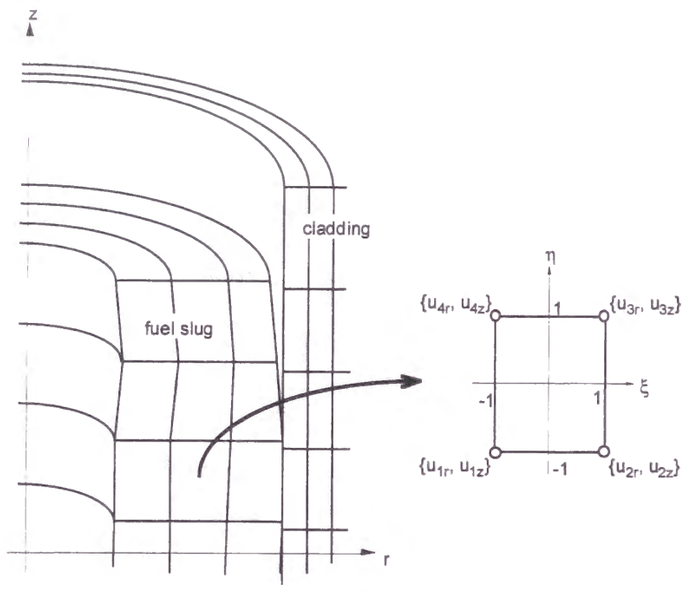


Fig. 2.2.-2 Finite element in the stress-strain analysis model.

where the element nodal displacement: $\{u\}=\{u_{1r},u_{1z},u_{2r},u_{2z},u_{3r},u_{3z},u_{4r},u_{4z}\}^T$. The shape function $N_i$ ($i$=1 to 4) in Eq. (2) is given by

$$N_1=\frac{1}{4}(1-\xi)(1-\eta)\,,\qquad N_2=\frac{1}{4}(1+\xi)(1-\eta)\,,$$
$$N_3=\frac{1}{4}(1+\xi)(1+\eta)\,,\quad\text{and}\quad N_4=\frac{1}{4}(1-\xi)(1+\eta)\,, \tag{3}$$

where $-1\le\xi\le1$, $-1\le\eta\le1$. With the above shape function $N_i$, the node displacement-strain matrix $[B]$ can be expressed in accordance with Ref. [7] as

$$[B]=\begin{bmatrix} \frac{\partial N_1}{\partial r} & 0 & \frac{\partial N_2}{\partial r} & 0 & \frac{\partial N_3}{\partial r} & 0 & \frac{\partial N_4}{\partial r} & 0 \\ 0 & \frac{\partial N_1}{\partial z} & 0 & \frac{\partial N_2}{\partial z} & 0 & \frac{\partial N_3}{\partial z} & 0 & \frac{\partial N_4}{\partial z} \\ \frac{N_1}{r} & 0 & \frac{N_2}{r} & 0 & \frac{N_3}{r} & 0 & \frac{N_4}{r} & 0 \\ \frac{\partial N_1}{\partial z} & \frac{\partial N_1}{\partial r} & \frac{\partial N_2}{\partial z} & \frac{\partial N_2}{\partial r} & \frac{\partial N_3}{\partial z} & \frac{\partial N_3}{\partial r} & \frac{\partial N_4}{\partial z} & \frac{\partial N_4}{\partial r} \end{bmatrix}. \tag{4}$$



The derivatives $\partial N_i/\partial r$ and $\partial N_i/\partial z$ is given by

$$\begin{Bmatrix} \frac{\partial N_i}{\partial r} \\ \frac{\partial N_i}{\partial z} \end{Bmatrix}=[J]^{-1}\begin{Bmatrix} \frac{\partial N_i}{\partial \xi} \\ \frac{\partial N_i}{\partial \eta} \end{Bmatrix}, \tag{5}$$

where the Jacobian matrix $[J]$ is given by

$$[J]=\begin{bmatrix} \sum_{i=1}^{4}\frac{\partial N_i}{\partial \xi}r_i & \sum_{i=1}^{4}\frac{\partial N_i}{\partial \xi}z_i \\ \sum_{i=1}^{4}\frac{\partial N_i}{\partial \eta}r_i & \sum_{i=1}^{4}\frac{\partial N_i}{\partial \eta}z_i \end{bmatrix}. \tag{6}$$

Considering the strain increments at $i+1$ *-th* iteration at the present time $t_{n+1}$, we can express the unknown variable $\{d\sigma_{n+1}^{i+1}\}$ in Eq. (1) as

$$\big([Ce]+[Cs]+[Cc]\big)\{d\sigma_{n+1}^{i+1}\}$$
$$=[B_n]\{\Delta u_{n+1}^{i+1}\}-[Ce]\Big(\{\sigma_{n+1}^{i}\}-\{\sigma_n\}\Big)$$
$$-\Big(\{\Delta\varepsilon_{n+1}^{th,i+1}\}+\{\Delta\varepsilon_{n+1}^{ss,i+1}\}+\{\Delta\varepsilon_{n+1}^{sw,i}\}+\{\Delta\varepsilon_{n+1}^{cr,i}\}\Big)\,, \tag{7}$$

where $\{u\}$ is the element nodal displacement and $\Delta$ means increment from the previous time $t_n$ to the present $t_{n+1}$. Volumetric strain is represented by ε without { } in the following text. Thermal expansion strain $\{\Delta\varepsilon_{n+1}^{th,i+1}\}$ is given as a function of temperature. Components of strain vector $\{\varepsilon\}$ are summarized in Table 2.2.-1. Substituting Eq. (7) into Eq. (1) to eliminate $\{d\sigma_{n+1}^{i+1}\}$, we can obtain the solution $\{\Delta u_{n+1}^{i+1}\}$. Then, the stress vector and each component of the strain at the time step $t=t_{n+1}$ is calculated after $i+1$ iteration. The stress-strain matrices $[Ce]$ and $[Cs]$ correspond to elasticity of the fuel alloy and volumetric change of closed gas bubbles, respectively. The other stress-strain matrix $[Cc]$ represents the response by creep of the fuel alloy and volume decrease of the open pores. Each stress-strain matrix is given as follows.

For the elastic strain-stress matrix $[Ce]$,

Table 2.2.-1 Strain components considered in ALFUS

| Symbol | Strain component | Description |
|---|---|---|
| $\varepsilon^{el}$ | elastic | Subsec. 2.2.2.1. |
| $\varepsilon^{th}$ | thermal expansion | Subsec. 2.2.2.1. |
| $\varepsilon^{sw}$ | gas swelling | Subsec. 2.2.2.2. |
| | $=\varepsilon^{cls}+\varepsilon^{opn}$ | |
| $\varepsilon^{cls}$ | swelling due to closed bubbles | Subsec. 2.2.2.2., 2.2.3.2. |
| $\varepsilon^{opn}$ | swelling due to open pores | Subsec. 2.2.2.2. |
| | $=\varepsilon^{opn+}+\varepsilon^{opn-}$ | |
| $\varepsilon^{opn+}$ | open pore formation | Subsec. 2.2.2.2., 2.2.3.2. |
| $\varepsilon^{opn-}$ | open pore collapse | Subsec. 2.2.2.2. |
| $\varepsilon^{cr}$ | creep + open pore collapse | Subsec. 2.2.2.2. |
| | $=\varepsilon^{creep}+\varepsilon^{opn-}$ | |
| $\varepsilon^{creep}$ | creep | Subsec. 2.2.2.2. |
| $\varepsilon^{ss}$ | solid FP swelling | Subsec. 2.2.5. |

$$\left\{\Delta\varepsilon_{n+1}^{el,i+1}\right\}\equiv\left\{\Delta\varepsilon_{n+1}^{el,i}\right\}+[Ce]\left\{d\sigma_{n+1}^{i+1}\right\}\ ,$$

$$[Ce]=\begin{bmatrix}\frac{1}{E} & -\frac{\nu}{E} & -\frac{\nu}{E} & 0\\ -\frac{\nu}{E} & \frac{1}{E} & -\frac{\nu}{E} & 0\\ -\frac{\nu}{E} & -\frac{\nu}{E} & \frac{1}{E} & 0\\ 0 & 0 & 0 & \frac{2(1+\nu)}{E}\end{bmatrix}, \tag{8}$$

where $E$ is the elastic modulus and $\nu$ is the Poisson's ratio. The stress-strain matrix $[Cs]$ in Eq. (7) for the volume change of closed gas bubbles is defined as

$$\left\{d\varepsilon_{n+1}^{sw,i+1}\right\}\equiv[Cs]\left\{d\sigma_{n+1}^{i+1}\right\}\quad\left(\equiv\left\{\Delta\varepsilon_{n+1}^{sw,i+1}\right\}-\left\{\Delta\varepsilon_{n+1}^{sw,i}\right\}\right). \tag{9}$$

As described in Section 2.2.3., the volume of a closed gas bubble (class $i$) is calculated by the Van der Waals equation:

$$\left(\sigma_m+\frac{2\gamma}{r_i}\right)\left(\frac{4}{3}\pi r_i^{\,3}-m_iA_v\beta\right)=m_iRT\quad . \tag{10}$$



Here, $\gamma$ is the surface tension (N/m), $r_i$ the radius of a class $i$ bubble (m), $m_i$ the gas amount in a class $i$ bubble (mol), $A_v$ the Avogadro number (atoms/mol), $R$ gas constant (J/K/mol), $T$ the temperature (K), $\beta=85\times10^{-30}$ (m$^3$), and $\sigma_m$ the average stress:

$$\sigma_m=\frac{\sigma_r+\sigma_\theta+\sigma_z}{3}\quad . \tag{11}$$

Differentiating Eq. (10) yields

$$-\frac{dr_i}{d\sigma_m}=\frac{r_i^{\,3}-\frac{3}{4\pi}m_iA_v\beta}{3r_i^{\,2}\sigma_m+4\gamma r_i+2\gamma\frac{3}{4\pi}m_iA_v\beta/r_i^{\,2}}\quad . \tag{12}$$

When we consider the volume change of one gas bubble,

$$\frac{d\varepsilon_i^{sw}}{d\sigma_m}=\frac{d\varepsilon_i^{sw}}{dr_i}\frac{dr_i}{d\sigma_m}\quad\text{and}\quad\frac{d\varepsilon_i^{sw}}{dr_i}=4\pi r_i^{\,2}C_i\quad , \tag{13}$$

where $C_i$ is the number density (n/m$^3$) of the class $i$ bubble. From Eqs. (9), (12) and (13),

$$[Cs]=\sum_i\frac{1}{3}\frac{d\varepsilon_i^{sw}}{d\sigma_m}\begin{bmatrix}\frac{1}{3} & \frac{1}{3} & \frac{1}{3} & 0\\ \frac{1}{3} & \frac{1}{3} & \frac{1}{3} & 0\\ \frac{1}{3} & \frac{1}{3} & \frac{1}{3} & 0\\ 0 & 0 & 0 & 0\end{bmatrix}$$

$$=\frac{4\pi r_i^{\,2}\left(r_i^{\,3}-\frac{3}{4\pi}m_iA_v\beta\right)C_i}{27r_i^{\,2}\sigma_m+36\gamma r_i+18\gamma\frac{3}{4\pi}m_iA_v\beta/r_i^{\,2}}\begin{bmatrix}1 & 1 & 1 & 0\\ 1 & 1 & 1 & 0\\ 1 & 1 & 1 & 0\\ 0 & 0 & 0 & 0\end{bmatrix}\quad . \tag{14}$$

The stress-strain matrix $[Cc]$ in Eq. (7) for the creep deformation is defined as

$$\left\{\Delta\varepsilon_{n+1}^{cr,i+1}\right\}\equiv\left\{\Delta\varepsilon_{n+1}^{cr,i}\right\}+[Cc]\left\{d\sigma_{n+1}^{i+1}\right\}=\Delta t_{n+1}\left\{\dot{\bar{\varepsilon}}_{n+\theta}^{c,i+1}\right\}\quad , \tag{15}$$

where the time increment $\Delta t_{n+1}=t_{n+1}-t_n$, and $\left\{\dot{\bar{\varepsilon}}_{n+\theta}^{c,i+1}\right\}$ is the creep strain rate vector

at a stress $\{\sigma_{n+\theta}\}$ estimated at a time $t_{n+\theta} = t_n + \theta(t_{n+1} - t_n)$, $(0 \le \theta \le 1)$. According to Ref. [7], the matrix $[Cc]$ is given by

$$[Cc] = \theta \Delta t_{n+1} \left( F_1 \left[ \sigma'_j \sigma'_k \right]^i_{n+\theta} + F_2 \left[ \frac{\partial \sigma'_j}{\partial \sigma_k} \right]^i_{n+\theta} \right), \tag{16}$$

$$F_1 = \frac{9}{4\left(\bar{\sigma}^i_{n+\theta}\right)^2} \left( \left( \frac{\partial f}{\partial \bar{\sigma}} \right)^i_{n+\theta} - \frac{f^i_{n+\theta}}{\bar{\sigma}^i_{n+\theta}} \right),$$

$$F_2 = \frac{3 f^i_{n+\theta}}{2 \bar{\sigma}^i_{n+\theta}} .$$

Here, the function $f$ is the uniaxial creep strain rate of the fuel alloy given by Eq. (20); $f = \dot{\bar{\varepsilon}}^c(\bar{\sigma})$. The equivalent stress $\bar{\sigma}$ is given by Eq. (21), and the deviatoric stress $\{\sigma'\}$ is defined as

$$\{\sigma'\} = \frac{2\bar{\sigma}}{3} \left\{ \frac{\partial \bar{\sigma}}{\partial \sigma} \right\} . \tag{17}$$

Note that $\left\{\Delta\varepsilon^{cr,i+1}_{n+1}\right\}$ in Eq. (15) includes the strain increment for volume decrease of the open pores, as follows.

### *2.2.2.2. Volume decrease of the open pores*

Total swelling increment $\{\Delta\varepsilon^{sw}\}$ (hereinafter, iteration and time step counters are dropped) in Eq. (7) is defined as

$$\{\Delta\varepsilon^{sw}\} = \{\Delta\varepsilon^{cls}\} + \{\Delta\varepsilon^{opn}\} , \qquad \{\Delta\varepsilon^{opn}\} = \{\Delta\varepsilon^{opn+}\} + \{\Delta\varepsilon^{opn-}\} \tag{18}$$

The vector $\{\Delta\varepsilon^{cls}\}$ is isotropic strain increment due to the closed bubble development, and $\{\Delta\varepsilon^{opn}\}$ is "net" isotropic strain increment due to open pore volume change, which consists of two components: $\{\Delta\varepsilon^{opn+}\}$ and $\{\Delta\varepsilon^{opn-}\}$. The increment $\{\Delta\varepsilon^{opn+}\}$ corresponds to open pore increase by interconnection of the closed bubbles. The gas swelling model explained later gives $\{\Delta\varepsilon^{cls}\}$ and $\{\Delta\varepsilon^{opn+}\}$. The increment $\{\Delta\varepsilon^{opn-}\}$



means the open pore collapse, which is calculated with creep strain increment $\{\Delta\varepsilon^{cr}\}$ as follows. Since the open pore has connection with the external of the slug and does not include high pressure FP gas unlike the closed bubble, it may collapse when compressive stress is applied. Here, volume decrease due to the open pore collapse is assumed to be controlled by creep mechanism and calculated in a manner similar to the hot press model proposed by Rashid et al [8]. When the creep strain component without volume change is denoted by $\{\Delta\varepsilon^{creep}\}$, the sum of $\{\Delta\varepsilon^{opn-}\}$ and $\{\Delta\varepsilon^{creep}\}$ is expressed by the following flow rule:

$$\left\{\Delta\varepsilon^{cr}\right\} \equiv \left\{\Delta\varepsilon^{creep}\right\} + \left\{\Delta\varepsilon^{opn-}\right\} = \dot{\bar{\varepsilon}}^c(\bar{\sigma}) \left\{ \frac{\partial \bar{\sigma}}{\partial \sigma_i} \right\} \Delta t , \tag{19}$$

where $\dot{\bar{\varepsilon}}^c(\bar{\sigma})$ is the equivalent creep strain rate, and $\sigma_i$ $(i = r, \theta, z)$ is the stress in the slug. The stress $\sigma_i$ takes a negative value when it is compressive. The equivalent creep strain rate for the U-Pu-Zr ternary alloy is given by

$$\dot{\bar{\varepsilon}}^c(\bar{\sigma}) = \begin{cases} (5000\bar{\sigma} + 6.0\bar{\sigma}^{4.5}) e^{-52000/RT} & \le 923K \\ 0.08\bar{\sigma}^3 e^{-28500/RT} & > 923K \end{cases} , \tag{20}$$

according to Ref. [9]. The equivalent stress $\bar{\sigma}$ in Eq. (19) is given by

$$\bar{\sigma} = \left[ \frac{1}{2} \left( (\sigma_r - \sigma_\theta)^2 + (\sigma_\theta - \sigma_z)^2 + (\sigma_z - \sigma_r)^2 + 6\tau_{rz} \right) + 3\alpha(\sigma_r + \sigma_\theta + \sigma_z + 3P_{pl})^2 \right]^{1/2}, \tag{21}$$

where the shear stress $\tau_{rz}$ is usually negligible. The term $(\sigma_r + \sigma_\theta + \sigma_z + 3P_{pl})$ represents the net effective hydrostatic stress applied to the open pores because the gas plenum pressure $P_{pl}$ in Eq. (21) is equal to the "internal" pressure of the open pores. The hot press parameter $\alpha$ means the compressibility of the open pores. Substituting Eq. (21) into Eq. (19) yields

$$\left\{\Delta\varepsilon^{cr}\right\} = \frac{\dot{\bar{\varepsilon}}^c(\bar{\sigma})}{2\bar{\sigma}} \Delta t \begin{bmatrix} 2+6\alpha & -1+6\alpha & -1+6\alpha & 18\alpha \\ -1+6\alpha & 2+6\alpha & -1+6\alpha & 18\alpha \\ -1+6\alpha & -1+6\alpha & 2+6\alpha & 18\alpha \end{bmatrix} \begin{Bmatrix} \sigma_r \\ \sigma_\theta \\ \sigma_z \\ P_{pl} \end{Bmatrix} . \tag{22}$$

In Eq. (22), a value of $-1+6\alpha$ must be negative. (For example, consider the case of $\{\sigma\}^T=\{\sigma_r,0,0,0\}$. The sign of $\Delta\varepsilon_\theta^{cr}$ must be opposite to that of $\sigma_r$. ) Therefore, $\alpha$ should be in the range of $0\le\alpha\le 1/6$. In the present study, it is assumed that $\alpha$ is dependent on the open pore swelling $\varepsilon_{sw}^{opn}$ and takes the maximum value when $\varepsilon_{sw}^{opn}$ is as large as 10%:

$$\alpha=\begin{cases}0.0 & ;\varepsilon_{sw}^{opn}=0\\ \dfrac{1}{6}\cdot\left(\dfrac{\varepsilon_{sw}^{opn}}{0.1}\right)^{1.5} & ;0<\varepsilon_{sw}^{opn}<0.1\\ 1/6 & ;0.1\le\varepsilon_{sw}^{opn}\end{cases} . \tag{23}$$

The dependency of $\alpha$ on $\varepsilon_{sw}^{opn}$ has been determined based on the following consideration of the compressibility of the porous material which consists of the same-sized spherical shells (see Fig. 2.2.-3).

When hydrostatic pressure $P_{ex}$ is applied to the porous material as shown in Fig. 2.2.-3, the equivalent stress $\bar{\sigma}_{pm}$ in this material can be expressed from Eq. (21) as

$$\bar{\sigma}_{pm}=3\sqrt{3\alpha}\cdot\left(P_{ex}-P_{in}\right). \tag{24}$$

Here, $P_{in}$ is internal pressure in the central pore ( $P_{ex}>P_{in}$). Substituting Eq. (21) into Eq. (19) and using Eq. (24) give the following volumetric strain rate $\dot{\varepsilon}_V^c$ :

$$\dot{\varepsilon}_V^c=-3\sqrt{3\alpha}\cdot\dot{\bar{\varepsilon}}^c(\bar{\sigma}_{pm}) . \tag{25}$$

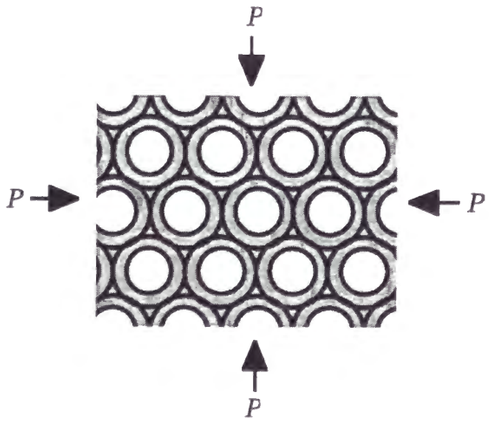


Fig. 2.2.-3 Closely-packed spherical shells, forming porous material.



On the other hand, if each shell itself is made of dense material, the creep deformation rate of the shell under hydrostatic pressure $P_{ex}$ is described by $\alpha=0$ in Eq. (21). The volumetric strain rate of the whole shell including the central pore is expressed as

$$\dot{\varepsilon}_V^c=-3\cdot\dot{\bar{\varepsilon}}^c(\bar{\sigma}_{sh}) . \tag{26}$$

The equivalent stress $\bar{\sigma}_{sh}$ at the outer surface of the shell ( $r=r_2$ ) is given by

$$\bar{\sigma}_{sh}=\frac{3}{2}\varepsilon_{pore}\cdot\left(P_{ex}-P_{in}\right),\qquad \varepsilon_{pore}=\frac{r_1^3}{r_2^3-r_1^3}, \tag{27}$$

where $r_1$ is the central pore radius, and $\varepsilon_{pore}$ means the volume ratio of the central pore to the dense material. When the interstitial media between the shells is assumed to transmit the forces but not to contribute to the volumetric strain of the whole material [8], the volumetric strain rate of Eq. (25) is equal to that of Eq. (26). When a creep rate of the dense material of the shell is assumed to be expressed in the form of

$$\dot{\bar{\varepsilon}}^c=A\sigma^n\ ,\quad (A:\text{constant}) \tag{28}$$

coupling Eq. (25) with Eq. (26) yields

$$\alpha=\frac{1}{3}\left(\frac{\varepsilon_{pore}}{2}\right)^{\frac{2n}{n+1}} . \tag{29}$$

The index $2n/(n+1)$ in Eq. (29) takes a value of approximately 1.5, since the creep rate correlation for U-Pu-Zr alloys used in ALFUS has the stress dependence of $n=3$ for the $\gamma$-solid solutions (higher than 923 K) and $n=3\sim4.5$ for the lower temperature, as expressed in Eq. (20). Equation (23) is obtained by adjusting Eq. (29) so that $\alpha$ takes the value of 1/6 at $\varepsilon_{sw}^{opn}=0.1$. The idealized model described above is thought applicable to the limiting case that the open pores are almost collapsed and "closed", namely $\varepsilon_{sw}^{opn}\to 0$.

Mcdeavitt [10] conducted hot isotropic pressing (HIP) experiments at 973 K for porous U-10 wt.% Zr specimens produced by sintering U and Zr powders. Linear strain rates of the specimens were measured in those experiments. The results for the "metal-derived specimens" [10] are summarized in Table 2.2.-2. The U-Zr specimens

Table 2.2.-2 Result of HIP experiment for sintered U-Zr alloys (Ref. 10)

| Specimen | Driving Force (MPa) | Linear Strain Rate* (/s) | Fractional Closed Pore** (%) | α |
|---|---|---|---|---|
| M9 | 15.5 | 2.50E-06 | 5.3 | 0.0093 |
| M10 | 8.9 | 2.50E-07 | 9.8 | 0.0067 |
| M13 | 20.7 | 7.00E-06 | 3.2 | 0.0101 |
| M15 | 12.4 | 1.20E-06 | 1.5 | 0.0090 |
| M18 | 12.4 | 1.20E-06 | 5.2 | 0.0090 |
| M20 | 19.4 | 7.00E-06 | 6.4 | 0.0111 |
| M22 | 5.7 | 3.00E-08 | 9.8 | 0.0046 |

* Read from plot data in Ref. 10.

** Calculated from data reported in Ref. 10 by (% closed porosity)/(100-(% closed porosity)).

included closed pores in which internal pressure had been equilibrated with the sintering pressure. The HIP stress, which was sufficiently higher than the closed pore pressure, is applied to the specimens with pressurized Ar gas. During the HIP process, volume of the closed pores in the specimens decreased, while volume of the open pores was thought almost constant because the pressurized Ar gas was in the open pore. Therefore, the volume fraction of the closed pores in Table 2.2.-2 corresponds to that of the open pores in the ALFUS model. The range of the fractional closed pore in Table 2.2.-2 can be interpreted to the open pore swelling of $0.015 \le \varepsilon_{sw}^{opn} \le 0.1$. Applying Eqs. (19) and (21) to the porous U-Zr specimens, the measured linear strain rate $-\dot{\varepsilon}_l$ is expressed as

$$-\dot{\varepsilon}_l = \frac{-\dot{\varepsilon}_V^c}{3} = \sqrt{3\alpha} \cdot \dot{\bar{\varepsilon}}^c(\bar{\sigma}_{HIP}). \tag{30}$$

Creep strain rate $\dot{\bar{\varepsilon}}^c$ for U-(Pu-)Zr alloys at 973 K is given in Ref. [10] by

$$\dot{\bar{\varepsilon}}^c = 3.2 \times 10^{-8} \cdot \bar{\sigma}_{HIP}{}^3 , \tag{31}$$

which is essentially identical to Eq. (20). The equivalent stress $\bar{\sigma}_{HIP}$ in Eq. (30) is given in the form similar to Eq. (24) :

$$\bar{\sigma}_{HIP} = 3\sqrt{3\alpha} \cdot P_{eff} , \tag{32}$$



where $P_{eff}$ is the HIP driving force in Table 2.2.-2. Substituting Eqs. (31) and (32) into Eq. (30) gives the hot press parameter:

$$\alpha = \sqrt{\frac{-\dot{\varepsilon}_l}{7.8 \times 10^{-6} \cdot P_{eff}{}^3}} . \tag{33}$$

Values of $\alpha$ calculated from Eq. (33) are also presented in Table 2.2.-2, which indicates that $\alpha$ is in the range from 1/220 to 1/90. Although the function of Eq. (23) gives larger $\alpha$ values than this range, Eq. (23) seems acceptable because the open pore in the irradiated fuel slug is really "open" to the outside of the slug and thought more compressible than the closed pore in the sintered U-Zr specimen.

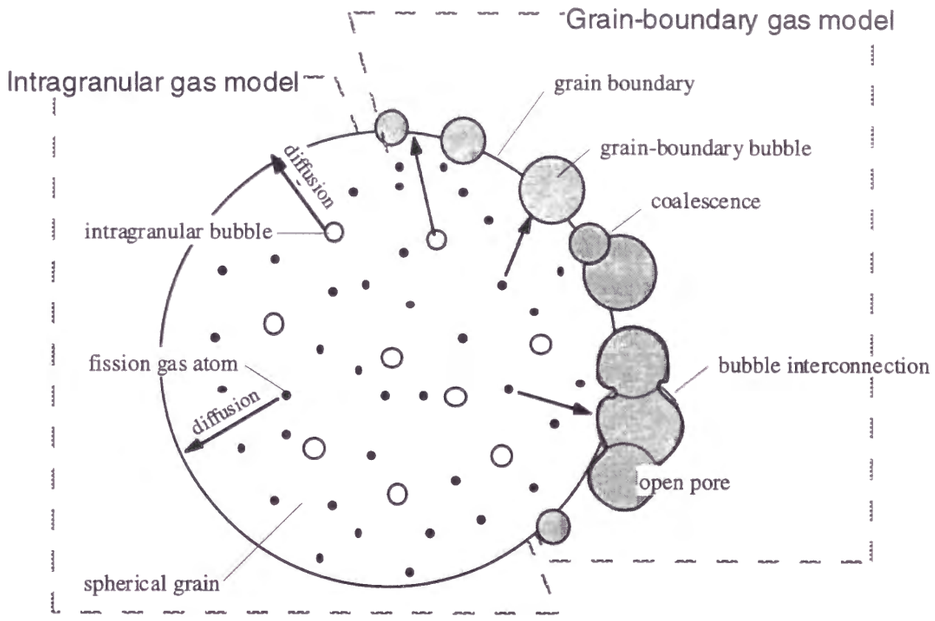


Fig. 2.2.-4 Concept of gas swelling model in ALFUS.

### 2.2.3. Gas swelling model

The gas swelling model gives the strain increments $\{\Delta\varepsilon^{cls}\}$ and $\{\Delta\varepsilon^{opn+}\}$ in Eq. (18) due to the closed bubble and open pore formation, respectively, and also calculates fission gas amount released to the gas plenum. This swelling model, which was applicable to analysis of uranium metal swelling [11], has been modified and incorporated into the ALFUS code [4].

This gas swelling model comprises two parts (see Fig. 2.2.-4); One of the sub-models describes migration of fission gas atoms and intragranular gas bubbles into the grain or phase boundary (intragranular gas model). Another sub-model describes growth of the grain-boundary bubbles due to gas supply from the grain and coalescence with the existing grain-boundary bubbles (grain-boundary gas model). The open pore formation due to interconnection of the grain-boundary (closed) bubbles and fission gas release through the open pore are also treated in this sub-model. Gas swelling volume is calculated as total volume of the closed bubbles and the open pores.

#### *2.2.3.1. Intragranular gas model*

The intragranular gas model for oxide fuel by Wood and Matthews [12] is modified and applied to calculate the concentrations of fission gas atom and gas bubble in the grain. The following assumptions are made in this model;

(a) A part of the gas atoms generated by fission forms gas bubbles in the grain. Some gas atoms may be trapped by the existing gas bubbles. Some of the gas bubbles may be destroyed by a fission fragment and dissolved in the fuel alloy matrix. Fission gas atoms and gas bubbles migrate in the spherical grain by the diffusion mechanism (Fig. 2.2.-4). The number density of the gas bubbles is represented by a single bubble size.

(b) The gas bubble formation (nucleation), gas atom trapping by the gas bubbles, and the re-solution of the gas into the matrix are in an equilibrium state.

(c) The gas atoms and bubbles that arrive at the grain boundary form the grain-boundary bubbles or flow into the existing grain-boundary bubbles, and do not come back to the grain. This means that the concentrations of both gas atom and intragranular bubble are zero at the boundary.

According to Ref.[12], assumption (a) is expressed as



$$\frac{\partial C_g}{\partial t} = \frac{1}{r^2}\frac{\partial}{\partial r}\left( D_g r^2 \frac{\partial C_g}{\partial r} \right) + K_g - D_g k_b^2 C_g - KC_t + bC_{gb} \quad , \tag{34}$$

$$A_v m_0 \frac{\partial C_b}{\partial t} = A_v m_0 \frac{1}{r^2}\frac{\partial}{\partial r}\left( D_{gb} r^2 \frac{\partial C_b}{\partial r} \right) + D_g k_b^2 C_g + KC_t - bC_{gb} \quad , \tag{35}$$

where

$C_g$ : the concentration of fission gas atoms dissolved in the matrix (atoms/m$^3$),

$C_{gb}$ : the concentration of gas included in intragranular bubbles (atoms/m$^3$);

$C_{gb} = A_v m_0 C_b$ ,

$C_b$ : the number density of intragranular bubbles (bubbles/m$^3$),

$C_t = C_g + C_{gb}$ ,

$A_v$ the Avogadro number (atoms/mol),

$m_0$ : the gas amount in one intragranular bubble (mol),

$D_g$ : the diffusion coefficient of the fission gas atom (m$^2$/s),

$D_{gb}$ : the diffusion coefficient of the intragranular bubble (m$^2$/s),

$K_g$ : the generation rate of the fission gas atoms (atoms/m$^3$/s),

$D_g k_b^2 C_g$ : the rate of gas atom trapping by the bubble (atoms/m$^3$/s),

$KC_t$ : the bubble nucleation rate (atoms/m$^3$/s), and

$bC_{gb}$ : the rate of the bubble re-solution by fission fragment (atoms/m$^3$/s).

In Ref.[12] for the oxide fuel, the gas bubbles was assumed to be immobile, so that the first term in the right hand side of Eq. (35) was not included in the equation. In the metallic fuel, however, the diffusion of gas bubbles will not be negligible, because the ratio $T/T_m$ of the fuel temperature $T$ (on average) to the melting temperature $T_m$ for the metallic fuel is higher than that for the oxide fuel.

From assumption (b),

$$D_g k_b^2 C_g + KC_t = bC_{gb} \quad . \tag{36}$$

Values of $K$ and $b$ have been estimated as $K = 4\times10^{-3}$ (/s) and $b = 6\times10^{-2}$ (/s) based on Ref. [12]. The sink strength $k_b^2$ of bubbles for the migrating gas atoms is expressed in Ref. [12] as

$$k_b^2 = 4\pi \cdot r_b \cdot \overline{C}_b \ . \tag{37}$$

Here, $\overline{C}_b$ is estimated from the number density of the bubbles at the previous time step. The radius of the bubble $r_b$ in Eq. (37) is calculated by the Van der Waals equation (see Eq. (10)), assuming an equilibrium state among internal pressure, surface tension and external stress (average stress in the fuel slug) of the bubble. The gas amount $m_0$ in the bubble has been assumed to be $m_0 = 1\times10^{-22}$ so that the bubble radius $r_b$ takes a value of ~1 nm. From Eq. (36),

$$C_g = \frac{b-K}{D_g k_b^2 + b} C_t \ , \quad \text{and} \quad C_{gb} = \frac{D_g k_b^2 + K}{D_g k_b^2 + b} C_t \ . \tag{38}$$

Coupling Eqs. (34), (35) and (38) yields

$$\frac{\partial C_t}{\partial t} = \frac{1}{r^2}\frac{\partial}{\partial r}\left( (D_1 + D_2) r^2 \frac{\partial C_t}{\partial r} \right) + K_g \ , \tag{39}$$

where

$$D_1 = \frac{b-K}{D_g k_b^2 + b} D_g \ , \quad D_2 = \frac{D_g k_b^2 + K}{D_g k_b^2 + b} D_{gb} \ . \tag{40}$$

During normal reactor operation, change in the irradiation conditions, such as fission rate and temperature, is much slower than diffusion of the gas atom and the bubble, so the system can be assumed to be in a steady-state: $\partial C_t / \partial t = 0$. The diffusion equation (39) can be solved under the boundary conditions: $C_t = 0$ at the grain boundary ($r = r_G$, assumed to be 2 μm) from assumption (c), and $\partial C_t / \partial r = 0$ at the center of the spherical grain ($r = 0$). In ALFUS, the approximate numerical solution is used which Matthews and Wood [13] proposed.

The diffusion coefficient $D_g$ of the gas atom in Eqs. (34) and (35) is tentatively assumed to be equal to the self-diffusion coefficient of γ-uranium [14]:

$$D_g = 1.19\times10^{-7} \exp\left( -\frac{26700}{RT} \right) \ , \tag{41}$$

because no data on diffusion of the noble gas atom in metals in available. The diffusion coefficient $D_{gb}$ of the intragranular bubble in Eq. (35) can be related to the



surface diffusion coefficient $D_s$ of the bubble inner surface by considering the jump distance of a bubble due to individual jumps of molecules on its inner surface [15], which yields a form of

$$D_{gb} = C_{adj} \cdot \frac{3}{2\pi}\left( \frac{a_0}{r_b} \right)^4 \cdot D_s \ , \tag{42}$$

where $a_0$ the lattice constant of the fuel alloy ($= 3.0\times10^{-10}$ m). The surface diffusion coefficient $D_s$ of the fuel alloy in Eq. (42) is assumed to be $D_s = 1000 \cdot D_g$, which gives the value close to the correlation evaluated by Gruber and Kramer [16]. The parameter $C_{adj}$ in Eq. (42) has been introduced to account for various factors affecting the gas bubble migration, such as fission fragments, multi-phase structures of the fuel alloy, and an internal gas pressure in the bubble. A value of $C_{adj}$ has been adjusted as described in Subsection 2.2.8.; $C_{adj} = 20$. In this case, $D_{gb} \approx 77 D_g$ for the intragranular bubble.

As far as Eq. (41) is used, $D_g$ takes a value in the range of $\sim10^{-13}$ – $\sim10^{-15}$, and $C_b$ $\sim10^{15}$ – $\sim10^{16}$ in the analyses of EBR-II test fuels and the prototypic fuel. Therefore, a value of $D_g k_b^2$ is the order of $\sim10^{-6}$ ($<< b$), so that the gas concentrations in the form of the gas atoms and bubbles can be estimated from Eq. (38) as

$$C_g \approx \left( 1 - \frac{K}{b} \right) C_t \approx 0.93 C_t \ , \quad \text{and} \quad C_{gb} \approx \frac{K}{b} C_t \approx 0.07 C_t \ . \tag{43}$$

Therefore, the ratio of fission gas transfer by the gas atom diffusion to that by the bubble diffusion can be estimated as

$$\frac{D_g \left( \partial C_g / \partial r \right)_{r=r_G}}{D_{gb} \left( \partial C_{gb} / \partial r \right)_{r=r_G}} \approx \frac{D_g \cdot 0.93 \left( \partial C_t / \partial r \right)_{r=r_G}}{77 D_g \cdot 0.07 \left( \partial C_t / \partial r \right)_{r=r_G}} \approx 0.17. \tag{44}$$

This indicates that ~15 % of total fission gas generated within the grain is transferred by the bubble migration, and this value is relatively independent of the temperature.

#### *2.2.3.2. Grain-boundary gas model*

***Grain-boundary bubble (closed bubble)***

This sub-model describes growth of the grain-boundary bubble, the open pore formation, and fission gas release through the open pore. The following assumptions are made in this grain-boundary bubble model (see Fig. 2.2.-4);

(d) The grain-boundary bubbles coalesce with each other by collision due to their random migration. They also absorb the fission gas atoms diffusing out from the grain. These two processes increase the size of the grain-boundary bubble. The intragranular gas bubbles coming out from the grain form the smallest grain-boundary bubbles.
(e) When the volume fraction of the grain-boundary bubbles increases over a threshold value, they begin interconnecting and form the open pore.
(f) When the bubbles interconnect and form the open pore, the fission gas included in the bubbles is immediately released to the gas plenum. The intragranular and grain-boundary bubbles may collide with the open pore. It leads to gas release and increase in an open pore size. The fission gas atoms may also be released through the open pore.

The grain-boundary (closed) bubbles are classified into *M-1* classes by gas amount $m_i$ (mol) included in each bubble so that growth of the bubbles can be numerically described. Although the characteristics of the open pore will be different from that of the closed bubble, the open pore is categorized into the class *M* "bubble" for the convenience of numerical modeling. The formation of the open pore (bubble interconnection) is, however, treated in a manner different from the growth of the closed bubble, as mentioned later.

The change in the number density of the closed bubble of class *i* can be described by considering fission gas supply from the grain, growth of lower (*i-1*) class bubbles, growth to upper class (*i+1*) bubbles, and collision with upper class bubbles (assumption (d));

$$\frac{dC_1}{dt} = G_1 - R'_{i,j} - \sum_{j=1}^{M} R_{j,1} , \qquad i = 1, \tag{45}$$

$$\frac{dC_i}{dt} = G_i + \sum_{j=1}^{i-1} R'_{i-1,j} - \sum_{j=1}^{i} R'_{i,j} - \sum_{j=i}^{M} R_{j,i} , \qquad i = 2 \text{ to } M-2, \tag{46}$$

where $C_i$ is the number density of class *i* bubble, $G_i$ is the increase rate of the number



density of the class *i* bubble by fission gas transfer from the grain, $R_{i,j}$ is the collision rate of class *i* with class *j* bubble, and $R'_{i,j}$ is the rank-up rate from class *i* to class *i+1* by coalescence with class *j* bubble. The term $G_i$ (*i>1*) in Eqs. (45) and (46) is calculated by distributing the fission gas atom from the grain in proportion to the grain surface area occupied by each class bubble. The term $G_1$ is calculated from gas amount in the intragranular bubbles arriving at the boundary (assumption (d)). According to Ref. [17], $R_{i,j}$ and $R'_{i,j}$ can be expressed as

$$R_{i,j} = 4\pi\delta(D_i + D_j)(r_i + r_j)C_iC_j , \tag{47}$$

$$R'_{i,j} = 4\pi\delta(D_i + D_j)(r_i + r_j)C_iC_jF_{i,j} , \tag{48}$$

$$\delta = \begin{cases} 1/2 & : i = j \\ 1 & : i \neq j \end{cases}$$

where $r_i$ is a radius of class *i* bubble, and $D_i$ is the diffusion coefficient of class *i* bubble. The factor $F_{i,j}$ in Eq. (48) means a fraction of the class *i* bubbles which rank up to the upper class (*i+1*) when one class *i* bubble collides with the lower class (*j*) bubble, and can be given by the conservation of the bubble gas amount:

$$m_i + m_j = (1 - F_{i,j})m_i + F_{i,j}m_{i+1} . \tag{49}$$

The diffusion coefficients $D_i$ in Eqs. (47) and (48) should be determined by considering the characteristics of the grain or phase boundary. However, the bubble mobility on the boundary in the fuel alloy is not known well at this stage. It has been assumed, therefore, that $D_i$ is given by Eq. (42).

***Open pore***

The formulation similar to Eqs. (45) – (49) has been assumed for the open pore formation by interconnection of the gas bubbles. For the class *M-1* bubble (the highest class of the closed bubble) and the class *M* "bubble" (the open pore),

$$\frac{dC_{M-1}}{dt} = G_{M-1} + \sum_{j=1}^{M-2} R'_{M-2,j} - \sum_{j=1}^{M-1} R'_{M-1,j} - \sum_{j=M-1}^{M} R_{j,M-1} \tag{50}$$

$$\frac{dC_M}{dt} = G_M + \sum_{j=1}^{M-1} R''_{M-1,j} + \sum_{j=1}^{M-1} R'_{M,j} , \tag{51}$$

$$R'_{M-1,j} = 4\pi\delta(D_{M-1} + D_j)(r_{M-1} + r_j)C_{M-1}C_j F'_{M-1,j} \quad , \tag{52}$$

$$R''_{M-1,j} = 4\pi\delta(D_{M-1} + D_j)(r_{M-1} + r_j)C_{M-1}C_j F_{M-1,j} f_{M-1,j} , \tag{53}$$

$$R'_{M,j} = 4\pi\delta(D_M + D_j)(r_M + r_j)C_M C_j F_{M,j} . \tag{54}$$

The second term in the right hand side of Eq. (51) represents the open pore formation by interconnection between the grain-boundary bubbles. The first and third terms indicate evolution of the existing open pores by the fission gas supply from the grain and by coalescence with the grain-boundary bubbles, respectively. For the values of $m_i$ assumed in the present study (see Subsection 2.2.8.), $D_M \approx D_{M-1} << D_{M-2}$ and $R'_{M,M-1} << R'_{M,M-2}$, which means that the open pores are treated as immoblile pores.

Based on assumption (e), *F*-factors in Eqs. (52) – (54) are different from that determined by Eq. (49) as follows. Since the open pore is treated as the highest-class (*M*) bubble, the factor $F_{M,j}$ in Eq. (54) is given by the following conservation of gas amount:

$$m_M + m_j = m_M + F_{M,j} m_M , \tag{55}$$

Note that "gas amount" $m_M$ of the open pore is the input parameter which controls the rate of rank-up of the closed bubble to the open pore. A value of $m_M$ has been adjusted so that the fission gas release data can be reproduced, as explained in Subsection 2.2.8. The factor $F'_{M-1,j}$ in Eq. (52) represents the fraction of the bubble interconnection to coalescence of one class *j* bubble with the class *M-1* bubble. When every coalescence of the class *j* bubble with the class *M-1* bubble contributes to the open pore formation (the bubble interconnection, i.e., rank-up to the class *M*), the conservation of gas amount included in the bubbles is expressed as

$$m_{M-1} + m_j = (1 - F_{M-1,j})m_{M-1} + F_{M-1,j} m_M , \tag{56}$$

where $F_{M-1,j}$ is essentially the same as $F_{i,j}$ in Eq. (49). In this case $F'_{M-1,j} = F_{M-1,j}$. On the other hand, when gas swelling is not enough to form the open pore and a part of



the coalescence with the class *M-1* bubble contributes only to increase of the number density of the class *M-1* bubbles, the gas amount conservation is expressed as

$$m_{M-1} + m_j = (1 - F'_{M-1,j})m_{M-1} + F_{M-1,j} f_{M-1,j} m_M \quad . \tag{57}$$

The factor $F'_{M-1,j}$ is calculated by coupling Eq. (56) with Eq. (57). The function $f_{M-1,j}$ can be considered as a probability of open pore formation. It appears reasonable to assume that the probability $f_{M-1,j}$ increases with the gas swelling level. In this study, $f_{M-1,j}$ is given by

$$f_{M-1,j} = \begin{cases} 0.0 & ;\varepsilon^{sw} \le \varepsilon_1^{sw} \\ \dfrac{\varepsilon^{sw} - \varepsilon_1^{sw}}{\varepsilon_2^{sw} - \varepsilon_1^{sw}} & ;\varepsilon_1^{sw} < \varepsilon^{sw} < \varepsilon_2^{sw} \\ 1.0 & ;\varepsilon_2^{sw} \le \varepsilon^{sw} \end{cases} . \tag{58}$$

Here, $\varepsilon^{sw}$ is the calculated gas swelling, and $\varepsilon_1^{sw}$ is the threshold gas swelling for open pore formation. The breakaway swelling level $\varepsilon_2^{sw}$ has been taken as $\varepsilon_2^{sw} = 0.33$ based on Barnes' theoretical consideration [18]. A value of $\varepsilon_1^{sw}$ can be determined either by irradiation experiences or by thermodynamic assessment of open pore morphology, as in the case of $UO_2$ fuel [19]. Tsai et al. [20] reported that fuel pins of 85% smear density, where the fuel slug is allowed to swell only 18 % before the slug-cladding contact, achieved 10 at.% peak burnup without cladding failure and showed fractional fission gas release of approximately 60 %. This suggests that a value of $\varepsilon_1^{sw}$ should be much lower than 0.18 (=18%). Based upon the above irradiation experience, $\varepsilon_1^{sw}$ is set to 0.10.

***Fission gas release***

Fission gas amount retained in a unit volume of the fuel alloy is expressed as

$$M_{retain} = C_g + C_{gb} + \sum_{i=1}^{M-1} m_i \cdot C_i , \tag{59}$$

and fission gas release during a time interval $\Delta t$ is calculated from change in the retained gas amount. Consistently with Eq. (59), fission gas release rate $dM_{release}/dt$ can be also derived from Eq. (51) multiplied by "virtual" gas amount $m_M$ in the open

pore, namely,

$$\frac{dM_{release}}{dt} \equiv m_M \frac{dC_M}{dt} = m_M G_M + m_M \sum_{j=1}^{M-1} R''_{M-1,j} + m_M \sum_{j=1}^{M-1} R'_{M,j} \ . \qquad (60)$$

The first term in Eq. (60) represents release of the fission gas atom from the grain through the existing open pores. The second term means gas release when the grain-boundary (closed) bubbles are interconnected. The third represents release of the gas in the grain-boundary bubbles through the existing open pores.

***Gas swelling***

Volumetric strain increment of the slug due to the closed bubble evolution during a time interval $\Delta t$ is given by

$$\Delta\varepsilon_{n+1}^{cls} = \Delta t \sum_{i=0}^{M-1} v_i \frac{dC_i}{dt} \ , \qquad (61)$$

where i=0 means the intragranular bubble. The volume $v_i$ of one class i bubble is calculated from the gas amount $m_i$ in the bubble based on the van der Waals equation. Volumetric strain increment due to open pore formation is given by

$$\Delta\varepsilon_{n+1}^{opn+} = v_M \frac{dC_M}{dt} \Delta t \quad , \qquad (62)$$

The open pore volume $v_M$ is calculated by the expedient of using the same scheme as the closed bubbles.

### 2.2.4. Effect of radial cracks

After the fuel slug comes into contact with the cladding, further axial growth is restrained. The slug deformation before the slug-cladding contact is anisotropic; The U-Zr binary fuels of about 75 % smear density show axial elongation of 8~10 % of as-fabricated slug length, while radial growth is about 16 % at the slug-cladding contact [21]. This anisotropic deformation can be related to the tearing at the grain or phase boundaries in the peripheral region of the slug due to anisotropic irradiation growth of α-U crystals [21,22]. In the case of the U-Pu-Zr ternary fuel, more pronounced



anisotropy has been observed and suggested to be dependent upon Pu content and radial temperature gradient in the fuel slug [21]. The anisotropy of the ternary fuel slug can be attributed to large radial crack formation due to the brittle nature of the ternary slug [21]. The cracks increase the slug radial strain and promote the anisotropy. In order to incorporate the effect of the cracks on the stress-strain state, the concept of the effective slug radius has been introduced. The effective radius $r^{eff}$ is defined (see Fig. 2.2.-5) as

$$r^{eff} = r_0 + dr^{slug} + dr^{crack} = r^{slug} + dr^{crack}, \qquad (63)$$

where $r_0$ is the as-fabricated slug radius, and $dr^{slug}$ is the radial strain increment due to thermal expansion, elasticity, creep, gas and solid FP swelling. The increment $dr^{crack}$ is due to the cracks and the tearing. After the slug including the tears and cracks comes into contact with the cladding, swelling into the tears and cracks will occur. In fact, extrusion of inner zone fuel into the radial crack was observed [21]. This process

| Stage of the slug-cladding contact: | (I) | (II) | (III) |
|---|---|---|---|
| Actual fuel being irradiated: | 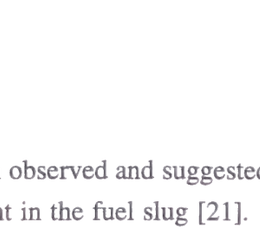  | 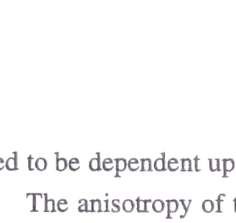  | 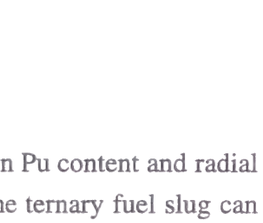  |
| Fuel being calculated by ALFUS: | 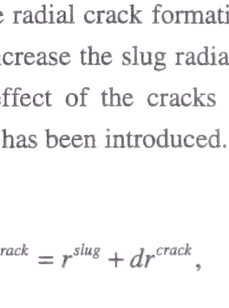  | 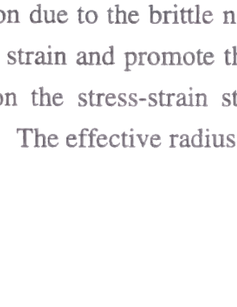  | 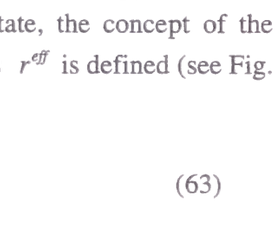 |
| Calculational condition at the outer surface of the slug: | no restraint | axial restraint, but no radial restraint | both axial and radial restraint |

Fig. 2.2.-5 Calculation conditions of the slug-cladding contact-state.

will relax radial FCMI stress. During this stage of the contact (Stage II in Fig. 2.2.-5), the area of the contact interface continues to increase without significant FCMI stress, and then the slug will stick to the cladding. Using $r^{eff}$, the following contact conditions are adopted in the ALFUS calculation (see Fig. 2.2.-5);

(I) $r^{eff} < r_i$ : no restraint by the cladding (no contact),
(II) $r^{slug} < r_i \le r^{eff}$ : axial restraint by the cladding, but no radial restraint,
(III) $r_i \le r^{slug}$ : both axial and radial restraints by the cladding,

where $r_i$ is the inner radius of the cladding. When the above condition is applied to the contact-state judgment, the value of the anisotropic radius increment $dr^{crack}$ at the beginning of Stage II ($r^{eff} = r_i$) must be known, which is estimated as follows.

As shown in the previous study [4], the sum of the strain components except tearing and crack strains is almost isotropic until the slug-cladding contact, so that its strain vector can be expressed as $\{\varepsilon^{iso}, \varepsilon^{iso}, \varepsilon^{iso}\}$. Assuming that the sum of the tearing and crack strains is highly anisotropic and can be expressed as $\{\varepsilon^{crack}, \varepsilon^{crack}, 0\}$ (no axial component), local axial elongation can be expressed as $100 \cdot \varepsilon^{iso}$ (%), and

$$dr^{slug} = \varepsilon^{iso} \cdot r_0^{slug}, \quad dr^{crack} = \varepsilon^{crack} \cdot r_0^{slug} . \tag{64}$$

Here, the anisotropy factor $f^{crack}$ is introduced, which is defined as a ratio of the anisotropic strain to the total strain at the slug-cladding contact ($r^{eff} = r_i$) :

$$f^{crack} \equiv \left( \frac{\varepsilon^{crack}}{\varepsilon^{iso} + \varepsilon^{crack}} \right)_{contact} , \tag{65}$$

where variables in the parentheses $(\ )_{contact}$ take the values at the slug-cladding contact. The anisotropy factor $f^{crack}$ is assumed to be a function of the initial Pu content $C_{Pu}$ and the temperature gradient in the peripheral region of the slug. The temperature gradient can be shown to be proportional to a value of $q/D_0$: the liner power rate divided by the diameter of the slug. Substituting Eqs. (63) and (64) into (65) yields

$$\left(dr^{crack}\right)_{contact} = f^{crack} \cdot r_0^{gap} , \tag{66}$$

where $r_0^{gap}$ $(= r_i - r_0^{slug})$ is the initial gap width between the slug and cladding. The



factor $f^{crack}$ can be estimated as follows; Equation (65) can be transformed to

$$f^{crack} = 1 - \left( \frac{\varepsilon^{iso}}{\varepsilon^{iso} + \varepsilon^{crack}} \right)_{contact}$$

$$= 1 - \frac{\left(\varepsilon^{iso}\right)_{contact}}{\sqrt{\frac{100}{SD} - 1}} , \tag{67}$$

where $SD$ is the initial smear density (%) of the fuel pin;

$$SD = \left( \frac{r_0^{slug}}{r_i} \right)^2 \cdot 100 . \tag{68}$$

Values of $f^{crack}$ for various fuel pins have been calculated by using Eq. (67), and plotted in Fig. 2.2.-6 as a function of $C_{Pu}$ and $q/D_0$. Values of $\left(\varepsilon^{iso}\right)_{contact}$ in Eq. (67) have been estimated from the experimental data [21,23,24] of the axial elongation of the whole slug instead of the local elongation. As can be seen in Fig. 2.2.-4, $f^{crack}$ values

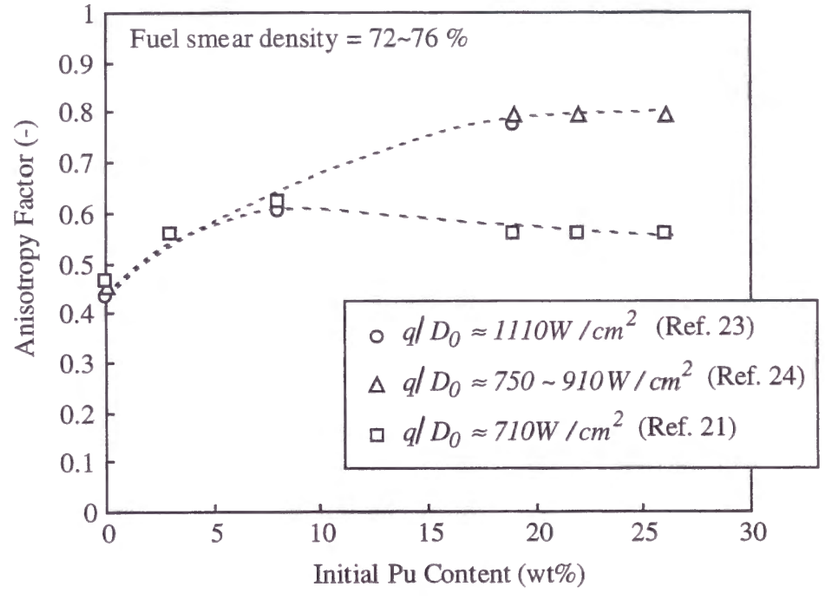


Fig. 2.2.-6 Anisotropy factor $f^{crack}$ as a function of the Pu content $C_{Pu}$ and the temperature gradient ($q/D_0$).

saturate at $f^{crack} \approx 0.8$ when $C_{Pu} \geq 19$ (wt.%) and $q/D_0 \geq 750$ (W/cm$^2$). In the calculations described in the next section, $f^{crack}$ is set to 0.8 because $C_{Pu}$ and $q/D_0$ for the analyzed fuel pins are within the above saturation range. The appropriate value of $\left(dr^{crack}\right)_{contact}$ for each fuel pin is given by Eq. (66).

The tearing model [4] in ALFUS was not used in the present study since the tearing strain is included in the concept of the effective slug radius introduced above.

### 2.2.5. Solid FP swelling model

Non-gaseous fission products cause incompressible volume increase of the fuel slug, which is called "solid FP swelling" hereinafter). The solid FP swelling in the metallic fuel slug can be assumed to be proportional to burnup. Hence, isotropic strain increment $\Delta\varepsilon^{sol}$ due to the solid FP swelling is given in ALFUS by

$$\Delta\varepsilon^{sol} = \dot{\varepsilon}^{sol} \cdot \Delta Bu \ , \tag{69}$$

where $\dot{\varepsilon}^{sol}$ is volumetric strain increment per atomic percent burnup (at.%) due to the solid FP swelling, and $\Delta Bu$ burnup increment. Hofman and Walters [25] have given a value of 1.2 %/at.% to $\dot{\varepsilon}^{sol}$ by considering possible forms of non-gaseous fission products in the irradiated fuel alloy. Pahl et al. [2] have estimated as $\dot{\varepsilon}^{sol} = 1.68\%/at\%$ from the analyses of cladding strain data of irradiated fuel pins. In the present study, a value of solid FP swelling rate $\dot{\varepsilon}^{sol}$ has been revised based on the following theoretical consideration.

Some non-gaseous fission products may form solid solution or intermetallic compounds with the fuel alloy constituents, and others may precipitate. In this study, it is simply assumed that molar volume of each fission product element in the fuel alloy matrix is equal to that of the pure substance. Table 2.2.-3 summarizes the volume occupied by major fission products generated by one mole fissions of the heavy metals (U and Pu). The yield of each nuclide has been calculated using a computer code ORIGEN-2 [26]. The one-group cross sections used in the ORIGEN-2 code have been generated with the neutron spectrum in the reactor core of which fuels are the U-Pu-10wt%Zr ternary alloys. As shown in Table 2.2.-3, one mole fissions of the heavy metals lead to net volume increase of 25.4 cm$^3$. This corresponds to the volumetric strain increment of 1.5 % per one atom percent burnup. Therefore, the solid FP swelling rate of $\dot{\varepsilon}^{sol} = 1.5\%/at\%$ has been used in the present study.



Table 2.2.-3 Amounts and volumes of major fission products generated by 1 mol fissions

| | Elements | Generation (mol) | Molar Volume (cc/mol) | Volume Change (cc) |
|---|---|---|---|---|
| Fuel Constituents | Zr | 0.0000 | 14.01 | 0.00 |
| | U and Pu | -1.0000 | 12.58 | -12.58 |
| Fission Products | (Noble Gas) | (0.2518) | | (-) |
| | Kr | 0.0190 | | - |
| | Xe | 0.2328 | | - |
| | (Alkali Metals) | (0.2051) | | (14.12) |
| | Rb | 0.0162 | 55.86 | 0.90 |
| | Cs | 0.1890 | 69.95 | 13.22 |
| | (Alkaline Earth) | (0.1057) | | (3.83) |
| | Sr | 0.0340 | 33.32 | 1.13 |
| | Ba | 0.0718 | 37.62 | 2.70 |
| | (Te and I) | (0.0559) | | (1.25) |
| | Te | 0.0354 | 20.42 | 0.72 |
| | I | 0.0205 | 25.69 | 0.53 |
| | (Lanthanides) | (0.4499) | | (9.44) |
| | Y | 0.0181 | 19.89 | 0.36 |
| | La | 0.0561 | 22.55 | 1.26 |
| | Ce | 0.1002 | 20.70 | 2.07 |
| | Pr | 0.0515 | 21.75 | 1.12 |
| | Nd | 0.1614 | 20.61 | 3.33 |
| | Pm | 0.0052 | 20.08 | 0.11 |
| | Sm | 0.0469 | 19.94 | 0.94 |
| | Eu | 0.0054 | 28.95 | 0.16 |
| | Gd | 0.0051 | 19.93 | 0.10 |
| | (Others) | (0.9260) | | (9.32) |
| | Zr | 0.1857 | 14.01 | 2.60 |
| | Nb | 0.0000 | 10.83 | 0.00 |
| | Mo | 0.2142 | 9.33 | 2.00 |
| | Tc | 0.0548 | 8.53 | 0.47 |
| | Ru | 0.1960 | 8.12 | 1.59 |
| | Rh | 0.0588 | 8.29 | 0.49 |
| | Pd | 0.1610 | 8.85 | 1.43 |
| | Ag | 0.0166 | 10.28 | 0.17 |
| | Cd | 0.0167 | 13.01 | 0.22 |
| | In | 0.0013 | 13.29 | 0.02 |
| | Sn | 0.0166 | 16.24 | 0.27 |
| | Sb | 0.0045 | 16.70 | 0.07 |
| Net Volume Change | | | | 25.39 |

### 2.2.6. Correlation of cladding wastage by rare-earth fission products

As stated in Chapter 1, rare-earth fission products attack the cladding and a wastage layer is formed at the inner surface of the cladding. This cladding wastage is called FCCI (Fuel-Cladding Chemical Interaction) hereinafter in this thesis. It is essential to incorporate FCCI into the consideration of the cladding integrity. The mechanistic model for FCCI applicable to wide range of the irradiation condition is too difficult to be constructed because the mechanism of FCCI has not been determined well at this stage. In the post-irradiation examination, some traces of radial migration of rare-earth fission products have been observed, and rare-earth rich layer has been found in the FCCI zone. Related data to quantify these phenomena are, however, not sufficient. Although it is also possible that Pu content in the fuel slug, liner power rate of the fuel pin, etc., affect FCCI behavior, these effects are not clear until now. Therefore, empirical correlation for FCCI has been made in the present study.

It is plausible to assume that FCCI is controlled by the solid-state diffusion mechanism, and local burnup is taken as a time-variable instead of the actual time. Based on these assumptions, the cladding wastage increment $\Delta\delta$ during local burnup increment $\Delta Bu$ is expressed as

$$\Delta\delta = \sqrt{K \cdot \Delta Bu}\,, \tag{70}$$

The rate constant $K$ is obtained by fitting Eq. (70) to the reported experimental data [20,27,28], as follows.

$$K = 1.069 \times 10^{13} \cdot e^{-20000/T}. \tag{71}$$

### 2.2.7. Temperature calculation model

Axial symmetric, r-z 2-dimensional finite element method is applied to calculation of the temperature distribution in the fuel slug and cladding. The crucial factors which affect the temperature distribution are changes in thermal conductivity of the slug due to evolution of the gas bubble and infiltration of the bond sodium. Thermal conductivity of fission gas in the closed bubble and the open pore is much less than that of the fuel alloy, so that the effective conductivity of the irradiated slug is degraded as fractions of the bubbles and open pores increase. On the other hand, it is reported that the bond sodium infiltrates the irradiated slug [25], probably through the



open pore. Since the thermal conductivity of sodium is comparable to the U-Pu-Zr alloys, bond sodium infiltration recovers the degraded conductivity of the irradiated slug. The above effects should be incorporated into the effective thermal conductivity of the slug.

Using the conductivity correction factor $f_{con}$, the effective thermal conductivity of the fuel slug is expressed [29] as

$$k_{eff} = f_{con} \cdot k_f\,, \tag{72}$$

where $k_f$ is the thermal conductivity of the unirradiated fuel alloy. The correction factor $f_{con}$ is recently approximated by the following expression [29], which was derived for spherical gas-filled and irregular sodium-filled pores:

$$f_{con} = \left[1 - 3 \cdot \frac{P_{Na}}{1-P_g} \cdot \frac{1 - \dfrac{k_{Na}}{k_f}}{\dfrac{2}{\varepsilon} + \left(3 - \dfrac{2}{\varepsilon}\right)\dfrac{k_{Na}}{k_f}}\right]\left(1 - P_g\right)^{3/2}, \tag{73}$$

where $k_{Na}$ is thermal conductivity of sodium, $P_g$ volume fraction of gas-filled pore, and $P_{Na}$ volume fraction of sodium-filled pore. The shape factor $\varepsilon$ is taken as $\varepsilon = 1.72$. In the ALFUS model, a part of the existing open pores is assumed to be infiltrated by the bond sodium. Using a volume fraction $F_N$ of the sodium-filled open pores to the total open pores, the volume fractions $P_g$ and $P_{Na}$ are expressed as

$$P_g = \frac{\varepsilon^{cls} + (1 - F_N)\varepsilon^{opn}}{1 + \varepsilon^{total}}\,, \tag{74}$$

$$P_{Na} = \frac{F_N \varepsilon^{opn}}{1 + \varepsilon^{total}}\,. \tag{75}$$

In Eqs. (74) and (75), $\varepsilon^{total}$ denotes total volumetric strain of the slug, $\varepsilon^{cls}$ volumetric strain due to the closed bubbles, and $\varepsilon^{opn}$ volumetric strain due to the open pores. The volume fraction $F_N$ is estimated as $F_N = 0.5$. As shown later in the next section (Fig. 2.3.-9), the open pores occupy approximately 70 to 20 % of the porosity: a volume fraction of the sum of the closed bubbles and the open pores to the swelled fuel. It means that about 35 to 10 % of the porosity is assumed to be infiltrated by the bond

sodium. This estimation is consistent with the following observation results: approximately 15 ~ 20 % of the porosity (in Ref. [25]) and 21 ~ 39 % of the porosity (calculated from TABLE I in Ref. [29]) are infiltrated by the sodium.
The thermal conductivity $k_f$ of the unirradiated U-Pu-Zr alloy is given as a function of Pu content $C_{Pu}$, Zr content $C_{Zr}$, (in atom fraction), and temperature $T$ (K);

$$k_f = 16.309 + 0.02713 \cdot T - 46.279 \cdot C_{Zr} + 22.985 \cdot C_{Zr}^{\ 2} - 53.545 \cdot C_{Pu} \ . \qquad (76)$$

The above correlation has been made by fitting the experimental data for the U-Zr alloys [30,31,32] and for the U-Pu-Zr alloys [33].

### 2.2.8. Adjustment of the model parameters in ALFUS

Based on the theoretical and/or empirical considerations, the following key parameters have been ***determined***:
$\alpha$: the hot press parameter for the open pore volume decrease (Subsection 2.2.2.),
$\varepsilon_1^{sw}$: the threshold gas swelling for open pore formation (Subsection 2.2.3.),
$f^{crack}$: the anisotropy factor in the crack model (Subsection 2.2.4.), and
$\dot{\varepsilon}^{sol}$: the solid FP swelling rate (Subsection 2.2.5.),
although values or correlations for these parameters include uncertainties due to effects of the various factors not considered in the models.

The models in ALFUS include other parameters and fuel alloy properties of which values have been ***assumed*** tentatively because of the lack of relevant data; The diffusion coefficient $D_g$ of the gas atom has been assumed to be equal to the self-diffusion coefficient of γ-uranium (Eq. (41)). The larger number of the bubble class $M$ is preferable to simulate the actual evolution of the bubbles, but $M = 6$ has been assumed to cut down the computing time. The gas amounts $m_i$ of the closed bubbles have been determined as $m_1 = 4.0 \times 10^{-21}$, $m_2 = 1.6 \times 10^{-19}$, $m_3 = 6.4 \times 10^{-18}$, $m_4 = 2.6 \times 10^{-16}$, and $m_5 = 1.0 \times 10^{-14}$, because the observed bubble size is the order of micron meter. In this case, the bubble radii of class 1 to *M-1* are in the range of ~4 nm ~1 μm. The diffusion coefficients $D_i$ of the grain-boundary bubbles has been assumed to be given by Eq. (42) because of insufficient knowledge of the bubble mobility on the boundary.

On the premise that the tentative values and correlations above are used, values of the multiplication factor $C_{adj}$ for the bubble diffusion coefficient (Eq. (42)) and the parameter $m_M$ ("gas amount" of the open pore; Eq. (55)) have been ***adjusted***, as



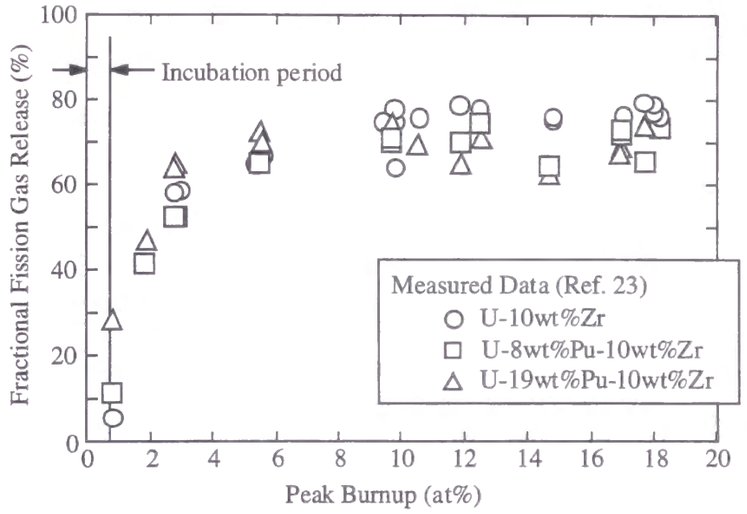


Fig. 2.2.-7 Fission gas release data measured for ~72% smear density pins of the lead test assemblies (Ref. [23]).

follows. Fission gas release data (Fig. 2.2.-7) show sharp increase in the gas release amount after an incubation period (~1 at.% peak burnup). At the higher burnup, the gas release levels off at an asymptotic value of ~60 – ~80 %. The calculated gas release over the whole irradiation period increases with a value of the factor $C_{adj}$, because a larger value of $C_{adj}$ increases the collision and growth rate of the bubbles. On the other hand, the parameter $m_M$ has an influence on the increasing rate of the gas release at the early stage of irradiation. At this stage, the second term in the right hand side of Eq. (51) is dominant compared to the other terms, and varies sensitively with a value of $m_M$ as expected from Eqs. (53) and (56). As a result of the calculations by ALFUS for various values of $C_{adj}$ and $m_M$, $C_{adj} = 20$ and $m_M = 1.015 \times 10^{-14}$ have been appropriate to simulate the measured data presented in Fig. 2.2.-7. If values or correlations of $D_g$, $D_i$, $M$ *and* $m_i$ are determined from theoretical and/or empirical considerations in the future, the adjusted values of $C_{adj}$ and $m_M$ should be revised.

At the present stage, each of the parameter values and the property correlations assumed tentatively cannot be validated separately. In order to validate the ALFUS code as a whole, therefore, the results of the code calculation are compared with the experimental data of the fuel irradiation behavior, which is the superposition of the various phenomena, as reviewed in Chapter 1. The validation of the ALFUS code is described in the next section.

## 2.3. Validation of ALFUS

In order to validate ALFUS, calculations have been performed for the U-19Pu-10Zr (in weight percent) fuel pins of the EBR-II test assemblies designated as X425 and X441. The X425 assembly consisted of 72 % smear density pins and was irradiated until the cladding breach occurred at ~19 at.% [2,34]. The X441 assembly, which included different smear density pins (70, 75, 85 %), was irradiated up to ~10 at.% burnup [2]. The cladding material of both assemblies was the low-swelling martensitic steel, HT9. The values of the model parameters and fuel alloy properties discussed in Section 2.2. are used in all the following ALFUS calculation. Specifications and irradiation conditions of the fuel pins analyzed in this section are summarized in Table 2.3.-1.

Table 2.3.-1 Specification and irradiation condition (Ref. 2) of fuel pins analyzed in the present study

| Assembly No. | X441* | X425 |
|---|---|---|
| Cladding Material | HT9 | HT9 |
| Clad Outer Diameter (mm) | 5.84 | 5.84 |
| Clad Wall Thickness (mm) | 0.38 | 0.38 |
| Fuel Alloy Composition (wt%) | U-19Pu-10Zr | U-19Pu-10Zr |
| Slug Outer Diameter (mm) | 4.67 | 4.32 |
| Fuel Slug Length (mm) | 343 | 343 |
| Smear Density (%) | ~85 | ~72 |
| Peak Linear Power (W/cm) | ~510 | ~400 |
| Peak Cladding Temp. (°C) | ~600 | ~590 |

* Listed only for 85 % smear density pin although X441 includes different smear density pins

### 2.3.1. Fission gas release

Fractional fission gas release calculated for the X425 fuel pin is shown in Fig. 2.3.-1. Release of fission gas starts at ~0.7 at.% peak burnup, which corresponds to onset of interconnection of the closed bubbles (= open pore formation), and levels off at higher burnup. This leveling-off behavior of the gas release is due to stable existence



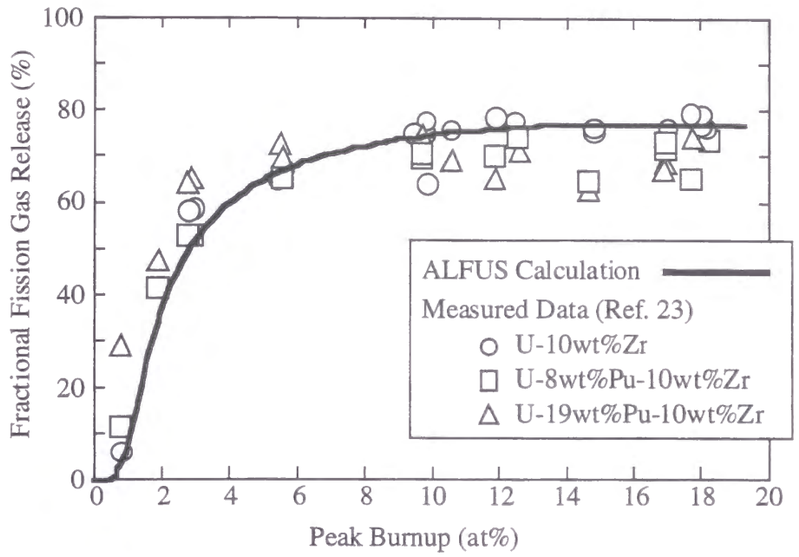


Fig. 2.3.-1 Calculation result of fractional fission gas release for U-19Pu-10Zr(wt%) pin of X425 assembly: measured data are from ~72% smear density pins of the lead test assemblies (Ref. [23]).

of the open pores over higher burnup as indicated later (Fig. 2.3.-9). Figure 2.3.-1 also shows the measured gas release data for ~72% smear density pins of the lead test assemblies designated X419, X420 and X421 [23]. Although the gas release data for the X425 pins have not been published, it is reported in Ref. [2] that they are consistent with the lead test data. The calculated curve reasonably represents the trend of these measured data. The calculated burnup of the gas release onset (the incubation period) is related to the threshold gas swelling $\varepsilon_1^{sw}$ for open pore formation and the gas swelling rate. The agreement between the calculated and test results as shown in Fig. 2.3.-1 indicates that ALFUS calculates a reasonable level of the gas swelling rate.

### 2.3.2. Axial elongation of the fuel slug

The slug axial elongation calculated for the same X425 pin is shown in Fig. 2.3.-2, again in comparison with the measured data for the lead test assemblies. The result obtained for the 85% smear density pin of X441 is also shown in Fig. 2.3.-2. The calculated curves agree well with the measured data. The calculated slug elongation stops at the beginning of the slug-cladding contact stage II (Fig. 2.2.-5), so

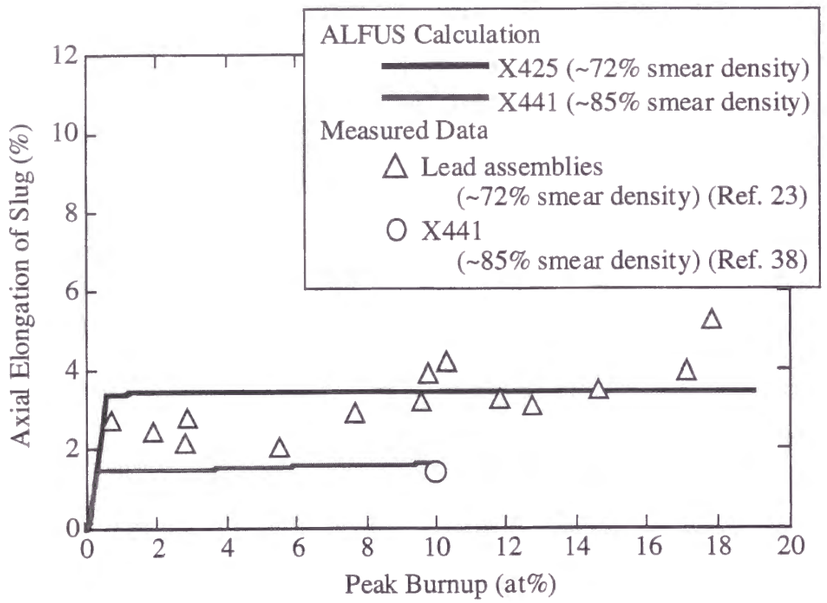


Fig. 2.3.-2 Calculation result of slug axial elongation of the X425 and X441 pins: measured data are from the fuel pins of the lead assemblies (Ref. [23]) and X441 (Ref. [38]).

that the parameter $f^{crack}$ is crucial to simulation of the axial elongation of the slug. Note that the data used to determine an appropriate value of $f^{crack}$ do not include those of the X425 and X441 pins. The reasonable calculation of the gas swelling rate can be confirmed also by Fig. 2.3.-2.

### 2.3.3. Cladding diametral strain and FCMI

#### *2.3.3.1. Axial distribution of cladding strain*

The curves in Fig. 2.3.-3 are the calculated axial distributions of the cladding diametral strain for the X425 pins at 10.4, 15.8 and 18.9 at.% peak burnup. As the swelling of HT9 steel has been neglected in accordance with Ref. [35], the cladding strain calculated in the present study is essentially due only to irradiation creep. In ALFUS, the following correlation of irradiation creep strain rate $\bar{\varepsilon}$ for HT9 is used;

$$\bar{\varepsilon} = \bar{B} \cdot \sigma^{1.5} \cdot \phi t \ , \qquad (77)$$



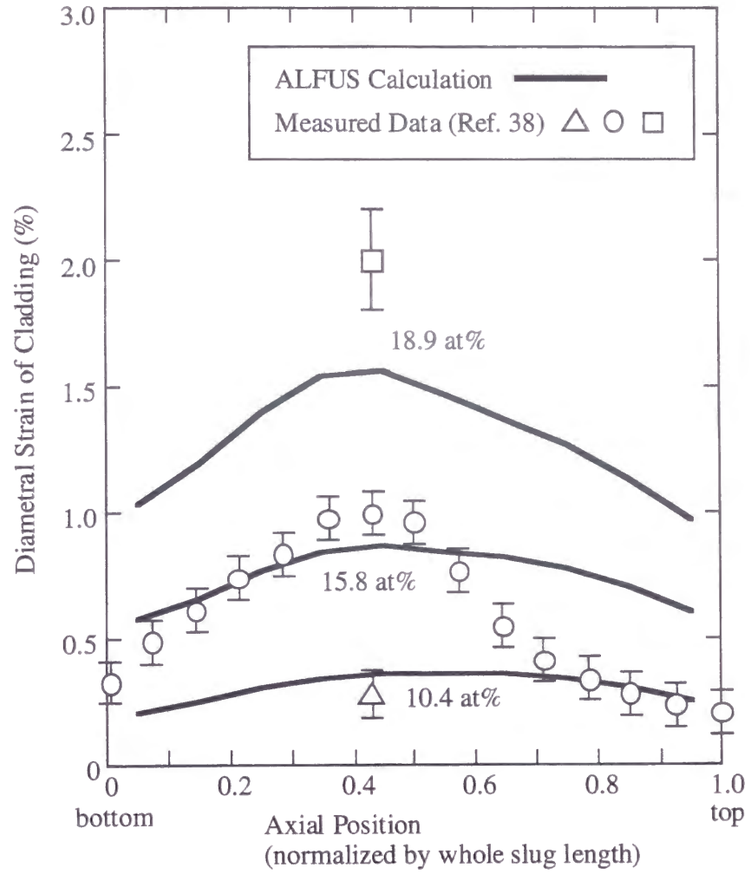


Fig. 2.3.-3 Calculation results and measured data (Ref. [38]) of cladding diametral strain at 10.4, 15.8 and 18.9 at% peak burnup. (X425, smear density ~72%)

where $\sigma$ is the equivalent cladding stress (MPa) and $\phi t$ fast neutron fluence (n/cm2). The following expression for the effective creep coefficient $\bar{B}$ is made by fitting the experimental data reported in Ref. [36] and [37];

$$\bar{B} = \frac{1.575 \times 10^{-26}}{923 - T} \ , \qquad (78)$$

where $T$ is cladding temperature (K). Each calculated strain curve in Fig. 2.3.-3 has a maximum near the core mid-plane, although the effective creep coefficient is larger at

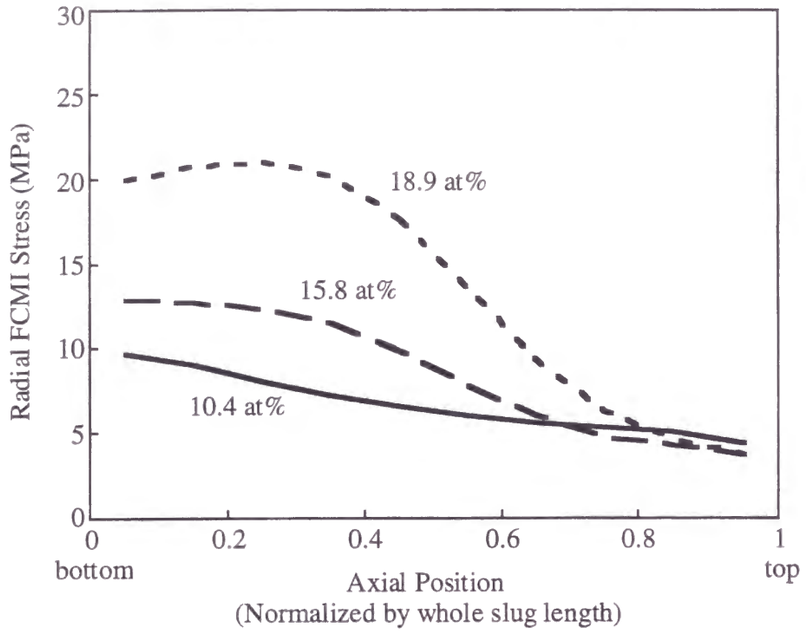


Fig. 2.3.-4 Calculation result of FCMI stress.
(X425, smear density ~72%)

the higher elevation of the cladding where the temperature is higher. This shape of the cladding strain curve is attributed not only to neutron flux distribution similar to the chopped-cosine, also to axial distribution of FCMI stress. Figure 2.3.-4 shows the calculated FCMI stress distributions for the X425 pins at 10.4, 15.8 and 18.9 at.% peak burnup. The volume decrease of the open pores, which accommodates the closed bubble swelling and the solid FP swelling, is slower at the lower (colder) part of the slug where the creep strain rate of the slug is smaller. Therefore, FCMI stress is larger at the lower part of the cladding, despite of the axial distributions of the closed bubble and the solid FP swelling rates, which are proportional to the linear power rate. As a result of combined effects of FCMI, uniform plenum gas pressure, neutron flux distribution, and cladding temperature, the calculated cladding strain shows the above-mentioned distribution.

Figure 2.3.-3 also shows the measured strain data [38], which indicate that the cladding strain increases significantly after ~10 at.% burnup. The ALFUS calculation has qualitatively reproduced the data trend, although the calculation over-predicts the data at the top part of the 15.8 at.% burnup pin. The results for the X441 pins of 85 %



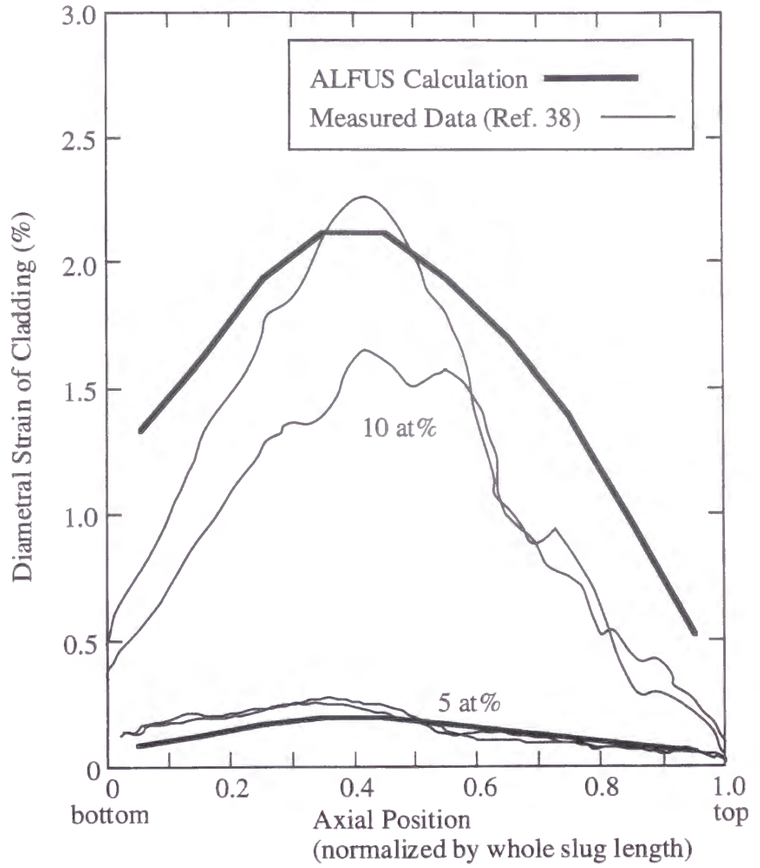


Fig. 2.3.-5 Calculation results and measured data (Ref. [38]) of cladding diametral strain at 5 and 10 at% peak burnup.
(X441, smear density ~85%)

smear density are shown in Fig. 2.3.-5, where large cladding strain has been observed for the 10 at.% burnup pins. The calculated curves (thick solid lines) in Fig. 2.3.-5 generally agree with the measured data [38] although slight over-predictions occur for both the top and bottom parts of the 10 at.% burnup pins. Similar discrepancies between measured and calculated results are also observed in the LIFEMETAL code predictions [2], and can be attributed to uncertainties in the irradiation condition and mechanical properties of HT9, as pointed out in Ref. [2]. Considering these uncertainties, it can be concluded that the cladding strain calculations shown in Figs. 2.3.-3 and 2.3.-5 agree approximately with the measured data.

### *2.3.3.2. Dependency of cladding strain on fuel smear density*

In Fig. 2.3.-6, the measured data [2] of the maximum cladding diametral strain for the X441 pins are plotted against the smear density, together with the ALFUS calculation results. The ALFUS results agree well with the measured data. The large strains observed in the case of the 85 % smear density pins at the higher burnup (1.25 Full Power Years) are caused by a significant level of FCMI. This dependency of the cladding strain on the smear density can be clearly explained by the detailed history of the fuel slug swelling shown in Figs. 2.3.-7 and 2.3.-8, where the radially averaged swelling components at an axial position near the core mid-plane are plotted against burnup. In the case of 85 % smear density (Fig. 2.3.-7), swelling due to the open pores is only ~5% at ~1 at.% burnup when the initial slug-cladding gap is filled with the swollen slug. At the latter stage of irradiation, the open pore volume is replaced by the solid FP swelling, and become insufficient to accommodate further solid FP swelling. It leads to continuous increase in FCMI stress as indicated in Fig. 2.3.-7(b). In the case of lower smear density (Fig. 2.3.-8), the open pore swelling amounts to over 20%, and can serve as a buffer against the solid FP swelling. Consequently, FCMI stress remains at a low level up to 10 at.% burnup (Fig. 2.3.-8(b) ).

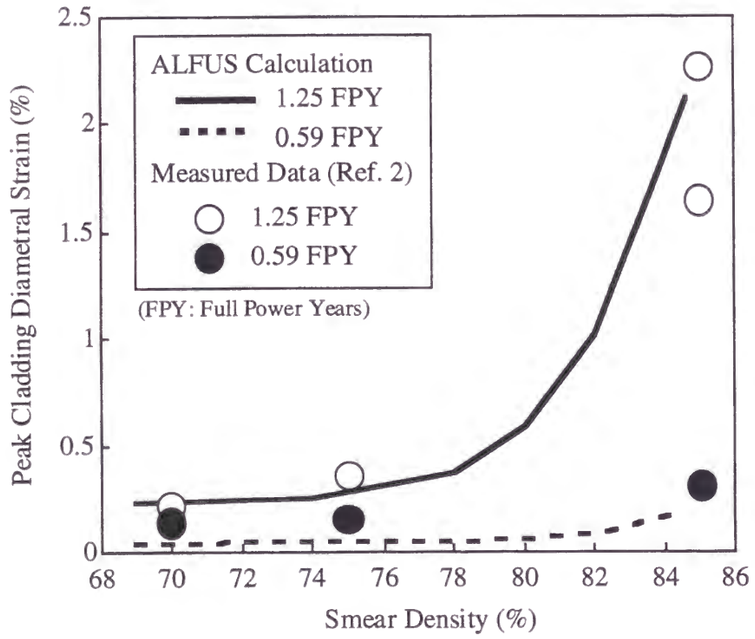


Fig. 2.3.-6 Dependency of peak cladding diametral strain on fuel smear density. (X441 assembly)



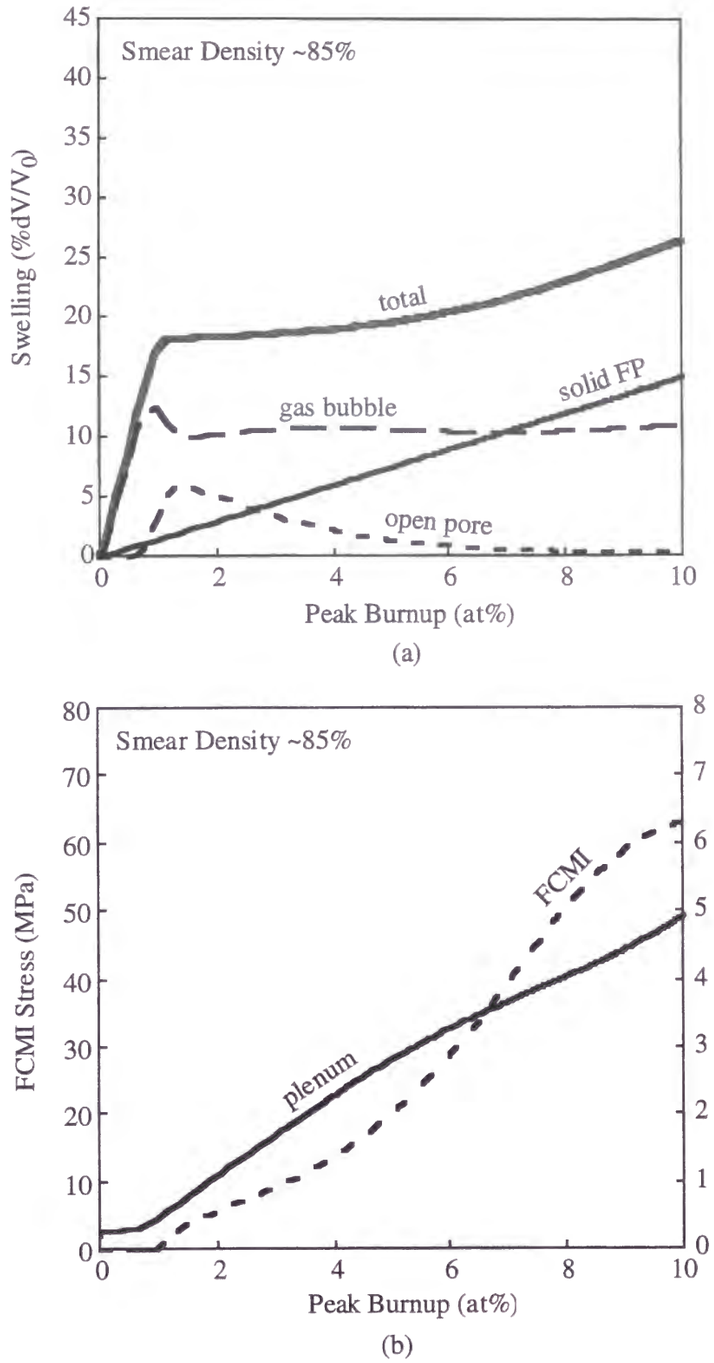


Fig. 2.3.-7 Calculated histories of (a) radially averaged swelling components and (b) FCMI stress and plenum pressure at the axial position of 45% of the slug length from the bottom. (X441, smear density ~85%)

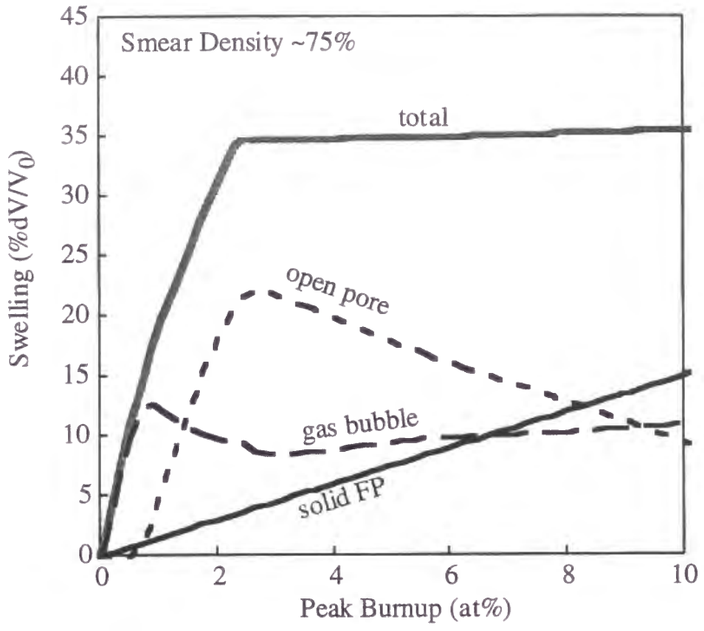


(a)

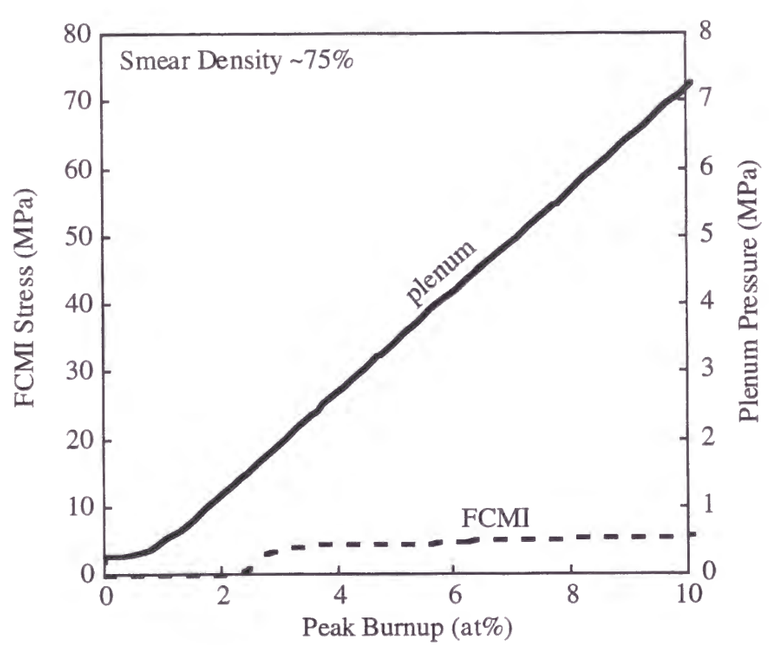


(b)

Fig. 2.3.-8 Calculated histories of (a) radially averaged swelling components and (b) FCMI stress and plenum pressure at the axial position of 45% of the slug length from the bottom. (X441, smear density ~75%)



#### *2.3.3.3. Effect of solid FP accumulation at higher burnup*

At a very high burnup, significant FCMI can occur even in the case of low smear density pins because of the accumulation of the solid FPs. This effect of the solid FP swelling at higher burnup is illustrated in Fig. 2.3.-9, which shows the calculated swelling history in the very high burnup pin of the X425 assembly. In this case, although decrease in the open pore volume accommodates the solid FP swelling until ~13 at.% burnup, the remaining volume of the open pores becomes too small at the higher burnup. This leads to significant increase in the FCMI stress as indicated in Fig. 2.3.-9(b). This mechanism explains the increase in the measured cladding strain data after ~10 at.% burnup, which is shown in Fig. 2.3.-3.

### 2.4. Validity and applicability of ALFUS

In the ALFUS models described in Section 2.2, the values of the model parameters: $\varepsilon_1^{sw}$, $\alpha$, $\dot{\varepsilon}^{sol}$ and $f^{crack}$ can be determined based on theoretical or experimental considerations. However, some mechanisms of the irradiation behavior, such as the intragranular gas behavior, the open pore formation, and the radial cracking, etc., cannot be identified and some of the relevant physical properties of the fuel alloy cannot be determined, because of the lack of the experimental data. In these cases, the simplified but reasonable mechanisms have been assumed, and the empirical correlations and/or the parameters have been introduced into the models. The parameter values have been adjusted so that the models can be consistent with the reported experimental results, whereby various effects on the irradiation behavior are implicitly incorporated into the models. Consequently, the results of the ALFUS calculations are in fair agreement with the measured data for the U-Pu-Zr ternary fuels of different design specifications: smear density range of 70 – 85 %, peak burnup up to ~19 at.%, and peak linear power rate of ~510 and ~410 W/cm. It can be concluded that ALFUS is valid for irradiation behavior analysis of the metallic fuel pins. Moreover, the swelling component histories calculated by ALFUS can reasonably explain the dependency of the measured cladding strain data on burnup and initial smear density. The methodology developed for ALFUS can be a basis for the design procedure which can optimize the metallic fuel pin geometry: for example, smear density, plenum volume and cladding thickness, etc., in order to achieve a target burnup at a certain temperature.

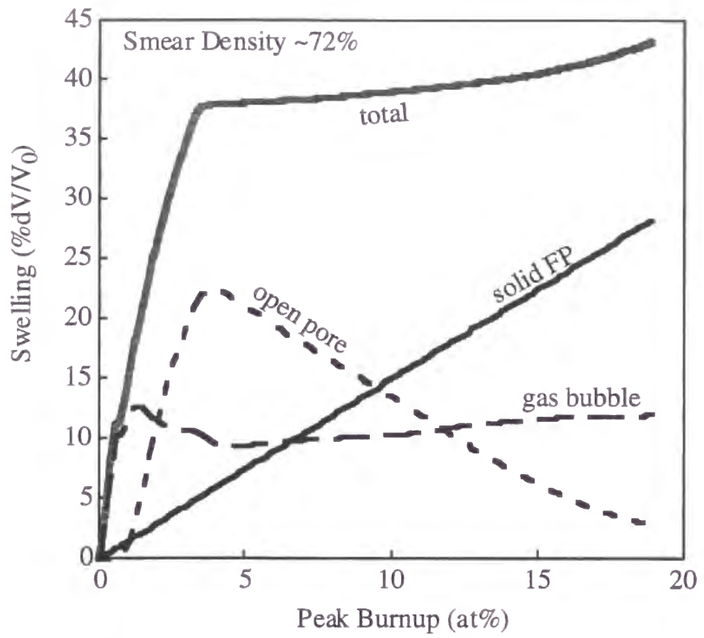


(a)

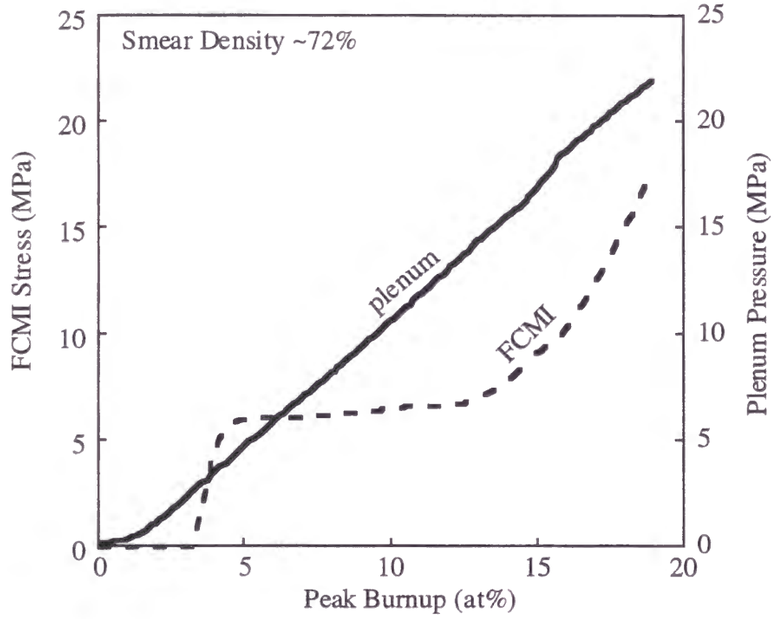


(b)

Fig. 2.3.-9 Calculated histories of (a) radially averaged swelling components and (b) FCMI stress and plenum pressure at the axial position of 45% of the slug length from the bottom. (X425, smear density ~72%)



There is, however, room for further improvement in the current version of ALFUS. In order to improve performance of the ALFUS code, some of the physical properties of the fuel alloy should be measured and the assumed fundamental mechanisms of irradiation behavior must be clarified. When the models are improved based on the measured physical properties and the clarified mechanisms, the ALFUS code will become applicable to the broader range of the fuel specifications and irradiation conditions. The irradiation tests will be necessary to validate these models and confirm the applicability of ALFUS. The following are some of the models of which improvements would be recommended. Presentation of them are useful to illustrate the performance limit of the current version of ALFUS and to give the guidelines for the code improvements in the future.

***Fission gas behavior***

In the gas swelling model (Subsection 2.2.3.), the intragranular and grain-boundary gas models for the oxide fuels have been adopted. The applicability of these models to the metallic fuel should be checked because the U-Pu-Zr fuel alloy shows the multi-phase structure. The fission gas behavior at the phase-boundary may be different from that at the grain-boundary.

The mobility of the grain-boundary bubbles has been assumed independently of the characteristics of the boundary; the diffusion coefficient of the grain-boundary bubble has been given by the same formulation as that of the intragranular bubble. The levels of these diffusion coefficients have been adjusted so that the trend of the fission gas release data can be reproduced (Subsection 2.2.8.). This adjustment should be validated by quantifying the various effects on the diffusion coefficients, which include the effects of irradiation and the fuel alloy structure. This quantification needs measurements of the physical properties, such as the diffusion coefficient of the fission gas atom, the surface diffusion coefficient of the fuel alloy, etc.

The formulation of the bubble collision rate assumed in the model is based on the theory for the coagulation of the colloid particles [39]. Although this assumption may hold in the case of the smaller bubbles in the isotropic, homogeneous medium, the applicability of this theory to the bubbles in the alloy of the polycrystalline or multi-phase structure is an open issue. The local creep deformation and fracture of the fuel alloy matrix may influence the collision and growth process for the larger (the order of micron meter) bubbles and the mechanism of the open pore formation. The number of

the class of both the intragranular and grain-boundary bubbles should be increased so that the calculation results become independent of the classification.

***Tearing and local cracking***

As stated in Subsection 2.2.4., the tearing (cavitation) at the grain- or phase-boundaries may occur due to anisotropic irradiation growth of α-U crystals. Local stress may also cause small cracks in the porous fuel slug. The concept of the effective slug radius (Subsection 2.2.4.) can be considered to include the strain due to the tearing and local cracking. The tearing and local cracking will not only increase the fuel slug strain, but also promote the closed bubble coalescence and the open pore formation. One may consider that the effects of the tearing and local cracking are implicitly incorporated into the model where the probability of the open pore formation is related to the gas swelling (Eq. (58) in Subsection 2.2.3.). However, the threshold gas swelling for the open pore formation in Eq. (58) has been given on the basis of the reported experimental data of fission gas release, but not determined based on the fundamental mechanisms. Quantification of the effects of the tearing and local cracking will need a mechanistic approach with consideration of the irradiation growth and damage, phase structure of the fuel alloy, local stress in the porous fuel slug, etc.

***Fuel constituent migration***

In these ten years, the attempts to model the fuel constituent migration have been made [6,40,41]based on the thermo-diffusion theory. Relevant diffusion data, such as interdiffusion coefficients in the U-Zr [42,43], U-Pu [44] and U-Pu-Zr [45] alloys, have also been measured. These data are still insufficient to describe the migration phenomenon completely. The heat of transport in the U-Pu-Zr system under a temperature gradient and the thermochemical assessment of the U-Pu-Zr alloys are desired, in addition to accumulation of the diffusion data.

The stress-strain analysis and the gas swelling model in ALFUS are not linked with local change in the fuel composition due to the fuel constituent migration. This is because the composition dependencies of the mechanical and physical properties of the fuel alloys are not clarified at this stage. The creep strain rate and other mechanical properties vary obviously with the fuel composition. Measurements of these properties are required to analyze the effects of the constituent migration on the structural behavior of the fuel slug.



***Fuel restructuring***

The cross section of the irradiated fuel indicates that the microstructure of the slug varies with the radial position or temperature [21,46]: spherical pores in the central Zr-rich zone, smaller but high number density pores in the intermediate Zr-depleted zone, and highly distorted, coarse cavities in the outermost zone. (The latter coarse cavity formation will be the results of the irradiation growth of the grain.) This zone formation or restructuring of the fuel may be related to the fuel constituent migration and the simultaneous phase change. For example, diffusion of U is much faster than that of Zr in the U-Zr binary system [47], which causes the vacancy flux in the direction opposite to the U flux (the Kirkendall effect). This kind of difference in the alloy constituent flux may also occur in the ternary U-Pu-Zr alloy under a temperature gradient, and cause the vacancy flow. The gas bubble nucleation would be closely related to the vacancy concentration.

***Accumulation of non-gaseous fission products***

The rate of the solid FP swelling, 1.5 volume % per at.% burnup, (Subsection 2.2.5.) has been determined based on the burnup calculation for the U-Pu-22.5 at.% Zr alloy fuel. It has also been assumed that all the non-gaseous fission products contribute to the solid FP swelling, which gives the upper bound of the solid FP swelling rate. If the distribution of the fuel constituents and fission products in the fuel slug, including transfer of alkali and alkaline-earth elements to the bond Na, is known well, a more reasonable rate of the solid FP swelling can be determined.

## 2.5. Conclusions for Chapter 2

An irradiation behavior analysis code for metallic fast reactor fuel, ALFUS, has been developed in order to understand the irradiation behavior comprehensively, analyze cladding stress and strain properly, and establish the design procedure for the metallic fuel pin. The irradiation behavior of the ternary fuel pins of various design specifications has been analyzed with ALFUS. From the results of the analysis, the following behavior of the cladding stress and strain has been shown;

(1) The FCMI stress is larger at the lower part of the slug mainly due to the lower rate of the open pore volume decrease. As a result of this axial distribution of FCMI, coupled with the axial profile of the neutron flux and the cladding temperature, the cladding diametral strain takes a maximum value near the core mid-plane in the case of the HT9 cladding.

(2) In the case of the higher (≥ ~85 %) smear density, the open pore volume is insufficient to accommodate further solid FP swelling, so that FCMI increases continuously. In the case of the lower (~75 %) smear density, the open pore volume can serve as a buffer against the solid FP swelling, and FCMI remains at a low level up to a moderate level (~10 at.%) of burnup.

(3) Even in the case of the lower smear density, significant level of FCMI occurs because of the accumulation of the solid FPs at a higher burnup (≥ ~10 at.%).

The ALFUS calculations are in fair agreement with the measured data for fission gas release, slug axial elongation and cladding deformation. It can be concluded that ALFUS is valid for irradiation behavior analysis of the metallic fuel pin and applicable to a wide range of fuel pin specifications. The methodology developed for ALFUS can be a basis for the design procedure of the metallic fuel pin.

In order to improve performance of the ALFUS code, some of the physical properties of the fuel alloy should be measured, and some of the irradiation behavior mechanisms must be clarified. When the models are improved, the ALFUS code will become applicable to the broader range of the fuel specifications and irradiation conditions. The irradiation tests will be necessary to validate these models and confirm the applicability of ALFUS.

## References


[1] M.C. Billone, Y.Y. Liu, E.E. Gruber, T.H. Hughes, and J.M. Kramer, Proc. Int. Conf. Reliable Fuels for Liquid Metal Reactors, Tucson, Arizona, September 7-11, 1986 (American Nuclear Society, 1986).

[2] R.G. Pahl, C.E. Lahm, H. Tsai and M.C. Billone, Proc. Int. Conf. Fast Reactor and Related Fuel Cycles, Kyoto, Japan, October 28-November 1 (Atomic Energy Society of Japan, 1991).

[3] T. Kobayashi, M. Kinoshita, S. Hattori, T. Ogawa, Y. Tsuboi, M. Ishida, S. Ogawa and H. Saito, Nucl. Technol. 89 (1990) 183.

[4] T. Ogata, M. Kinoshita, H. Saito and T. Yokoo, J. Nucl. Meter., 230 (1996) 129.

[5] T. Ogata and T. Yokoo, Nucl. Technol. 128 (1999) 113.





[6] M. Ishida, T. Ogata and M. Kinoshita, Nucl. Technol. 104 (1993) 37.

[7] T. Nakajima, M. Ichikawa, Y. Iwano, K. Ito, H. Saito, K. Kashima, M. Kinoshita and T. Okubo, Japan Atomic Energy Research Institute Report JAERI-M 9251 (1981).

[8] Y.R. Rashid, H.T. Tang and E.B. Johansson, Nucl. Eng. Des. 29 (1974) 1.

[9] E.E. Gruber and J. M. Kramer, Radiation-Induced Changes in Microstructure: 13th Int. Symp. (Part I), ASTM STP 955 (1987) 432.

[10] S.M. McDeavitt, PhD Thesis, Purdue University (1992).

[11] Y. Tsuboi, T. Ogata, M. Kinoshita, and H. Saito, J. Nucl. Mater. 188 (1992) 312.

[12] M.H. Wood and J.R. Matthews, J. Nucl. Mater. 91 (1980) 35.

[13] J.R. Matthews and M.H. Wood, Nucl. Eng. Des., 56 (1980) 439.

[14] E.A. Brandes, Smithells Metals Reference Book, 6th edition (Butterworth & Co., 1983).

[15] D.R. Olander, "Fundamental Aspects of Nuclear Reactor Fuel Elements," TID-26711-P1 (US Technical Information Center, USERDA, 1976)

[16] E.E. Gruber and J.M. Kramer, J. Am. Ceram. Soc. 70, No.10 (1987) 699.

[17] M.R. Hayns and M.H. Wood, J. Nucl. Mater. 67 (1977) 155.

[18] R.S. Barns, J. Nucl. Mater. 11 (1964) 135.

[19] W. Beere and G. L. Reynolds, J. Nucl. Mater., 47 (1973) 51.

[20] H. Tsai, A.B. Cohen, M.C. Billone, and L.A. Neimark, Proc. 3rd JSME/ASME Joint Int. Conf. on Nuclear Engineering, Kyoto, Japan, April 23-27, 1995, vol. 2, p. 849 (1995)

[21] G.L. Hofman, R.G. Pahl, C.E. Lahm, and D.L. Porter, Metall. Trans., 21A, (1990) 517.

[22] J. Rest, J. Nucl. Mater. 207 (1993) 192.

[23] R.G. Pahl, R.S. Wisner, M.C. Billone, and G.L. Hofman, Proc. Int. Fast Reactor Safety Meeting, Snowbird, 1990, vol. IV (American Nuclear Society, 1990).

[24] D.C. Crawford, S.L. Hays, and R.G. Pahl, Trans. Am. Nucl. Soc., 71 (1994).

[25] G.L. Hofman and L.C. Walters, Metallic Fast Reactor Fuels, Nuclear Materials, Part 1: vol.10A, edited by B.R. Frost (VCH Verlagsgesellschaft, 1994).

[26] A.G. Croff, ORNL/TM-7175, Oak Ridge National Laboratory (July 1980).

[27] A.B. Cohen, H. Tsai and L.A. Neimark, J. Nucl. Mater. 204 (1993) 244.

[28] R.G. Pahl, C.E. Lahm and S.L. Hayes, J. Nucl. Mater. 204 (1993) 141.

[29] T.H. Bauer and J.W. Holland, Nucl. Technol. 110 (1995) 407.

[30] Y. Takahashi, M. Yamawaki, and K. Yamamoto, J. Nucl. Mater. 154 (1988).

[31] Argonne National Laboratory, Chemical Technology Division Annual Technical Report for 1986, ANL-87-19 (1987).

[32] Y.S. Touloukian, R.K. Kirby, R.E. Taylor, and P.D. Desai, Thermophysical Properties of Matter, Thermal Conductivity, Metallic Elements and Alloys I, IFI/Plenum, New York (1970).

[33] Argonne National Laboratory, Reactor Development Progress Report, ANL-7230 (1996).

[34] A.M. Yaccout, S.Salvatores, and Y. Orechwa, Nucl. Technol., 113 (1996) 177.

[35] A.M. Yacout and Y. Orechwa, Trans. Am. Nucl. Soc., 65 (1992) 191.

[36] B.A. Chin, Topical Conference on Ferritic Alloys for Use in Nuclear Energy Technologies, Snowbird, UT (1983) 593.

[37] P.J. Puigh, Effects of Radiation on Materials: 12th Int. Symp., ASTM STP 870 (1985) 7.

[38] M.C. Billone, Argonne National Laboratory, Personal Communication.

[39] S. Chandrasekhar, Rev. Mod. Phys. 15 (1943) 1.

[40] T. Ogawa, T. Iwai, and M. Kurata, J. Less-Common Met. 175 (1991) 59.

[41] G.L. Hofman, S.L. Hayes, and M.C. Petri, J. Nucl. Mater. 227 (1996) 277.

[42] T. Ogata, M. Akabori, A. Itoh, and T. Ogawa, J. Nucl. Mater. 232 (1996) 125.

[43] M. Akabori, A. Itoh, T. Ogawa, and T. Ogata, J. Alloys and Compounds, 271-273 (1998) 597.

[44] M.C. Petri, A.G. Hins, J.E. Sanecki, and M.A. Dayananda, J. Nucl. Mater., 211 (1994) 1.

[45] M.C. Petri and M.A. Dayananda, J. Nucl. Mater., 240 (1997) 131.

[46] R.G. Pahl, D.L. Porter, C.E. Lahm, and G.L. Hofman, Metallurgical Trans. 21A (1990) 1863.

[47] Y. Adda, C. Mairy, and J.L. Andreu, Rev. Metall. 57 (1960) 550.



# Chapter 3.

# Irradiation behavior analysis for a prototypic metallic fuel pin

## 3.1. Objective of the analysis

The performance of the reactor fuel should be discussed not only for the test fuel pins, but also for practical, prototypic design of the fuel pins. In order to evaluate the performance of the metallic fuel, irradiation behavior of a prototypic metallic fuel pin is analyzed in this chapter.

For a commercial fast reactor plant, a higher thermal efficiency is desired, so that the coolant outlet temperature will be higher than ~500 °C, which corresponds roughly to the peak cladding temperature of ~600 °C or higher. Fast reactor designers usually adopt the core height of ~1 m and aim at attaining an average burnup higher than ~10 at.% for commercial use. Although the irradiation tests for the U-Pu-Zr ternary fuel in EBR-II demonstrated high-burnup capability (≻~18 at.% of peak burnup) [1] , peak cladding temperatures for these tests were relatively moderate, ≤ ~600 °C. In the IFR-1 irradiation test [2], the ternary fuel slugs of prototypic length (~914 mm) were irradiated in FFTF, but peak burnup and peak cladding temperature were limited to ~10 at.% and ≤ 608 °C, respectively. The only method to examine irradiation performance of a prototypic fuel pin is prediction or extrapolation by a computer code, based on the irradiation test results. For the present analysis, the ALFUS code has been used.

The ALFUS code was validated by using only the data of the EBR-II irradiation tests as described in Chapter 2; the Pu content of the fuel slug, the slug length, the fuel pin diameter and the peak cladding temperature of the prototypic fuel pin analyzed here are not within the range of those of the EBR-II test pins. In this chapter, however, the ALFUS code is assumed to be applicable to the prototypic pin. This assumption may be reasonable because the measured fission gas release are insensitive to the Pu content [1] and the slug length [2]. The radial temperature gradient and heat generation rate ($W/cm^3$) in prototypic fuel pin are also comparable to those in the EBR-II test pins, although the fuel pin diameter of the prototypic pin is thicker. The peak cladding temperature (at the mid-wall) of the prototypic pin is only ~35 °C higher than that of the X441 pins.

In the following sections, the specifications and irradiation conditions of the prototypic pin are described. The integrity of the prototypic fuel pin is discussed based on

the calculation results for margins to the slug center-line melting and cladding creep rupture.

### 3.2. Conditions for the analysis

#### 3.2.1. Specifications and irradiation conditions of the analyzed fuel pin

A prototypic reactor core with the metallic fuel has been designed in Ref.[3]. The fuel pin having the highest linear power rate in this core is analyzed here. The specifications of the analyzed pin are presented in Table 3.2.-1. The axial profile of the linear power rate is assumed to be "chopped-cosine" of the peaking factor 1.25, as shown in Fig. 3.2.-1. The analysis of the reactor core performance [3] has indicated that the power rate of this fuel pin decreases only to 98 % of the beginning-of-irradiation power, so that the linear power rate of the pin is assumed to be constant. The coolant flow rate is also assumed to be constant over the whole irradiation period (three years), accordingly the cladding temperature is constant. At the end of irradiation, the peak burnup of the pin reaches ~19.5 at.% (pin-average burnup of ~15.6 at.%). To avoid the liquid phase

Table 3.2.-1 Specifications and irradiation conditions of the prototypic metallic fuel pin

| | |
|---|---|
| Cladding material | Ferritic/martensitic steel |
| Clad. outer diameter | 7.1 mm |
| Clad. wall thickness | 0.5 mm |
| Fuel alloy composition | U-14.1Pu-10Zr (wt.%) |
| | U-12.1Pu-22.5Zr (at.%) |
| Fuel slug diameter | 5.283 mm |
| Fuel slug length | 1000 mm |
| Fuel smear density | 75 % |
| Plenum length | 1560 mm |
| Peak linear heat rate | 502 W/cm (constant) |
| Peak clad. inner temp. | 644 °C (constant) |



formation at the fuel slug–cladding interface, the peak inner cladding temperature has been set at 644℃, based on the results of the ex-reactor tests for the U-Pu-Zr / Fe diffusion couples described in Chapter 4.

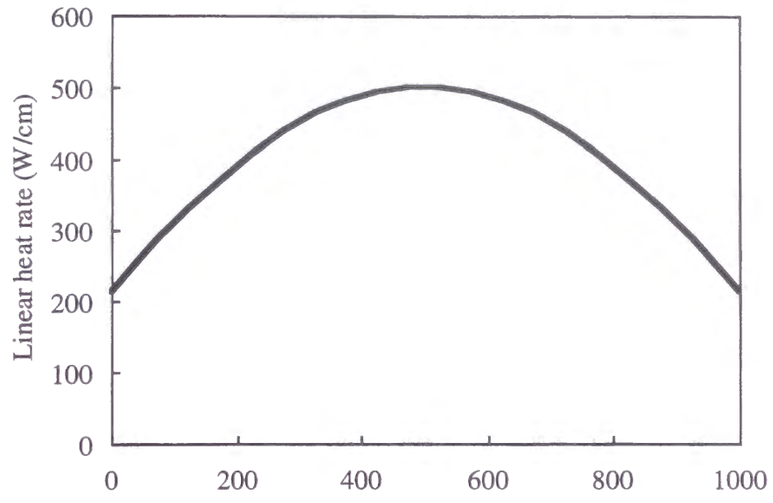


Fig. 3.2.-1 Assumed axial profile of the linear power rate.

Table 3.2.-2 Calculation cases

| Calculation case | Bond Na infiltration | Fuel constituent migration |
|---|---|---|
| Normal operation | | |
| Reference Case | Yes | No |
| Case-1 | No | No |
| Case-2 | No | Yes (Fig. 3.2.-2) |
| 160% over power | | |
| Case-3 | No | No |

### 3.2.2. Calculation cases

Calculations for two extreme cases – Case-1 and Case-2 in Table 3.2.-2 – have also been conducted in the present analysis to examine the effects of the bond Na infiltration and the fuel constituent migration on the temperature distribution in the fuel slug. Note that these two cases are not realistic, but assumed only to examine these effects on the slug temperature. Figure 3.2.-2 shows the hypothetical distributions of the fuel constituents used for the Case-2 calculation. In the Reference Case, the bond Na is assumed to infiltrate 50 % of the open pore volume. In Subsections 3.3.3 through 3.3.5, the calculation results only for the Reference Case are presented.

To show the margin to the slug center-line melting, the Case-3 calculation has been performed under the over-power condition – 160 % of the nominal linear power rate – keeping the coolant flow rate constant. Although the bond Na infiltrates the swollen slug to some extent on the average over the whole slug, fission gas trapped locally in the slug may not allow the bond Na to infiltrate some of the open pores. For the purpose of conservative estimation of the margin to the center-line melting, therefore, the over-power calculation is conducted for Case-1 (no infiltration), when the effective thermal conductivity of the slug becomes worst. The over-power condition has been maintained for 9 seconds

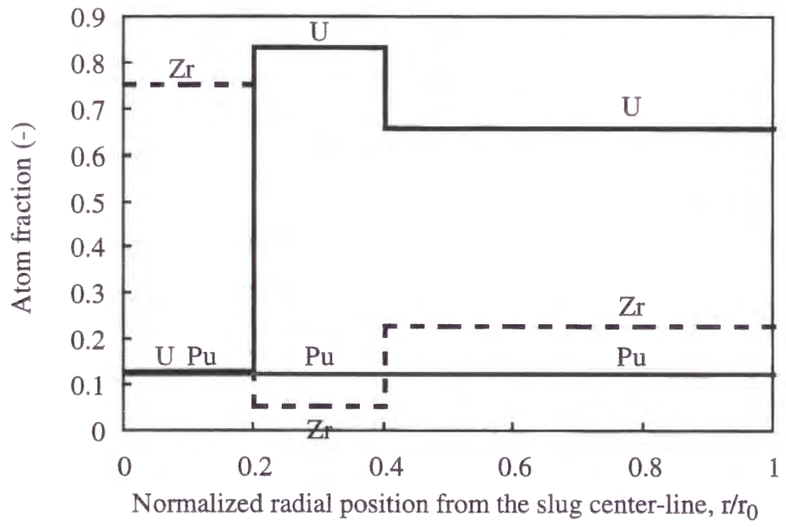


Fig. 3.2.-2 Hypothetical radial distributions of the fuel constituents assumed for all axial positions of the fuel slug over the whole irradiation period in Case 2 calculation.



after the power is increased linearly from 100 % (nominal) to 160 % (see Fig. 3.2.-3), to examine the steady-state temperature distribution.

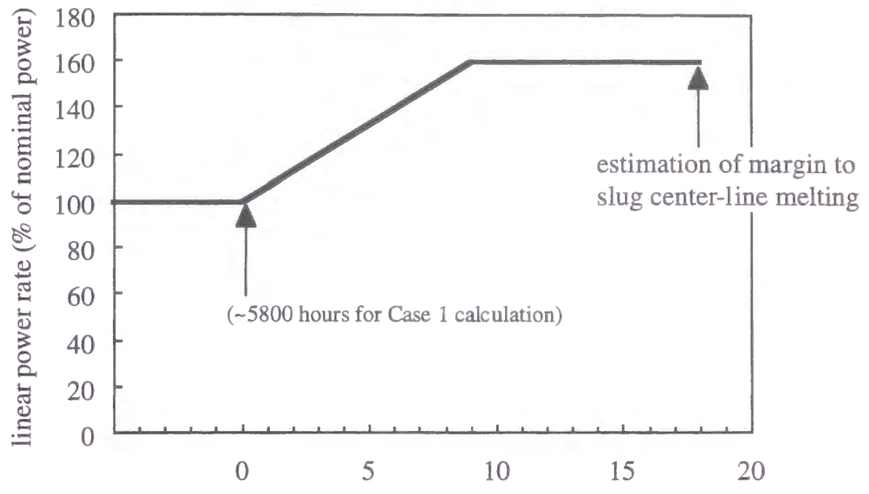


Fig. 3.2.-3 Linear power history for the over-power calculation.

### 3.2.3. Model parameters in ALFUS

As for the key model parameters in ALFUS, threshold gas swelling for open pore formation $\varepsilon_1^{sw}$, compressibility of the open pores $\alpha$, and accumulation rate of non-gaseous fission products $\dot{\varepsilon}^{sol}$ are independent of the specification and irradiation condition of the fuel pin. Therefore, the same values as in Chapter 2 are used here for these three parameters. A value of the anisotropy factor for the crack model $f^{crack}$ is determined as a function of Pu content $C_{Pu}$ and the radial temperature gradient $q/D_0$ (see Fig. 2.2.-6). Because $C_{Pu} = 14.1$ (wt.%) and $q/D_0 \geq 750\,(\mathrm{W/cm^2})$ for the fuel pin analyzed here, a value of 0.75 is used for $f^{crack}$ based on Fig. 2.2.-6. Consequently, the key parameter values used in this analysis are the same as for the EBR-II test pins. As for other parameters and fuel alloy properties in ALFUS, the same values or correlations as those in Chapter 2 are also used here.

### 3.2.4. Cladding material

A swelling-resistant ferritic/martensitic steel is favorable for the metallic fuel cladding because the neutron fluence in the metallic fuel core is usually higher than that in the oxide fuel core. Based on current progress in cladding material development, the cladding material has been assumed to be the advanced ferritic/martensitic steel that has the following creep rupture strength,

$$\log t_R = -21.709 - 0.00853\sigma - 1.5737\log\sigma + 27240/T \ . \qquad (1)$$

This is equivalent to a strength two times higher than that of HT9 [4]. This assumption is realistic because one of the advanced ferritic/martensitic materials, PNC-ODS [5,6], has exceeded this level of creep rupture strength. Using the above creep rupture time $t_R$, the margin to the creep rupture is estimated by the following cumulative damage function (CDF) [7],

$$CDF = \sum \frac{\Delta t}{t_R(\sigma,T)} \ , \qquad (2)$$

where $t_R(\sigma,T)$ (hr) is the creep rupture time at stress $\sigma$ (MPa) and temperature $T$ (K), and $\Delta t$ (hr) is the time interval during which the cladding is under the condition of $\sigma$ and $T$. The CDF value approaching unity means less margin to the creep rupture.

The swelling of the advanced ferritic cladding is assumed to be negligible. The cladding strain discussed here is, therefore, essentially due only to in-reactor creep. An improvement can also be expected for the in-reactor creep property of the cladding. The following function for the effective creep strain $\bar{\varepsilon}_{cr}$ has been used:

$$\bar{\varepsilon}_{cr} = \bar{B} \cdot \bar{\sigma}^{1.5} \cdot \phi t \ , \qquad (3)$$

where $\bar{\sigma}$ and $\phi t$ are the equivalent stress and neutron fluence, respectively. The effective creep coefficient $\bar{B}$ is given by

$$\bar{B} = \frac{1.575\times10^{-26}}{953 - T} \ , \qquad (4)$$

which has been made by shifting the HT9 correlation (see Eq. (78) in Chapter 2) by 30 K.



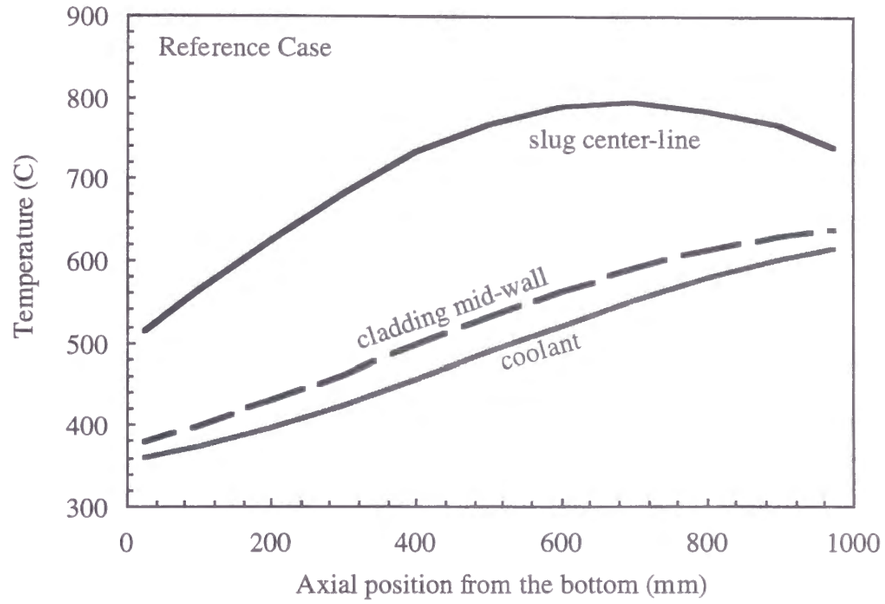


Fig. 3.3.-1 Axial distributions of slug center, cladding and coolant temperatures at 5764 hours (~4.3 at.% peak burnup) for Reference Case.

## 3.3. Results and discussion

### 3.3.1. Fuel temperature

Figure 3.3.-1 shows the axial distributions of the temperatures of slug center-line, cladding mid-wall and coolant at ~5800 hours after the beginning of irradiation for the Reference Case. The slug center-line temperature takes the maximum at 700 mm from the bottom of the slug, although the peak of the linear power rate is at the core mid-plane (500 mm from the bottom). This is the result of the tight thermal coupling between the coolant and the slug due to the Na bonding and high thermal conductivity of the slug.

The histories of the slug center-line temperatures at 700 mm from the bottom for the Reference Case and Case-1 are presented in Fig. 3.3.-2. In the early stage of irradiation, the slug center-line temperature increases because of the formation of less conductive gas bubbles, although the linear power rate and the coolant temperature are constant. For the Reference Case, the slug center-line temperature drops at ~700 hours. This is because open pore formation starts at this time and the effective thermal conductivity

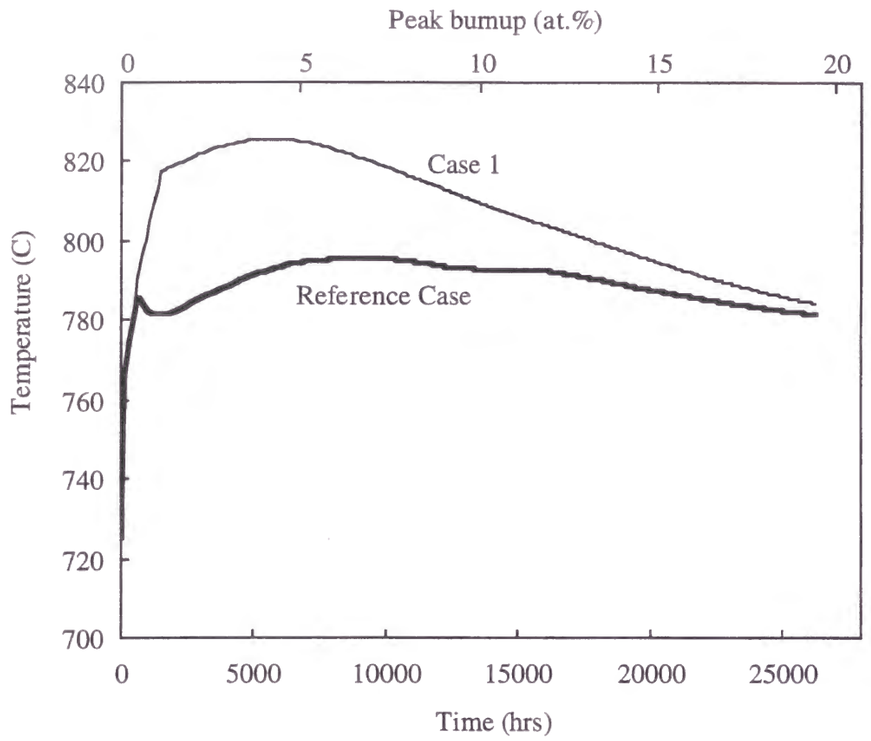


Fig. 3.3.-2 Histories of slug center-line temperatures at the axial position of Z=700 mm from the bottom.

of the slug recovers due to the bond Na infiltration. Radial swelling of the slug begins to be restrained by the cladding at ~2000 hours and the open pore volume starts to decrease, so that a part of the infiltrated Na is expelled from the open pore. Accordingly, the effective thermal conductivity is deteriorated again and the center-line temperature increases gradually from ~2000 hours for the Reference Case. For Case-1, because the bond Na infiltration is not considered, the slug temperature continues to increase in the early stage of irradiation, then reaches the peak (825 ℃) at ~5800 hours. Afterward, the slug temperature decreases as the pores in the slug are replaced with the accumulating non-gaseous fission products (solid FP), which occurs also for the Reference Case (from ~10000 hours). This solid FP accumulation will be presented later (Fig. 3.3.-6).

Figure 3.3.-3 presents the radial distributions of the slug temperatures at ~5800 hours for the Reference Case, Case-1 and Case-2. The difference in the temperature profile between Case-1 and Case-2 is negligible when we consider uncertainties in the physical properties of the slug. The thermal conductivity of the unirradiated fuel alloy (see



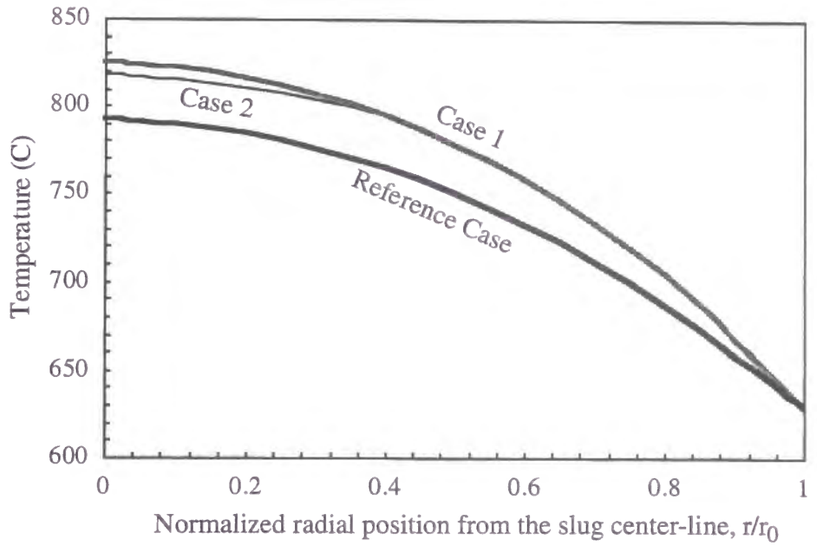


Fig. 3.3.-3 Radial temperature profile at axial positions of Z=700 mm from the bottom at 5764 hours.

Eq. (76) in Chapter 2) of the central Zr-rich zone composition (see Fig. 3.2.-2) is 50 % lower than that of the nominal composition. The heat generation rate in the central Zr-rich zone, however, is lower due to less U content. Conversely, the Zr-depleted zone has higher thermal conductivity but a higher heat generation rate. In this way, the change in thermal conductivity is offset by the change in the heat generation rate. Consequently, the temperature profile for Case-2 becomes close to that for Case-1.

### 3.3.2. Margin to slug center-line melting

Figure 3.3.-4 shows the axial distributions of the temperatures of the slug center, cladding, and coolant in the case of the 160 % over-power condition (Case-3). The over-power is applied for Case-1 at ~5800 hours when the slug center-line temperature becomes the maximum. The peak slug temperature (~1060 ℃) is ~100 ℃ lower than the solidus temperature (~1155 ℃) of the U-~13 at.% Pu- 22.5 at.% Zr alloy [8], even though the bond Na infiltration is not considered. Such a high power level as ~800 W/cm or 160 % of the nominal level is unlikely in the normal reactor operation and the operational transient. It can be concluded, therefore, that the metallic fuel has a sufficient margin to the slug center-line melting.

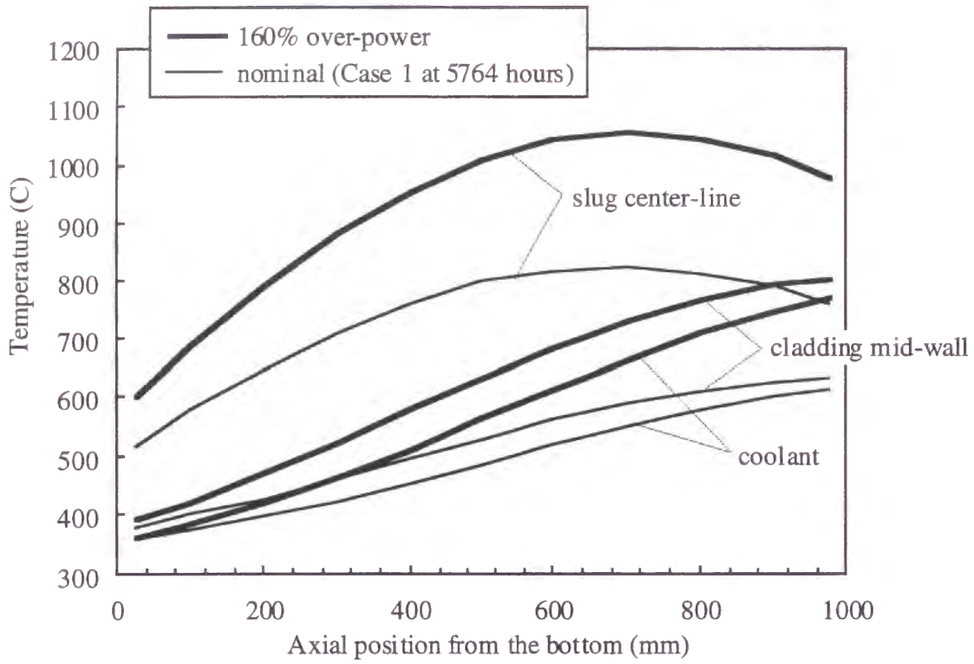


Fig. 3.3.-4 Axial distributions of slug center, cladding, and coolant temperatures at 160% over power.

If the fuel constituent migration is incorporated into the over-power calculation, the temperature distribution in the slug would be almost identical to that in Fig. 3.3.-4, but the solidus temperature of the central Zr-rich zone would increase. In this case, the margin to the center-line melt might be enhanced. The constituent migration phenomenon, however, cannot be predicted well at this stage, so it should not be incorporated into the present over-power analysis.

### 3.3.3. Fission gas release and slug axial elongation

Calculated results for fractional fission gas release and slug axial elongation are presented in Fig. 3.3.-5. These are comparable to the results for the EBR-II test fuel pins (Figs. 2.3.-1 and 2.3.-2 in Chapter 2). This suggests that the gas release and slug deformation of the metallic fuel pin are relatively insensitive to the fuel temperature and the slug length.



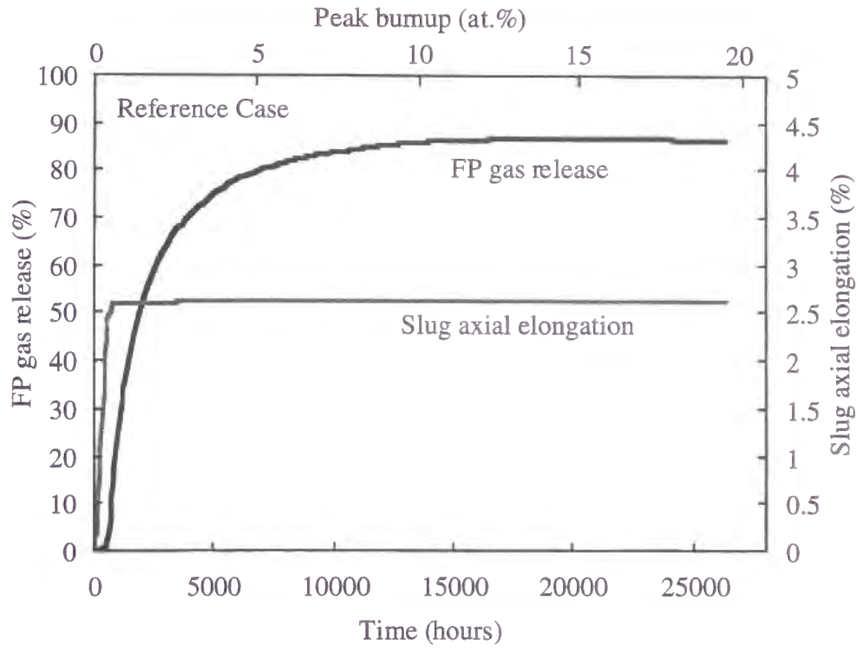


Fig. 3.3.-5 Histories of FP gas release and slug axial elongation.

### 3.3.4. Cladding stress and strain

As explained in Chapter 2, when the fuel smear density is not high (≤ ~75 %), the open pore of sufficient volume is formed in the slug, and excessive gas swelling of the slug is suppressed due to fission gas release through the open pore. The open pore also acts as a buffer to the solid FP swelling. In this way, fuel-cladding mechanical interaction (FCMI) remains at a low level until a moderate burnup (~10 at.%). When a peak burnup becomes higher than ~10 at.%, however, increase in the solid FP swelling cannot be accommodated by the open pore volume decrease, then a significant level of FCMI occurs. This behavior will vary with the axial position of the fuel pin. The validated ALFUS code can predict the axial variation in the swelling behavior and FCMI. Figure 3.3.-6 presents the calculated histories of the radially-averaged swelling components and the FCMI stress (a) near the bottom of the slug, (b) at the core mid-plane, and (c) near the top of the slug. As shown in Fig. 3.3.-6, accumulation of solid fission products causes a significant level of FCMI at the higher burnup (>~10 at.% peak burnup), except at the top of the slug.

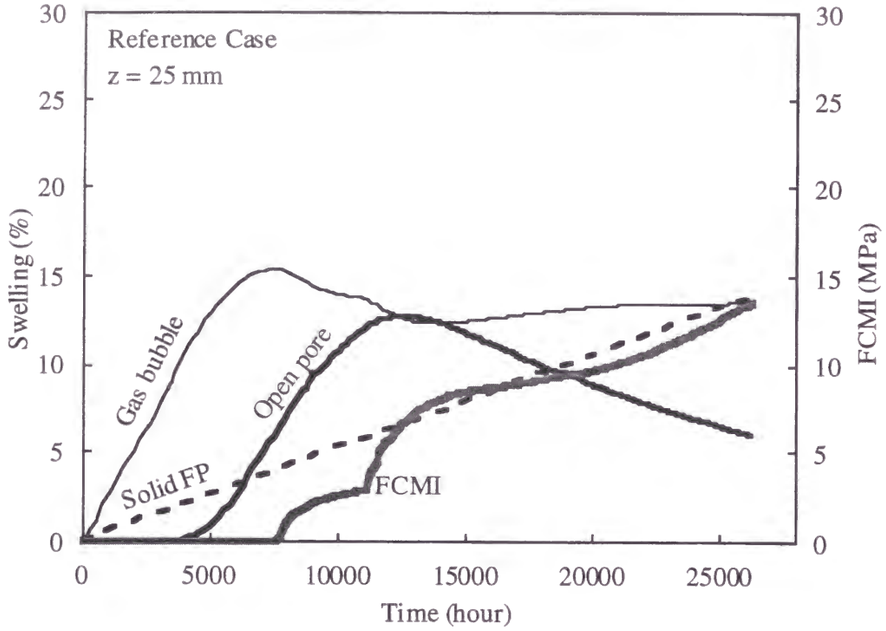


(a) near the bottom of the slug (z = 25 mm)

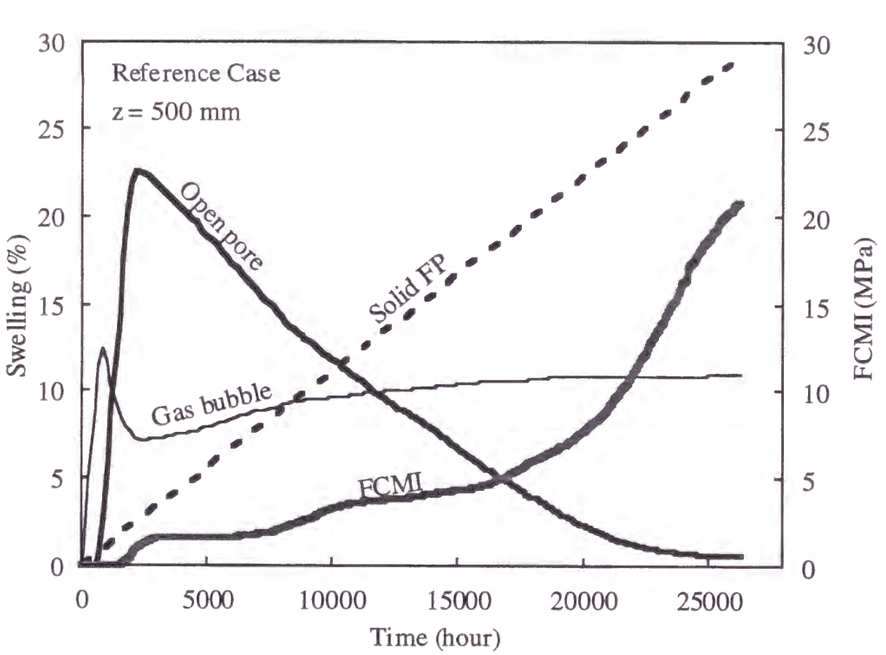


(b) at the core mid-plane (z = 500 mm)

Fig. 3.3.-6 Histories of radially-averaged swelling components and FCMI for Reference Case (a) near the bottom of the slug (z = 25 mm), (b) at the core mid-plane (z = 500 mm), and (c) near the top of the slug (z = 975 mm).



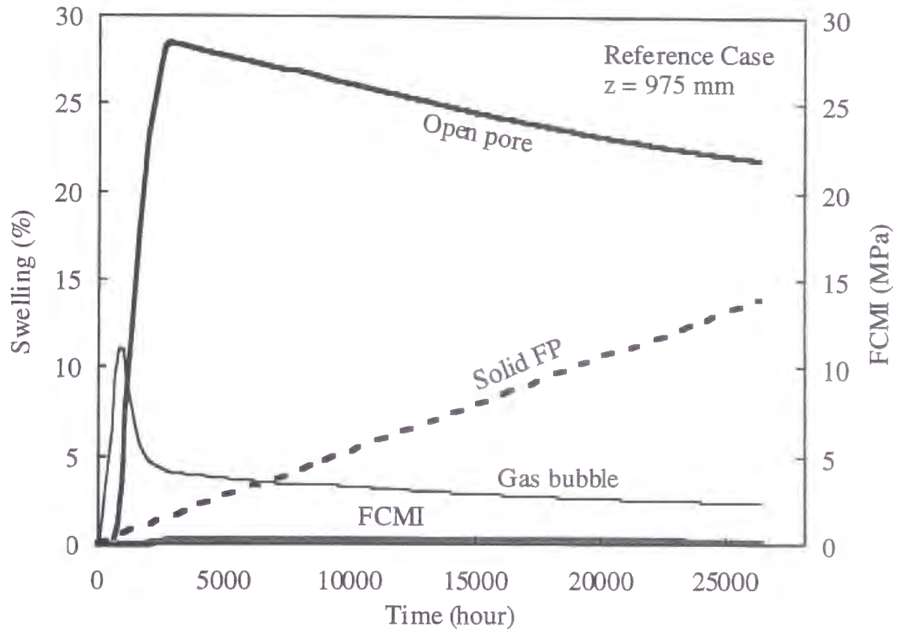


(c) near the top of the slug (z = 975 mm)

Fig. 3.3.-6 (Continued)
Histories of radially-averaged swelling components and FCMI for Reference Case (a) near the bottom of the slug (z = 25 mm), (b) at the core mid-plane (z = 500 mm), and (c) near the top of the slug (z = 975 mm).

Differences among the histories of the swelling components and FCMI at these axial positions (Fig. 3.3.-6 (a) through (c)) are produced by the following reasonable mechanism which is assumed in ALFUS :

- The solid FP swelling is proportional to a burnup rate (linear power rate), namely, lower solid FP swelling near both ends of the slug.
- The rate of open pore volume decrease is controlled by the creep mechanism, and dependent on the slug temperature; the open pore is less compressible at the lower (colder) part of the slug.
- The mobilities of fission gas atoms and bubbles are less at the colder part of the slug (dependent on the self-diffusion coefficient in the fuel alloy), which leads to more fission gas retention, namely, larger gas bubble swelling at the colder part of the slug.

Coupled with the in-reactor creep property assumed for the advanced cladding material (Eqs. (3) and (4)), the above mechanism consequently causes the axial distribution

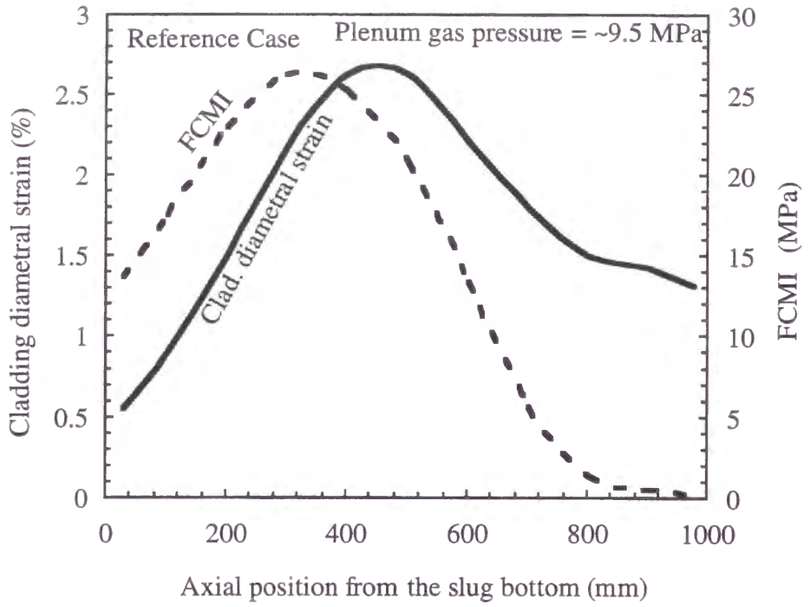


Fig. 3.3.-7 Axial distributions of cladding diametral strain and FCMI at the end of irradiation (~19.5 at% peak burnup) for Reference Case.

of the cladding diametral strain at the end of irradiation, as shown in Fig. 3.3.-7. The FCMI distribution and the plenum gas pressure level are also presented in the figure. The maximum cladding strain of ~2.5 % is caused at the core mid-plane, where the FCMI stress (≥ 20 MPa) is much higher than the plenum gas pressure (~9.5 MPa). This indicates that FCMI is important when the diametral strain is estimated for a swelling-resistant steel cladding. It should be noted that this level of the cladding diametral strain will neither influence the integrity of the coolant flow channel nor cause the excessive bundle-duct interaction.

### 3.3.5. Margin to cladding creep rupture

The axial distributions of CDF and cladding wastage due to FCCI at the end of irradiation are presented in Fig. 3.3.-8. The maximum wastage thickness amounts to ~200 μm, but the peak value of CDF is less than unity. This fuel pin will have a margin to cladding creep rupture during three-year irradiation and be able to attain ~19.5 at.% peak



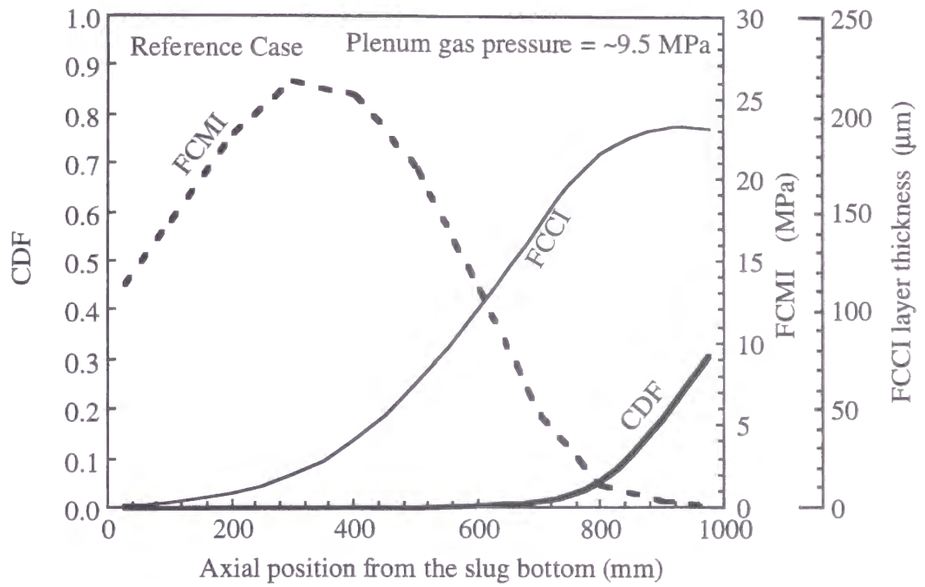


Fig. 3.3.-8 Axial distributions of CDF, FCMI and FCCI at the end of irradiation (~19.5 at% peak burnup) for Reference Case.

burnup (~15.6 at.% pin-average burnup), provided that such a high-strength cladding material as PNC-ODS is brought into practical use.

The CDF value takes the maximum at the top of the slug, where the source of cladding stress is smallest and the FCMI stress (~0.2 MPa) is negligible compared to the plenum gas pressure (~9.5 MPa) as can be seen in Fig. 3.3.-8. This means the degradation of the cladding creep rupture strength with the increasing temperature, assisted by cladding thinning due to FCCI, is more dominant to CDF estimation than the decrease in the FCMI stress. The causes of the negligible level of FCMI at the slug upper part can be attributed to the mechanism stated in Subsection 3.3.4. (see also Fig. 3.3.-6(c)): less accumulation of solid fission products, higher compressibility of the open pore, and less gas bubble swelling. This calculation result suggests that FCMI is less important to the CDF estimation for the metallic fuel clad with the advanced ferritic/martensitic steel.

From the discussion in subsections 3.3.4. and 3.3.5., it can be concluded that the integrity of a prototypic metallic fuel pin can be assured up to high burnup by considering FCMI appropriately in the fuel pin design.

### 3.4. Conclusions for Chapter 3

The following conclusions can be derived from the irradiation behavior analysis of a prototypic metallic fuel pin.

(1) The fuel constituent migration phenomenon has a small influence on the slug temperature prediction.

(2) The slug peak temperature calculated under the 160 % over-power condition is sufficiently lower than the solidus of the fuel alloy, even though the bond Na infiltration is not considered. The metallic fuel has a sufficient margin to the slug center-line melting.

(3) The calculation results for fission gas release and slug axial elongation are comparable to those for the EBR-II test fuel pins.

(4) The cladding diametral strain at the end of irradiation takes the maximum near the core mid-plane, where the FCMI stress is much higher than the plenum gas pressure. This means that FCMI is important when the diametral strain is estimated for a swelling-resistant steel cladding. The predicted level of the cladding diametral strain will neither influence the integrity of the coolant flow channel nor cause excessive bundle-duct interaction.

(5) The value of CDF takes the maximum at the top of the slug, where the FCMI stress is negligible compared to the plenum gas pressure. The degradation of the cladding creep rupture strength with the increasing temperature, assisted by cladding thinning due to FCCI, is more dominant to CDF estimation than the decrease in the source of the cladding stress.

(6) The integrity of a prototypic metallic fuel pin can be assured up to high burnup by considering FCMI appropriately in the fuel pin design.

### References


[1] R.G. Pahl, R.S. Wisner, M.C. Billone and G.L. Hofman, Proc. Int. Fast Reactor Safety Meeting, Snowbird, 1990, vol. IV (American Nuclear Society, 1990).

[2] H. Tsai and L.A. Neimark, Proc. Int. Conf. on Design and Safety of Advanced Nuclear Power Plants, Kyoto, (Atomic Energy Society of Japan 1992) 28.2-1

[3] T. Yokoo, Y. Tanaka and T. Nishimura, CRIEPI Report T88043 (1989) (in Japanese).

[4] M.K. Booker, V.K. Sikka and B.L.P. Booker, Proc. Ferritic Steels for High Temperature Applications, ASM, Metals Park, Ohio (1983) 257.





[5] S. Ukai, T. Nishida, H. Okada, T. Okuda, M. Fujiwara and K. Asabe, J. Nucl. Sci. Technol., 34 (1997) 256.

[6] S. Ukai, T. Nishida, T. Okuda and T. Yoshitake, J. Nucl. Sci. Technol., 35 (1998) 294.

[7] A.E. Walter and A.B. Reynolds, "Fast Breeder Reactors," Pergamon Press (1982).

[8] J.H. Kittel et al., Nucl. Eng. Des., 15 (1971) 373.

# Chapter 4.

## Experimental study on liquefaction of the peripheral region of the fuel slug

### 4.1. Methodology to clarify the conditions for liquefaction

As stated in Chapter 1, the potential for liquefaction of the slug peripheral region should be excluded during normal reactor operation. The conditions for liquefaction, for example, the cladding temperature and the fuel alloy composition, have not been clarified, although several studies [1-6] on the metallic fuel-cladding compatibility were conducted.

The potential for liquefaction in the slug peripheral region will be influenced by fuel design specifications and in-reactor phenomena, which include fuel alloy composition, cladding alloy composition, fuel slug or cladding temperature, linear power rating (temperature gradient), fission products, and neutron irradiation. When the liquefaction phenomenon is assessed, it is important to know the possible phases formed in the reaction zone and their variations with the above factors. Some of the factors may change the diffusivities of the elements in the fuel–cladding system. However, the diffusivity or the reaction rate is not important to the present issue – whether or not liquefaction in the slug peripheral region occurs to any extent. Considering the amount of Pu in the fuel slug and the eutectic point of ~410°C in the Pu-Fe binary system, the Pu content in the fuel alloy will have a significant effect on the liquefaction mechanism. Lanthanide elements, a dominant group of fission products, will be less significant because the solubility of lanthanide elements in the U-Pu-Zr alloys is limited (~0.6 wt.% or less) [7] and the eutectic point in the binary system of any lanthanide element and Fe is higher than that in the Pu-Fe system.

The author recognizes that the mechanism of liquefaction near the cladding can be clarified primarily by

(1) identifying and investigating the phases in the reaction zones formed between the U-Pu-Zr fuel alloys and the Fe-based steels at different fuel alloy compositions (especially Pu contents) and temperatures, and

(2) establishing the related phase diagrams and determining the solidus temperatures of the phases identified in the reaction zones.

Based on the above methodology, a series of ex-reactor experiments have been started. This chapter describes the results of the first diffusion experiment with two couples – U-



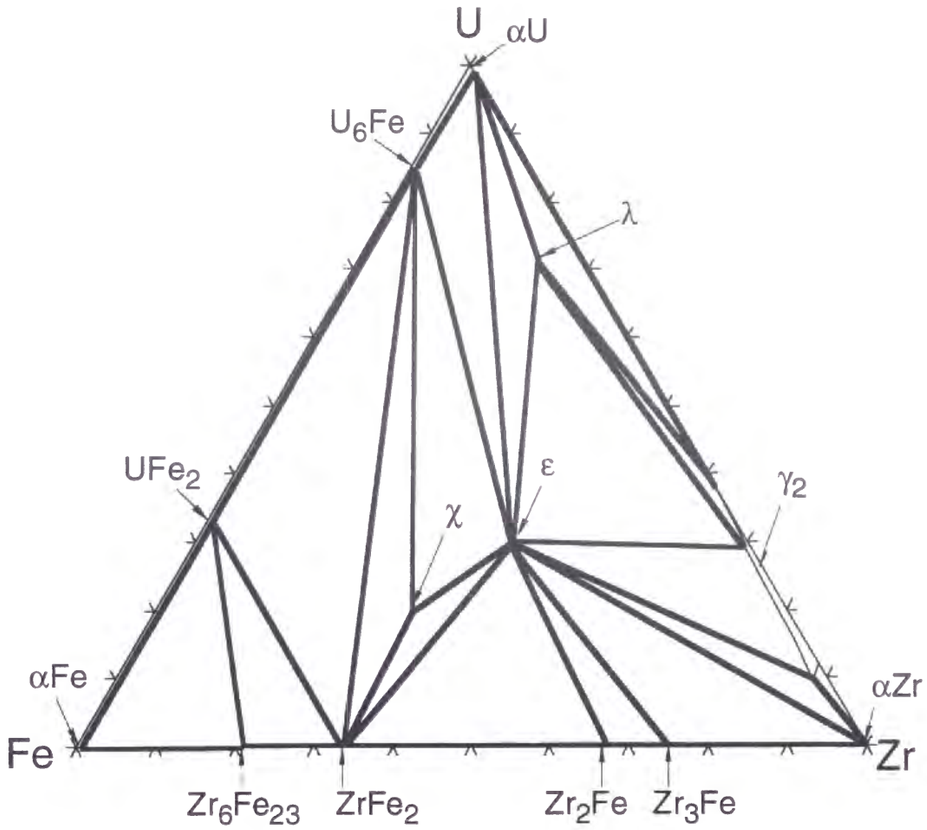


Fig. 4.1.-1 Optimized U-Zr-Fe isotherms at 923 K [5,9,10]. Note that narrow two-phase regions exist between three-phase regions (indicated by bold lines) although these are buried in the neighboring bold lines.

13at.%Pu-22at.%Zr/Fe and U-22at.%Pu-22at.%Zr/Fe [8]. Both couples have been annealed isothermally at 923 K, which is determined based on the test results in Refs. [3,6]. The phases formed in the reaction zones have been identified or estimated from the optimized U-Zr-Fe [5,9,10] and U-Pu-Fe isotherms [11] at 923 K, which are shown in Figs. 4.1.-1 and 4.1.-2. The characteristics of the reaction zone structure and phase compositions are presented in this chapter. The effect of the additives in the cladding material on the potential for liquefaction is also discussed. Finally, current progress in the present test series is mentioned.

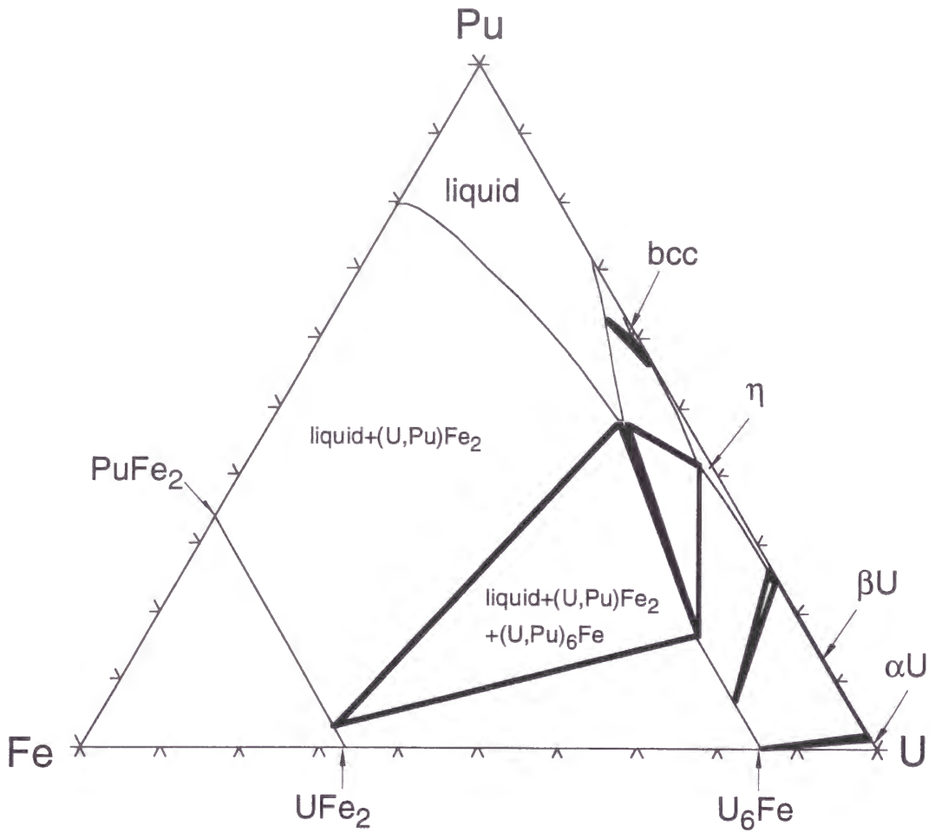


Fig. 4.1.-2 Optimized U-Pu-Fe isotherms at 923 K [11].

### 4.2. Experimental procedure

Two ingots of U-13at.%Pu-22at.%Zr and U-22at.%Pu-22at.%Zr alloys (hereinafter, D1 and D2 alloys, respectively) were prepared from the pure metals U, Pu, and Zr by arc-melting in highly purified argon gas. The arc-melted ingots were inverted and re-melted; the inverting-melting cycle was repeated three or four times to enhance the homogeneity. Oxidation of the ingots during the fabrication process was minimized by arc-melting a pure Zr button before each melting cycle. The O, H, and N contents in the products were less than 200, 15, and 50 ppm, respectively. The compositions of the fabricated ingots are summarized in Table 4.2.-1. Results of the chemical analysis are also presented in the table, and are close to the compositions based on the starting materials.



Table 4.2.-1 Compositions of fabricated alloy ingots

| Alloy | Starting materials (g) | | | Composition (wt.%) | | | Composition (at.%) | | | Chemical analysis (wt.%) | | |
|---|---|---|---|---|---|---|---|---|---|---|---|---|
| | U | Pu | Zr | U | Pu | Zr | U | Pu | Zr | U | Pu | Zr |
| D1 | 12.5 | 2.4 | 1.7 | 75.3 | 14.7 | 10.0 | 64.8 | 12.6 | 22.6 | 75.1 | 14.4 | 10.1 |
| D2 | 7.0 | 2.8 | 1.1 | 64.6 | 25.6 | 9.8 | 55.9 | 22.0 | 22.1 | 64.7 | 24.9 | 9.3 |

These results support the macroscopic homogeneity of the ingots.

To ensure their homogeneity, the D1 and D2 alloy ingots were annealed at 1073 K for about 3 days after being encapsulated in stainless steel cans under an atmosphere of 0.1 MPa argon. The inside surfaces of the cans were lined with tantalum foil then tungsten foil to prevent the ingots from reacting with the stainless steel. After annealing, the cans containing the ingots were quenched in a silicone-oil bath.

A sample of approximately 4 mm × 4 mm × 3 mm was taken from each of the homogenized U-Pu-Zr ingots. Iron disk samples of 5 mm diameter × 3 mm thickness were prepared from a pure Fe (99.995%) rod. Two diffusion couples – D1/Fe and D2/Fe couples – were assembled, a schematic view of which is illustrated in Fig. 4.2.-1. The surfaces of the U-Pu-Zr and the Fe samples that would be the interfaces of the diffusion couples were polished with diamond paste immediately before assembling the couples. The diffusion couples were compressed in a stainless steel holder to ensure complete contact between the U-Pu-Zr and Fe samples. The inside surfaces of the holders were lined with tantalum foil then tungsten foil to prevent the couples from reacting with the

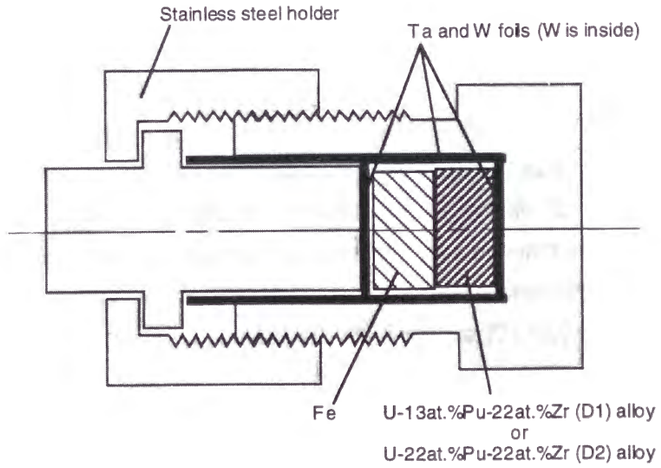


Fig. 4.2.-1 Schematic view of the diffusion couple assembly.

holders. Each of the diffusion couple assemblies was encapsulated in a stainless steel can under an atmosphere of 0.1 MPa argon, and annealed isothermally at 923 K for 48 hours (the D1/Fe couple) and 92 hours (the D2/Fe couple). After annealing, the cans containing the diffusion couples were quenched in a silicone-oil bath.

The annealed couples were cut perpendicularly to the diffusion interface to reveal the reaction zones. The cross sections of the couples were ground and polished for examination by electron probe microanalysis. The compositions of the phases in the reaction zones were measured point-to-point using an energy dispersive X-ray (EDX) detector. For the multi-phase regions, the average compositions were measured by scanning the electron probe within sufficiently large areas. The X-ray spectra obtained were converted to compositions by the ZAF correction program. The X-ray peaks used for quantification were U-Lα, Pu-Lα, Zr-Kα, and Fe-Kα.

All the work including sample preparation, diffusion couple assembly, annealing, and microanalysis was performed in gloveboxes purged with either pure argon or nitrogen gas to minimize oxidation of the samples.

## 4.3. Results

### 4.3.1. U-13at.%Pu-22at.%Zr/Fe couple (D1/Fe couple)

Photograph 4.3.-1 shows the back-scattered electron image of the reaction zone formed in the D1/Fe couple. The reaction zone has been divided into eight regions (regions 1 to 8, see Photo. 4.3.-1) based on the phase structure. Some of the boundaries between the regions are not clear, and the phase structures seem to change continuously over the "boundaries." Even in such cases, preliminary boundaries have been drawn (indicated by the dotted lines in Photo. 4.3.-1) to illustrate the variations of the compositions and the combinations of phases in the regions. Table 4.3.-1 summarizes the phase compositions and the average compositions of the reaction regions. Each of the phases has been identified or estimated (see Table 4.3.-1) based on the composition measurement results and the U-Zr-Fe [5,9,10] and the U-Pu-Fe [11] isotherms at 923 K (Figs 4.1.-1 and 4.1.-2), as follows.



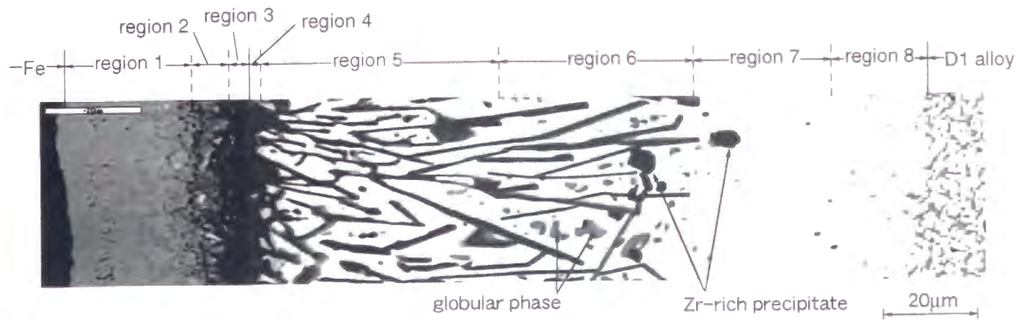


Photo. 4.3.-1 Back-scattered electron image of the reaction zone formed in the U-13at.%Pu-22at.%Zr/Fe diffusion couple.

Table 4.3.-1 Measured phase compositions and identified or estimated phase for the U-13at.%Pu-22at.%Zr/Fe diffusion couple (D1/Fe couple)

| Phase in Photo. 1 | Phase composition (at.%) | | | | Identified or estimated | Region-average composition (at.%) | | | |
|---|---|---|---|---|---|---|---|---|---|
| | Fe | Zr | Pu | U | | Fe | Zr | Pu | U |
| Region 1 | | | | | | 63.7 | 5.0 | 2.1 | 29.2 |
| (Multi-phase)*1) | 67.2 | 3.4 | 2.1 | 27.3 | $(U,Zr,Pu)Fe_2$+$(Zr,U,Pu)Fe_2$ | | | | |
| Region 2 | | | | | | 63.3 | 18.8 | 1.4 | 16.5 |
| (Multi-phase)*1) | 68.5 | 13.2 | 1.6 | 16.7 | $(U,Zr,Pu)Fe_2$+$(Zr,U,Pu)Fe_2$ | | | | |
| Region 3 | | | | | | - | - | - | - |
| (Multi-phase)*1) | 69.5 | 20.7 | 1.1 | 8.6 | $(U,Zr,Pu)Fe_2$+$(Zr,U,Pu)Fe_2$ | | | | |
| Region 4 | | | | | | - | - | - | - |
| (single) | 53.4 | 27.5 | 1.1 | 18.0 | $\chi$ | | | | |
| Region 5 | | | | | | 40.6 | 20.3 | 4.4 | 34.6 |
| bright | 19.5 | 5.4 | 11.4 | 63.7 | $(U,Pu,Zr)_6Fe$ | | | | |
| dark | 51.2 | 28.8 | 1.6 | 18.4 | $\chi$ | | | | |
| Region 6 | | | | | | 32.7 | 18.4 | 7.4 | 41.6 |
| bright | 18.1 | 6.4 | 11.0 | 64.6 | $(U,Pu,Zr)_6Fe$ | | | | |
| dark | 49.9 | 30.3 | 0.8 | 19.0 | $\chi$ | | | | |
| globular | 30.6 | 34.2 | 3.9 | 31.2 | $\varepsilon$ | | | | |
| Region 7 | | | | | | - | - | - | - |
| (single)*2) | 11.7 | 16.9 | 17.6 | 53.8 | $\lambda$ | | | | |
| Region 8 | | | | | | 9.5 | 20.7 | 12.0 | 57.7 |
| brighter | 7.1 | 9.8 | 11.0 | 72.2 | $\zeta$ | | | | |
| bright | 10.5 | 19.9 | 13.5 | 56.1 | $\lambda$ | | | | |
| dark | - | - | - | - | $\gamma$ | | | | |

*1) "Phase composition" for regions 1 to 3 shows the average value of the randomly selected points.

*2) "Phase composition" for region 7 shows the average value of the randomly selected points, although the Pu content decreases from 23 at.% to 13 at.% moving toward region 8.

Regions 1 to 3 in Photo. 4.3.-1 seem to consist of a few phases. Because the sizes of the precipitates in these regions are smaller than the resolution limit of the microanalyzer, the compositions of these precipitates have not been determined directly. The results of the composition measurements for the points randomly selected in these regions indicate, however, that the ratio of (U+Pu+Zr):Fe is approximately 1:2, and that the Zr concentration increases sequentially from region 1 to region 3, replacing U, as can be seen in Table 4.3.-1. The Pu concentrations are always within 2 at.%. These results indicate that each of the regions 1 to 3 consists of the $(U,Zr,Pu)Fe_2$ and the $(Zr,U,Pu)Fe_2$ phases. Note that in this chapter the elements in parentheses ( ) are written in order of decreasing concentration.

The single-phase region 4 is identified as the $\chi$ phase of the U-Zr-Fe system (see Fig. 4.1.-1), the composition of which is U-32at.%Zr-50at.%Fe. The Pu concentration in

region 4 is low (1.1at.%).

The dark phase that extends linearly in regions 5 and 6 in Photo. 4.3.-1 has almost the same composition as the single-phase in region 4, namely the χ phase. The bright phase in regions 5 and 6 has been identified as the $(U,Pu,Zr)_6Fe$ phase from the ratio of (U+Pu+Zr):Fe. The region including the globular precipitates, which seem slightly brighter than the χ phase in Photo. 4.3.-1, has preliminarily been defined as region 6, although the boundary between regions 5 and 6 is not obvious. These globular precipitates have been identified as the ε phase of the U-Zr-Fe system (see Fig. 4.1.-1), because the ratio of (U+Pu):Zr:Fe is close to that of the ε phase with composition U-(33-50)at.%Zr-33at.%Fe.

In the single-phase region 7, the Pu content decreases from 23 at.% to 13 at.% moving toward region 8, with a corresponding increase of U. From the ratio of (U+Pu):Zr:Fe, region 7 is considered analogous to the λ phase of the U-Zr-Fe system (see Fig. 4.1.-1), the composition of which is U-(21~25)at.%Zr-6at.%Fe. In region 7, U of the λ phase seems to be replaced by Pu. Small dark precipitates are seen in regions 6 and 7 in Photo. 4.3.-1. These precipitates are presumably zirconium oxides and have occasionally been observed over the cross sections of the present diffusion couples, for example, in regions 7 and 8 in the D2/Fe couple (see Photo. 4.3.-2(c)).

Region 8 seems to consist of the λ matrix phase and precipitates of the ζ and the γ phases. The ζ and γ phases appear in the unreacted D1 alloy. Although the γ precipitates in region 8 are too small to be quantified, their existence has been estimated from an interpretation of the electron image shown in Photo. 4.3.-1.

### 4.3.2. U-22at.%Pu-22at.%Zr/Fe couple (D2/Fe couple)

The back-scattered electron image of the reaction zone in the D2/Fe diffusion couple is presented in Photo. 4.3.-2(a). The reaction zone has been divided into eight regions as indicated in Photo. 4.3.-2(a). Note that the region number is specific to each diffusion couple, and the region number for the D2/Fe couple does not correspond to the region of the same number for the D1/Fe couple. The preliminary boundaries are indicated by the dotted lines in the figures, as is the case for the D1/Fe couple. Table 4.3.-2 summarizes the phase compositions and the average compositions of the reaction regions. Each of the phases in the reaction zone has been identified or estimated (see Table 4.3.-2) in a manner similar to that for the D1/Fe couple, as follows.



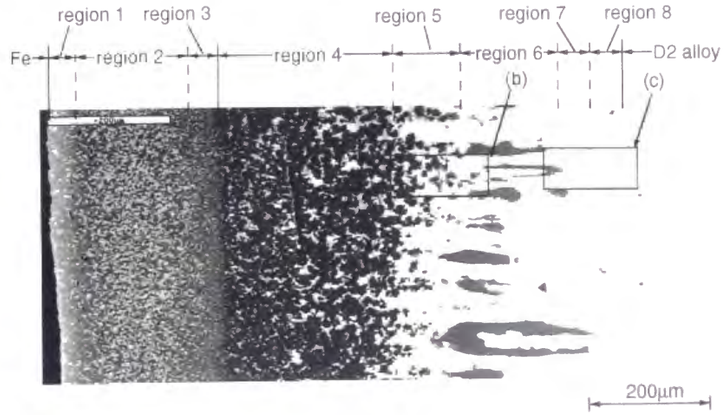


(a) Whole reaction zone

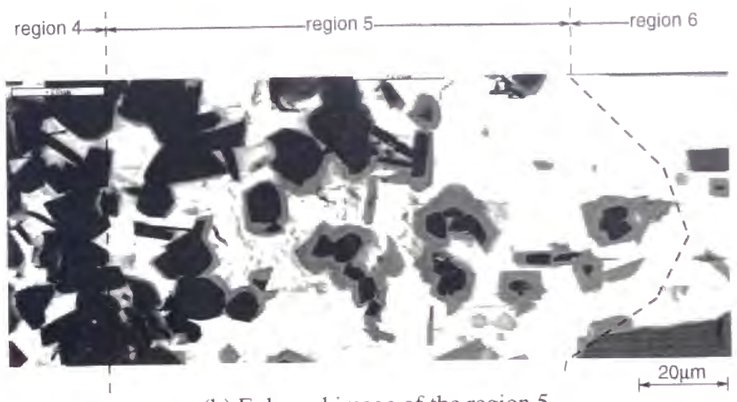


(b) Enlarged image of the region 5

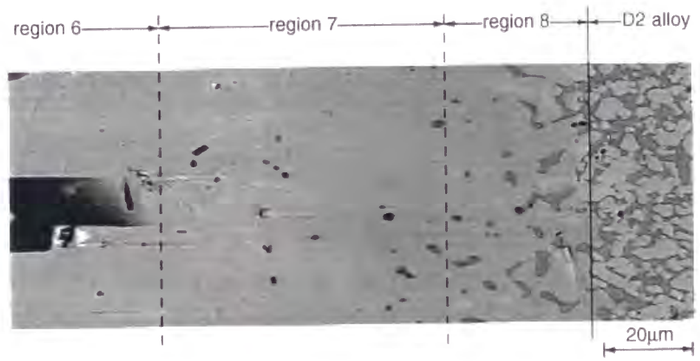


(c) Enlarged image of the regions 7 and 8

Photo. 4.3.-2 Back-scattered electron images of the reaction zone formed in the U-22at.%Pu-22at.%Zr/Fe diffusion couple.

Table 4.3.-2 Measured phase compositions and identified or estimated phase for the U-22at.%Pu-22at.%Zr/Fe diffusion couple (D2/Fe couple)

| Phase in Photo. 2 | Phase composition (at.%) | | | | Identified or estimated | Region average composition (at.%) | | | |
|---|---|---|---|---|---|---|---|---|---|
| | Fe | Zr | Pu | U | | Fe | Zr | Pu | U |
| Region 1 | | | | | | - | - | - | - |
| bright | 17.8 | 4.8 | 20.2 | 57.2 | $(U,Pu,Zr)_6Fe$+liquid | | | | |
| dark | 66.7 | 8.0 | 1.7 | 23.6 | $(U,Zr,Pu)Fe_2$ | | | | |
| Region 2 | | | | | | 54.2 | 8.6 | 9.0 | 28.3 |
| bright | 17.5 | 4.3 | 20.0 | 58.3 | $(U,Pu,Zr)_6Fe$+liquid | | | | |
| dark | 65.7 | 9.2 | 2.1 | 23.0 | $(U,Zr,Pu)Fe_2$ | | | | |
| Region 3 | | | | | | 61.9 | 12.9 | 3.4 | 21.7 |
| bright | - | - | - | - | $(U,Pu,Zr)_6Fe$+liquid | | | | |
| dark | 65.7 | 13.1 | 1.7 | 19.5 | $(U,Zr,Pu)Fe_2$ | | | | |
| Region 4 | | | | | | 61.0 | 16.7 | 5.6 | 16.7 |
| bright*1) | 17.5 | 9.0 | 20.4 | 53.1 | $(U,Pu,Zr)_6Fe$+liquid | | | | |
| dark | 66.0 | 18.5 | 1.6 | 14.0 | $(Zr,U,Pu)Fe_2$ | | | | |
| Region 5 | | | | | | - | - | - | - |
| bright | - | - | - | - | $(U,Pu,Zr)_6Fe$+liquid | | | | |
| dark | 67.6 | 18.6 | 1.6 | 12.2 | $(Zr,U,Pu)Fe_2$ | | | | |
| gray | 66.0 | 8.0 | 2.8 | 23.3 | $(U,Zr,Pu)Fe_2$ | | | | |
| Region 6 | | | | | | - | - | - | - |
| bright | 17.3 | 6.6 | 13.5 | 62.6 | $(U,Pu,Zr)_6Fe$ | | | | |
| dark | 48.9 | 29.2 | 1.2 | 20.6 | $\chi$ | | | | |
| Region 7 | | | | | | 10.9 | 13.8 | 26.4 | 48.9 |
| (single) | 8.9 | 18.4 | 26.0 | 46.6 | $\lambda$ | | | | |
| Region 8 | | | | | | 6.4 | 24.9 | 19.8 | 48.9 |
| brighter | 3.9 | 9.9 | 19.2 | 67.0 | $\zeta$ | | | | |
| bright | 7.5 | 22.9 | 18.8 | 50.8 | $\lambda$ | | | | |
| dark | 4.2 | 47.0 | 20.3 | 28.5 | $\gamma$ | | | | |

*1) The Pu content in the bright phase in region 4 has varied in the range of 16 to 30 at.%.

Regions 1 to 3 show two-phase structures. From the concentration ratio of (U+Pu+Zr):Fe, these three regions are considered to consist of the $(U,Zr,Pu)Fe_2$ and $(U,Pu,Zr)_6Fe$ phases, which appear dark and bright, respectively, in Photo. 4.3.-2(a). The Zr concentration in the $(U,Zr,Pu)Fe_2$ phase increases sequentially from region 1 to region 3, replacing U, as can be seen in Table 4.3.-2. The fraction of the $(U,Pu,Zr)_6Fe$ phase in region 2 is larger than in regions 1 and 3. The Pu content in the bright phases in regions 1 and 2 is about 20 at.%. The composition of the $(U,Pu,Zr)_6Fe$ phase in region 3 could not be determined, but is thought to be equivalent to that of the $(U,Pu,Zr)_6Fe$ phase in region 2. Considering the solubility limit of Pu in the $(U,Pu)_6Fe$ phase (~16 at.%Pu) in the optimized U-Pu-Fe isotherm at 923 K (see Fig. 4.1.-2), one can assume that the bright phases in

regions 1 to 3 included the liquid phase to some extent, although the coexistence of Zr may change the Pu solubility in the $(U,Pu)_6Fe$ phase.

The phase structure of region 4 is similar to that of regions 1 to 3. The results of the phase composition measurements indicate that region 4 comprises the $(Zr,U,Pu)Fe_2$ and the $(U,Pu,Zr)_6Fe$ phases. The Pu content in the $(U,Pu,Zr)_6Fe$ phase has varied in the range of 16 to 30 at.%. This suggests that the $(U,Pu,Zr)_6Fe$ phase in region 4 included the liquid phase at 923 K, and that Pu-rich spots have segregated from the liquid phase during solidification. The $(U,Pu,Zr)_6Fe$ phase in region 4 has an average composition equivalent to that of the $(U,Pu,Zr)_6Fe$ phase in regions 1 and 2, which supports the assumption that the $(U,Pu,Zr)_6Fe$ phases in region 1 to 3 includes the liquid phase.

The enlarged image of region 5 is shown in Photo. 4.3.-2(b). The region showing the peritectic structure has preliminarily been defined as region 5, although the boundary between regions 4 and 5 is not obvious. In Photo. 4.3.-2(b), the gray phase surrounds the dark phase. The phase compositions in Table 4.3.-2 indicate that the dark and gray phases in region 5 are equivalent to the $(Zr,U,Pu)Fe_2$ phase in region 4 and the $(U,Zr,Pu)Fe_2$ phase in regions 1 to 3, respectively. Since such a peritectic structure will not usually be formed in the isothermal system, the $(U,Zr,Pu)Fe_2$ phase in region 5 is considered to have developed while the couple was cooling. Some measurement points in the bright phase in region 5 shown in Photo. 4.3.-2(b) have indicated a concentration ratio of (U+Pu+Zr):Fe=6:1, but others have shown a high-Pu concentration (70 - 80 at.%Pu at maximum). The optimized U-Pu-Fe isotherm at 923 K (see Fig. 4.1.-2) indicates that phases with such high-Pu spots include the liquid phase at 923 K. These high-Pu spots are thought to have segregated from the liquid phase during solidification. The author have estimated, therefore, that at 923 K region 5 consisted of $(U,Pu,Zr)_6Fe$, $(Zr,U,Pu)Fe_2$, and the liquid phase. The peritectic structure has not been observed in regions 1 to 4, although these regions are estimated to have included the liquid phase. This may be attributed to the smaller fraction of the liquid phase in regions 1 to 4 than in region 5.

The two phases observed in region 6 have been identified as the $(U,Pu,Zr)_6Fe$ and $\chi$ phases. The Pu content of the $(U,Pu,Zr)_6Fe$ phase is ~13.5 at.%, which is lower than that of the $(U,Pu,Zr)_6Fe$ (+liquid) phase in regions 1 to 5. Based on the U-Pu-Fe isotherm at 923 K (see Fig. 4.1.-2), the $(U,Pu,Zr)_6Fe$ phase in region 6 does not include the liquid phase.

The enlarged image of regions 7 and 8 is presented in Photo. 4.3.-2(c). The single-phase region 7 is considered the $\lambda$ phase in which 26 at.% Pu has replaced U. The variation of the Pu content was not obvious in region 7, although it was observed in the $\lambda$ single-phase region in the D1/Fe couple.



The boundary between regions 7 and 8 is ambiguous, as shown in Photo. 4.3.-2(c). Region 8 is estimated to consist of the $\lambda$, $\zeta$, and $\gamma$ phases, from measured compositions presented in Table 4.3.-2.

## 4.4. Discussion

### 4.4.1. Effects of the Pu content in the U-Pu-22at.%Zr alloys on the reactions

In Fig. 4.4.-1(a), the average compositions of the regions in each reaction zone are plotted schematically in the U-Pu-Zr-Fe composition tetrahedron, and connected by the thick dotted lines, which are called "schematic diffusion paths" in this chapter. For the regions of which average compositions cannot be measured, the average compositions have been estimated from the phase compositions. The optimized U-Zr-Fe [5,9,10] and U-Pu-Fe [11] isotherms at 923 K are drawn (gray lines in Fig. 4.4.-1(a)) on the U-Pu-Zr-Fe composition tetrahedron. The thin dotted lines in Fig. 4.4.-1(a) indicate the equilibrium phase relations estimated from the present test results. Ogata et al. [4] examined the reactions between the U-23at.%Zr alloys and Fe at 923 K, and Nakamura et al. [5] also analyzed the phase structure of this reaction zone after they established the U-Zr-Fe phase diagram [9,10]. The schematic diffusion path for this U-23at.%Zr/Fe couple is shown on the U-Zr-Fe plane in Fig. 4.4.-1(b). The variation of the reaction zone structure with the Pu content in the initial U-Pu-22at.%Zr alloy of the couple is illustrated by these schematic diffusion paths in the composition tetrahedron. From Fig. 4.4.-1, the following can be derived.

(a) The phase combinations in the reaction zones are dependent on the Pu content in the initial U-Pu-22at.%Zr alloy.

(b) The compositions of the phases near the U-Zr-Fe plane – $(U,Zr,Pu)Fe_2$, $(Zr,U,Pu)Fe_2$, $\chi$, and $\varepsilon$ – are almost independent of the Pu content in the initial U-Pu-22at.%Zr alloy.

(c) The Pu content in each of the Pu-rich phases – $(U,Pu,Zr)_6Fe$ and $\lambda$ – increases with that in the initial U-Pu-22at.%Zr alloy.

(d) In increasing the Pu content in the initial U-Pu-22at.%Zr alloy at 923 K, the first liquid phase in the U-Pu-22at.%Zr/Fe couple is formed when the Pu content in the $(U,Pu,Zr)_6Fe$ phase exceeds the Pu solubility limit (~16 at.%) of this phase.

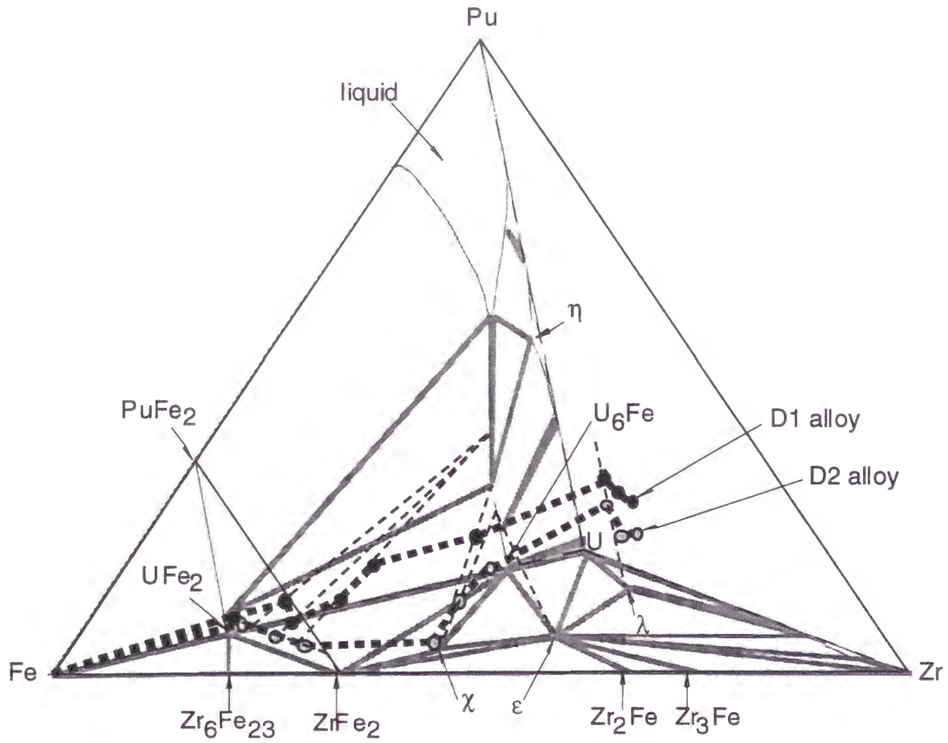


(a) U-Pu-22at.%Zr/Fe couples (D1/Fe and D2/Fe couples)

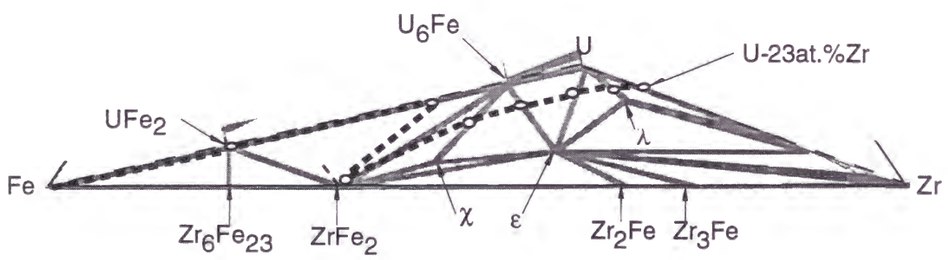


(b) U-23at.%Zr/Fe couple [5]

Fig. 4.4.-1 Schematic diffusion paths at 923 K for
(a) U-Pu-22at.%Zr/Fe couples (D1/Fe and D2/Fe couples), and
(b) U-23at.%Zr/Fe couple [5].



The above (c) and (d) are more clearly illustrated in Fig. 4.4.-2, where the compositions of the phases of (U,Zr,Pu)$Fe_2$, (U,Pu,Zr) $_6$Fe, and λ phases are projected onto the optimized U-Pu-Fe isotherm [11] at 923 K without changing the Fe concentration and the concentration ratio of U:Pu in each phase. One may conclude from Fig. 4.4.-2 that liquefaction in the U-Pu-22at.%Zr/Fe couples is dependent on the Pu content in the initial U-Pu-22at.%Zr alloy, and that the Pu content in the $(U,Pu)_6Fe$-type phase is a crucial factor in determining the conditions that lead to liquefaction. If we assume that the Pu content in the $(U,Pu)_6Fe$-type phase varies linearly with that in the initial U-Pu-22at.%Zr alloy, the extrapolation from the results for D1/Fe couple suggests that the liquefaction will not occur at 923 K when the Pu/(U+Pu) ratio in the U-Pu-Zr alloy is less than 0.22 (U-17at.%Pu-22at.%Zr alloy).

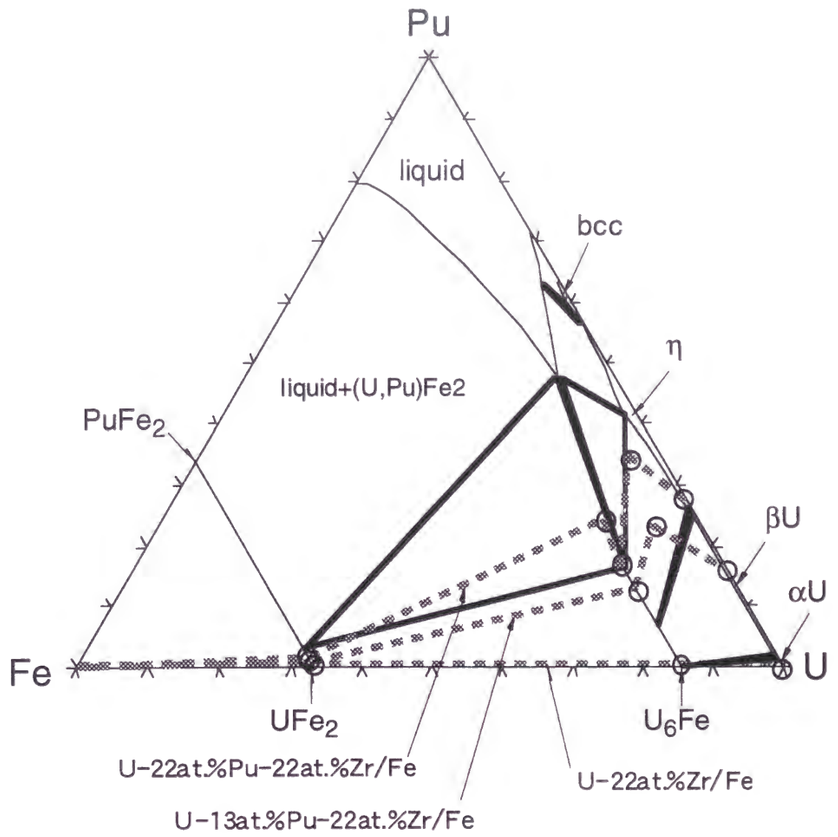


Fig. 4.4.-2 Compositions of the phases of (U,Zr,Pu)Fe2, (U,Pu,Zr)6Fe, and λ, projected on the optimized U-Pu-Fe isotherm at 923 K [11].

### 4.4.2. Effect of the additives in the cladding materials on the liquefaction

Keiser and Petri [3] have conducted a diffusion test using a couple consisting of the U-21at.%Pu-23at.%Zr alloy and HT9, a martensitic stainless steel having an approximate composition of Fe-12wt.%Cr-1wt.%Mo. The U-Pu-Zr alloy that they used is comparable to the D2 alloy in the present tests. They have examined the phase structure of the reaction zone with SEM-EDX after annealing the diffusion couple isothermally at 923 K for 100 hours. The Pu-rich (as high as 90 at.% Pu) phase observed in the U-21Pu-23Zr/HT9 couple is probably identical to the $(U,Pu,Zr)_6Fe$+liquid phase in region 5 of the present D2/Fe couple. The composition of the $(U,Pu,Zr)_6(Fe,Cr)$ phase formed adjacent to the $(U,Pu)(Fe,Cr)_2$ phase in the U-21Pu-23Zr/HT9 couple has been reported to be 52U-24Pu-3Zr-19Fe-0.8Cr (at.%), which is comparable to the compositions of the $(U,Pu,Zr)_6Fe$ phases in regions 1 to 4 of the D2/Fe couple (see Table 4.3.-2) within the accuracy of the SEM-EDX measurement. This similarity in the compositions of the crucial $(U,Pu)_6Fe$-type phases suggests that the additives in the HT9 steel, for example, Cr and Mo, do not significantly affect the potential for liquefaction in the slug peripheral region.

### 4.4.3. Current progress in the diffusion tests

Based on the foregoing discussion, the fuel design specifications to exclude the potential for liquefaction will be clarified by further examination of the Pu content in the $(U,Pu)_6Fe$-type phase for various U-Pu-Zr/Fe couples annealed at different temperatures. The diffusion paths for these couples in the U-Pu-Zr-Fe quaternary or the U-Pu-Fe ternary phase diagrams should be also investigated in a manner similar to that of the present study, after these diagrams are established at various temperatures.

In the experiments for the compatibility of the U-Pu-Zr or U-Zr fuel alloys with the cladding materials, the Zr contents in the fuel alloys have always been set to 10 wt.% (= 22~23at.%) [1-6]. During irradiation, however, Zr in the fuel slug migrates up the radial temperature gradient to the central hotter region ($\gamma$-phase), and hence a Zr-depleted zone is left in the fuel [12,13]. It may be possible that this Zr-depleted zone is formed in the outermost region of the fuel slug under higher temperature conditions and touches the cladding inner surface. The minimum Zr concentration in the Zr-depleted zone has not been determined at this stage. When the potential for liquefaction is assessed, therefore, the reactions between binary U-Pu alloys and Fe should be examined as an extreme case. In this sense, the U-Pu-Fe ternary reactions is more important than the U-Pu-Zr-Fe



quaternary reactions in determining the conditions that lead to liquefaction.

From the standpoint above, ex-reactor tests have subsequently been conducted for the diffusion couples consisting of the U-Pu binary alloys and Fe. The result of these tests has indicated that the liquefaction does not occur below 923 K when Pu/(U+Pu) < 0.25 [14], although theoretical explanation will be required. With this level of Pu content in the metallic fuel, wide range of the reactor core – small scale (~300 MWe) to large scale (>1000 MWe) – can be designed. Even though the peak cladding inner temperature is limited to < 923 K, the core outlet temperature of the coolant can be raised to > 773 K, so that the practical thermal efficiency of the power plant can be obtained.

It should be noted that the influence of neutron irradiation, temperature gradient and fission products on the liquefaction mechanism must be checked by in-reactor tests.

## 4.5. Conclusions for Chapter 4

The reaction zones formed at 923 K in two diffusion couples – U-13at.%Pu-22at.%Zr/Fe and U-22at.%Pu-22at.%Zr/Fe – have been examined. The phases in the reaction zones have been identified or estimated based on the optimized U-Zr-Fe and U-Pu-Fe isotherms at 923 K. The results of the present experiment are summarized as follows.

(1) The liquid phase has been formed in the U-22at.%Pu-22at.%Zr/Fe couple, but not in the U-13at.%Pu-22at.%Zr/Fe couple.

(2) The Pu content in the $(U,Pu)_6Fe$-type phase in the reaction zone increases with the Pu content in the initial U-Pu-22at.%Zr alloy of the couple. The liquid phase in the U-Pu-22at.%Zr/Fe couples is formed when the Pu content in the $(U,Pu)_6Fe$-type phase exceeds the solubility limit of this phase. In other words, the Pu content in the $(U,Pu)_6Fe$-type phase is a crucial factor in determining the conditions that lead to liquefaction. The extrapolation from the results for the U-22at.%Pu-22at.%Zr/Fe couple suggests that the liquefaction will not occur at 923 K when the Pu/(U+Pu) ratio in the U-Pu-Zr alloy is less than 0.22.

(3) The reported composition of the $(U,Pu,Zr)_6(Fe,Cr)$ phase formed in the U-21at.%Pu-23at.%Zr/HT9 couple is comparable to the compositions of the $(U,Pu,Zr)_6Fe$ phases in the present U-22at.%Pu-22at.%Zr/Fe couple. This similarity in the compositions of the $(U,Pu)_6Fe$-type phases suggests that the additives in the HT9 steel do not significantly affect the potential for liquefaction in the slug peripheral region.

(4) The fuel design specifications to exclude the potential for liquefaction will be clarified by further examination of the Pu content in the $(U,Pu)_6Fe$-type phase for various U-Pu-Zr/Fe couples annealed at different temperatures. As a result of the diffusion tests with the U-Pu/Fe couples conducted subsequently based on the standpoint above, it has been indicated that the liquefaction does not occur below 923 K when $Pu/(U+Pu) < 0.25$.

## References


[1] D.D. Keiser Jr. and M.A. Dayananda, J. Nucl. Mater. 200 (1993) 229.

[2] D.D. Keiser Jr. and M.A. Dayananda, Metall. and Mater. Trans. 25A (1994) 1649.

[3] D.D. Keiser Jr. and M.C. Petri, J. Nucl. Mater. 240 (1996) 51.

[4] T. Ogata, M. Kurata, K. Nakamura, A. Itoh and M. Akabori, J. Nucl. Mater. 250 (1997) 171.

[5] K. Nakamura, T. Ogata, M. Kurata, A. Itoh and M. Akabori, J. Nucl. Mater. 275 (1997) 246.

[6] A.B. Cohen, H. Tsai and L.A. Neimark, J. Nucl. Mater. 204 (1993) 244.

[7] M. Kurata, T. Inoue, L. Koch, J-C. Spirlet, C. Sari, J-F. Babelot, CRIEPI Report T92005 (1992) (in Japanese).

[8] T. Ogata, K. Nakamura, M. Kurata and M.A. Mignanelli, to be published in J. Nucl. Sci Technol.

[9] M. Kurata, T. Ogata, K. Nakamura and T. Ogawa, J. Alloys and Comp. 271-273 (1998) 636.

[10] K. Nakamura, M. Kurata, T. Ogata, A. Itoh and M. Akabori, J. Nucl. Mater. 275 (1999) 151.

[11] M. Kurata, K. Nakamura, T. Ogata, and M.A. Mignanelli, CRIEPI Report T98074 (1999) (in Japanese).

[12] D.L. Porter, C.E. Lahm and R.G. Pahl, Metallurgical Trans. 21A (1990) 1871.

[13] G.L. Hofman, S.L. Hays and M.C. Petri, J. Nucl. Mater. 227 (1996) 277.

[14] K. Nakamura, T. Ogata, M. Kurata and M.A. Mignanelli, to be published.




# Chapter 5.

# Conclusions

The computer code, ALFUS, has been developed and validated to comprehensively analyze irradiation behavior of the metallic fuel pin. The ALFUS code has been applied to the analysis of a prototypic fuel pin. An ex-reactor experiment has also been conducted to clarify the conditions for liquefaction of the slug peripheral region. Based on the results of these studies, the performance of the metallic fuel can be summarized from the standpoints of (1) cladding stress and strain, (2) slug center-line melting, and (3) liquefaction of the slug peripheral region, as follows;

(1) Cladding stress and strain:

(1.1) In the case of the higher (≥ ~85 %) smear density, the open pore volume is insufficient to accommodate further solid FP swelling, so that FCMI increases continuously. In the case of the lower (~75 %) smear density, the open pore volume can serve as a buffer against the solid FP swelling, and FCMI remains at a low level up to a moderate level (~10 at.%) of burnup.

(1.2) Even in the case of the lower smear density, a significant level of FCMI occurs due to the accumulation of the solid FPs at a higher burnup (≥ ~10 at.%).

(1.3) The FCMI stress is higher at the lower part of the slug mainly due to the lower rate of the open pore volume decrease. As a result of this axial distribution of FCMI, coupled with the axial profile of the neutron flux and the cladding temperature, the cladding diametral strain takes a maximum value near the core mid-plane. The estimation of FCMI is important to the prediction of the diametral strain of a swelling-resistant ferritic steel cladding.

(1.4) The CDF value of the cladding takes the maximum at the top of the slug. In the cladding creep damage estimation, the decrease in creep rapture strength due to increasing temperature, assisted by cladding thinning due to FCCI, is more dominant than the moderation of FCMI at the slug top part.

(1.5) For the prototypic metallic fuel pin, the advanced ferritic steel will be adopted as the cladding material, and the peak cladding inner temperature is limited to less than ~923 K, considering the potential liquefaction of the slug peripheral region (Chapter

4). In this case, the prototypic metallic fuel pin can be used for three years (the peak burnup ~19 at.% at the end of use) maintaining peak linear power of ~500 W/cm without significant diametral strain and creep rapture of the cladding.

(2) Slug center-line melting:

(2.1) The bond-Na infiltration into the open pores has an influence on slug temperature prediction, but the fuel constituent migration does not.

(2.2) The slug peak temperature calculated under the 160 % over-power condition is sufficiently lower than the solidus of the fuel alloy even if the bond-Na infiltration is not considered. The metallic fuel has a sufficient margin to the slug center-line melting.

(3) liquefaction of the slug peripheral region:

(3.1) At 923 K, the liquid phase has been formed in the U-22at.%Pu-22at.%Zr/Fe couple, but not in the U-13at.%Pu-22at.%Zr/Fe couple.

(3.2) The Pu content in the $(U,Pu)_6Fe$-type phase is a crucial factor in determining the conditions for liquefaction.

(3.3) The extrapolation from the result for the U-13at.%Pu-22at.%Zr/Fe couple suggests that the liquefaction will not occur below 923 K when the Pu/(Pu+U) ratio in the U-Pu-Zr alloy is less than 0.22. In fact, this has been supported by recent experimental results. Even though the peak cladding inner temperature is limited to less than 923 K, the core outlet temperature of the coolant can be raised to >773 K, so that the practical thermal efficiency of the power plant can be obtained.

These results indicate that the integrity of the metallic fuel pin can be assured up to sufficiently high burnup, and that the design limit for the potential liquefaction does not deteriorate the attractiveness of the metallic fuel stated in Chapter 1. Therefore, it can be concluded that the metallic fast reactor fuel is applicable to commercial use.

In the future, if the applicability of the metallic fuel is confirmed by irradiation tests under commercial fast reactor conditions, this attractive metallic fuel can be selected as a reference fuel for the fast reactor. The technical and economic breakthroughs brought about by the metallic fuel will accelerate realization of the commercial fast reactor and its fuel cycle, which will consequently enhance the national energy security.



**Acknowledgments**

I would like to thank Mr. T. Yokoo of the Central Research Institute of Electric Power Industry (CRIEPI) for his useful comments on development, validation and application of ALFUS. Furthermore, he made a great contribution to preparation for a series of the ex-reactor experiments. I also wish to acknowledge the contributions to the modeling efforts made by Mr. M. Kinoshita of CRIEPI, Mr. M. Ishida of Hitachi Engineering Co., Ltd., Dr. T. Kobayashi, Mr. Y. Tsuboi and Dr. Y. Iwano of Toshiba Corporation, Mr. K. Ito and Mr. Y. Saito of Nuclear Development Corporation., Dr. T. Ogawa of Japan Atomic Energy Research Institute, and Mr. H. Saito of the CRC Research Institute. The technical support to the ex-reactor experiments provided by Dr. M. Kurata and Mr. K. Nakamura of CRIEPI and Dr. M.A. Mignanelli, Mr. J.J.W. Green and Dr. I.A. Vatter of the AEA Technology plc. is greatly appreciated. I would like to thank Prof. A. Serizawa, Prof. K. Higashi, Prof. M. Koiwa, and Dr. I. Takagi of Kyoto University for their suggestions to improve this thesis.

I want to thank my wife, Yuko, and my daughter, Yuri, for their mental support to me.